ABSTRACT

COLMER, WILLIAM DONALD LOUIS. Development of Vessel Lower Head Heat Transfer Analysis Capability for Evaluation of In-Vessel Retention Thermal Margin. (Under the direction of Dr. Nam Dinh).

In-vessel Retention (IVR) is a leading strategy for severe accident management (SAM) strategy in several advanced Light Water Reactor (LWR) designs. IVR strategy relies on maintaining coolability of molten corium and debris in a reactor pressure vessel lower head by external reactor vessel cooling (ERVC) by ensuring the thermal margin to critical heat flux (CHF) on the exterior. In this strategy, the integrity of the lower head is preserved and the molten corium material will remain contained in the pressure vessel, arresting accident progression and mitigating consequences. Multiple studies have investigated boiling heat transfer on the vessel lower head exterior surface, the composition of corium layers inside the vessel, as well as the heat transfer driven by decay heating that occurs within.

The goal for this work is to develop an analytical capability to characterize heat transfer in the lower head of the corium pool layers, the vessel structure, and the heat removal on the vessel exterior. Previous work includes the FIBS model from UCSB, followed by the VESPA revision model from INEEL and ERI IVRAM model. In this study, a lumped parameter approach is employed for heat transfer in a two-layer configuration, while the vessel lower head wall.is treated with angular segmentation to reflect large angular dependency of corium pool's downward heat flux. This model enables thermal loading analysis in different vessel lower head geometries and input conditions, offers a vast improvement of computational time over high-resolution methods, and determines the thermal margin to vessel failure in a given scenario. The IVRAM calculations performed by Esmaili et al. are used for benchmarking the code developed in this work.

The developed approach remains similar to these previous endeavors but improves upon them by offering insight into reactors such as the AP1000 but also lower power SMR designs with ellipsoidal lower heads. Information regarding thermal margin and resistance to vessel failure for these SMR reactors help inform the safety design under development. Additionally, the development of a quasi-transient model allows for progressive calculations which track system vulnerabilities by encompassing time dependent decay heating with scenarios for molten corium mass addition to the lower head system. This capability,

combined with the computational efficiency of the model, makes it suitable for tracking the lower head integrity under a wide range of possible accident progressions.

Development of Vessel Lower Head Heat Transfer Analysis Capability for Evaluation of In-Vessel Retention Thermal Margin

by
William Donald Louis Colmer

A thesis submitted to the Graduate Faculty of
North Carolina State University
in partial fulfillment of the
requirements for the degree of
Master of Science

Nuclear Engineering

Raleigh, North Carolina
2015

APPROVED BY:

_____	_____
Nam Dinh, Ph.D. Committee Chair	Joseph M. Doster, Ph.D.
_____	_____
Igor A. Bolotnov, Ph.D.	Tiegang Fang, Ph.D.

DEDICATION

To Mom, to Dad, and to Pop-Pop, the first in our family to believe in nuclear energy

BIOGRAPHY

The author graduated from Vanderbilt University in Nashville, Tennessee, with a Bachelor of Engineering degree in Mechanical Engineering in 2011. During his undergraduate career he pursued concentrations in the fields of mathematics, economics, and material science in addition to his engineering curriculum. In the spring of 2011, he led a team of engineers from Vanderbilt who traveled to the Ulpan Valley near Cobán, Guatemala, to install a power generation capability, developed at the university, for the local population. In 2011 he was awarded with a departmental fellowship from the Nuclear Engineering department at North Carolina State University as a first-year graduate student. When Dr. Nam Dinh joined the faculty in January of 2013, the author began his work in severe accident and reactor safety research as his first student in North Carolina. In his free time the author enjoys playing bridge and manages the local Raleigh Bridge Club.

ACKNOWLEDGMENTS

I would like to first thank Dr. Nam Dinh for his constant guidance and support throughout our time working together. I have nothing but the deepest gratitude for your time and effort throughout the many ups and downs of this process. I would also like to thank my committee of Dr. Mike Doster, Dr. Igor Bolotnov, and Dr. Tiegang Fang for their contributions in reviewing my work as well as two additional faculty members, Dr. John Mattingly and Dr. Steve Shannon for their advice and support throughout my graduate career. Additionally, I would like to thank the Babcock & Wilcox Company for their support and resources concerning the SMR applications of this project as well as the representatives from B&W and the Westinghouse Company who supplied aid, feedback, or additional resources used in this report.

From the beginning of time my family has supported me and I would be hard-pressed to find myself where I am without them. Thank you to Mom, Dad, Sara, Clint, and all of the cats (Brady!) for your love and support. Happy 6-month birthday Nephew Luke! Perhaps one day he'll be an engineer like his uncle and grandfather. Finally, I would like to thank all of the fantastic friends I have made here in North Carolina who have truly made living here memorable and the thought of leaving unbearable: Alex, Casey, Dave, Jack, Jenn <(" }, Katie, Kyle, and Tim, to name a few. Thank you again, to you and to everyone, for enabling me to not only live here and obtain a degree, but to have the time of my life doing it.

TABLE OF CONTENTS

LIST OF TABLES

LIST OF FIGURES

LIST OF NOMENCLATURE

AP1000 – Westinghouse AP1000® Two-Loop, Generation III+ PWR (3415 MWt)

AP600 – Westinghouse AP600® Two-Loop, Generation III PWR (1940 MWt)

ATWS – Anticipated Transient without Scram

BWR – Boiling Water Reactor

CDF – Core Damage Frequency

CFP – Containment Failure Probability

CHF – Critical Heat Flux

DCD – Design Control Document

DNB – Departure from Nucleate Boiling

ERVC – External Reactor Vessel Cooling

FCI – Fuel-Coolant Interaction

HPME – High Pressure Melt Ejection

HRA – Human Reliability Analysis

IV(M)R – In-Vessel (Melt) Retention

LERF – Large Early Release Frequency

LOCA – Loss of Coolant Accident

LRF – Large Release Frequency

MCCI – Molten Corium-Concrete Interaction

PRA – Probabilistic Risk Assessment

PWR – Pressurized Water Reactor

R(P)V – Reactor (Pressure) Vessel

RCS – Reactor Coolant System

SAM – Severe Accident Management

SAMG – Severe Accident Management Guidelines

SMR – Small Modular Reactor

1 INTRODUCTION

1.1 Background on SAM and IVR

Following the nuclear accident at Fukushima Daiichi in March of 2011, the nuclear safety community has bolstered research into severe accident management and passive safety systems. This response is similar to how research into design basis accident response increased following the WASH-1400 report of 1975 and the Three Mile Island accident of 1979. The increased effort is necessary not only for preventing mistakes and oversights of the past but for determining the unrealized threats and providing a prevention strategy incorporating natural processes, risk assessment, and minimal human operator intervention. This work aims to support a small portion of that goal by characterizing a key physic during severe accident scenarios, heat transfer of molten core materials, and utilizing the results to inform the in-vessel retention severe accident management strategy.

Severe accident management strategies are often concerned with the protection of the integrity of the three basic barriers between radioactive core fission products and the general environment: the fuel rod cladding enclosures, the reactor pressure vessel, and finally the reactor containment structure. A SAM strategy changes priorities as these barriers fail in order to terminate the accident progression as soon as possible. The ultimate goal is to prevent a “large early release” of radioactive fission products into the environment where large refers to an amount which may inflict a threshold level of casualties while early refers to a time scale that restricts or prevents evacuation or other emergency preparation efforts. Before a discussion of the varied strategies to achieve this goal, we must define a basic accident progression.

During an accident scenario excessive heat buildup, generally caused from a loss of local cooling, may cause core materials to exceed cladding melting temperatures. In order to prevent the failure of this first barrier, methods such as coolant injection into the pressure vessel may be utilized.

This stage, seen in Figure 1-1, continues until the accident progression is terminated by ensuring long-term core cooling or the accident continues upon depletion of all injected coolant. At this point, the cladding is compromised and the core begins to melt down. Following the failure of one or more cladding structures, the molten core materials

(corium) may continue to break down other internal structures leading to an accumulation of corium in the lower head of the RPV.

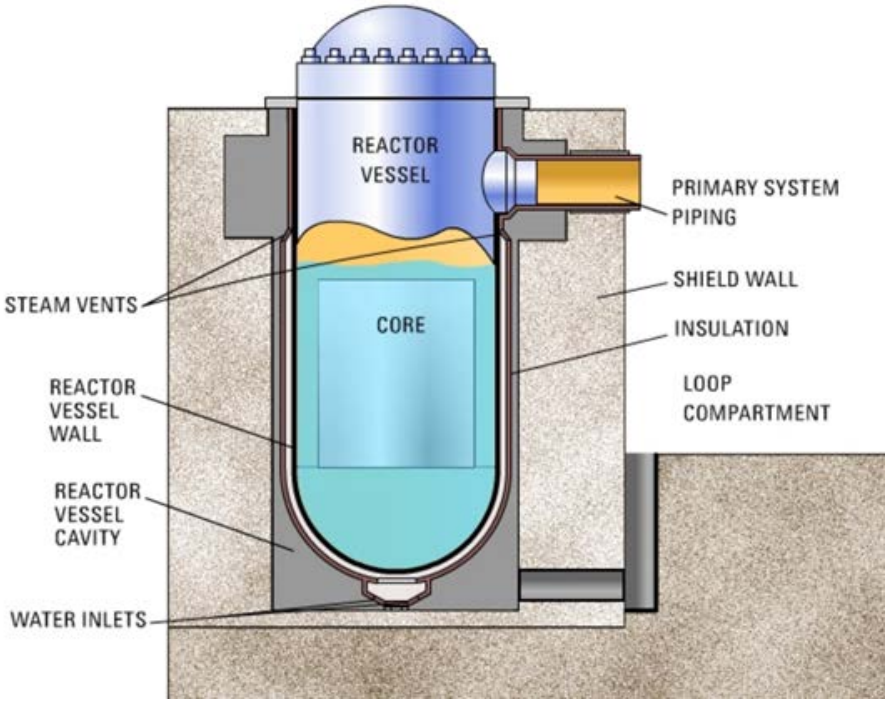

Figure 1-1: AP1000 during core-coolant injection accident phase

Following core breakdown, exposed fuel materials can react with coolant inside the pressure vessel in what is known as molten fuel-coolant interaction (MFCI). This process can generate excess heat which can further endanger the vessel structure. Inside the vessel, the molten corium collects and stratifies into distinct material layers. The main two layers to consider are the heavier ceramic and oxide materials and the lighter metallic materials from internal structures and other sources. The sole heat source in this example may be assumed as the volumetric heat generation in the oxide layer, and to a lesser extent the metallic layer, due to residual decay heat of the UO_2 and subsequent fission products. This generated heat imposes a heat flux on the vessel exterior where convective cooling determines the surface temperature.

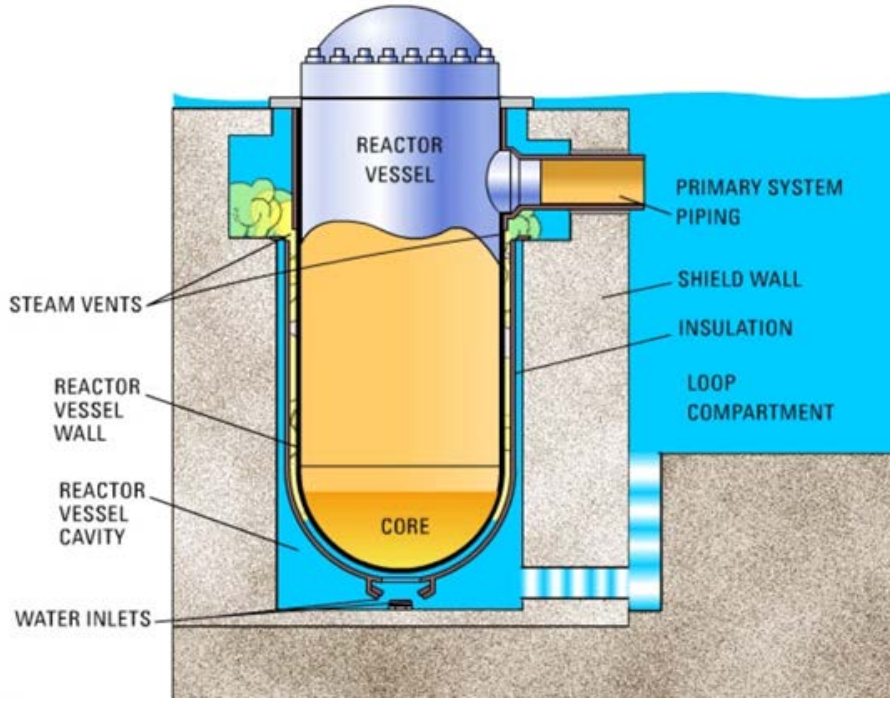

Figure 1-2: AP1000 following core breakdown and containment cavity flooding

At this stage, shown in Figure 1-2, successful cooling of the exterior leading to the termination of accident progression while containing all such molten corium materials within the reactor vessel is the criteria for the SAM strategy known as in-vessel melt retention. If, however, the corium remains inadequately cooled, the RPV integrity may be compromised, causing a deposit of core materials on the concrete containment basemat, the final defense between the hazardous fission products and the general environment. As IVR has failed, the next goal would be the successful cooling of the materials before the containment barrier fails, known as ex-vessel melt retention. The focus of this document, however, is IVR and its success or failure in various accident scenarios.

NB: Figure 1-1 and Figure 1-2 are frames from an animation from the Westinghouse Electric Company (LLC), used with permission from Mr. Jim Scobel, showing severe accident progression and mitigation methods used in the AP1000 plant.

1.2 IVR Metrics: Critical Heat Flux & Thermal Margin

In 1979, the Three Mile Island (TMI-2) accident showcased the possibility of partial or full core relocation during a loss of cooling scenario. Fortunately, only the first barrier was compromised in that accident and the progression was terminated with all materials still contained in the pressure vessel. Since the incident, however, IVR has become a key focus area for severe accident research as part of a total defense in depth strategy for facing emergency situations.

In order to adequately cool the core materials in the lower head, the containment structure must be flooded up to and exceeding the level of corium within the vessel. Once the containment and RPV have been depressurized, natural circulation provides the convective cooling on the vessel exterior. At this point, the key physic in determining IVR success is the generated heat flux compared to the heat removal rate of the bulk fluid. In order to maintain nucleate boiling on the surface of the vessel, the heat flux value must remain below that of the *critical heat flux* (CHF). At this point, the system would undergo a boiling crisis, where vapor bubbles no longer detach from the vessel surface. These bubbles, rather, accumulate into large bubble masses or entire vapor films which effectively insulate the vessel surface from the moving fluid coolant layer. Due to the inferior heat removal caused by the presence of the vapor layer, the surface temperature will rapidly rise. Once temperatures reach the melting point of the vessel, the RPV will fail locally, causing an egression of the melt and ending the IVR process. Therefore, accurate predictions of both CHF and vessel heat flux values are necessary for determining the *thermal margin* or the disparity between the two values. This thermal margin will serve as the figure of merit for this project.

1.3 Melt Pool Formation and Heat Transfer Overview

As previously mentioned, as the melt pool relocates and continues to grow, it will stratify into different material layers as shown in Figure 2-1. There are important phenomena which occur at the onset of the pool formation such as the possibility of either a melt jet or interior steam explosion caused by the interaction of molten core materials with coolant previously injected into the pressure vessel. These are complex phenomena,

however, and for the purposes of this document we shall continue to the case where the corium has begun to settle in the base of the vessel [1].

The heat in an IVR scenario may be assumed as purely decay heating of fission products contained in one or both of the stratified corium layers. Immediately following a reactor trip and control rod insertion, total decay heating drops to around 7% of previous operating levels. As is shown in Figure 1-3, heat generation drops logarithmically over time with typical accident scenarios occurring at around 0.5-1.5% of a plant's thermal power rating. In the case of the AP1000 this accounts to approximately 15-50 MWt generated in the corium layers.

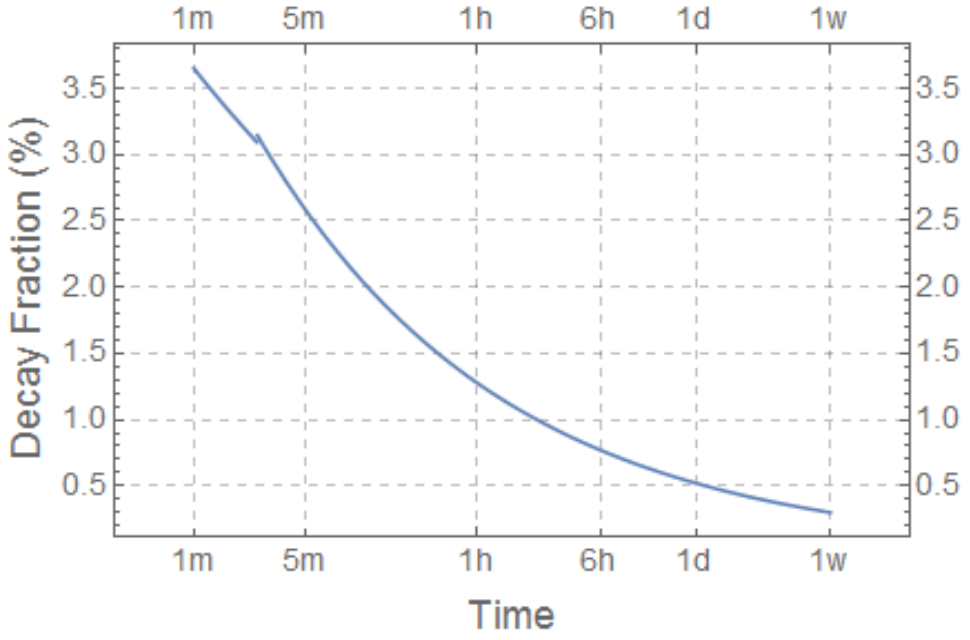

Figure 1-3: Decay heating curve following reactor trip

In the bulk of the oxide layer and in the entirety of the molten light metal layer, the primary heat transfer mechanism is natural convection driven by the internal heat generation. Since the oxide layer forms a crust at its boundaries, the heat is then conducted through the crust into either the vessel wall or the above light metal layer. In the light metal layer, the heat is either conducted through the vessel wall or radiated to the internal

structures of the pressure vessel. The convection in both the oxide and metallic layers may be correlated based on the internal Rayleigh numbers and, occasionally, factor in the fluid Prandtl number when calculating the Nusselt number for the layer. Generally the heat transfer in these layers is divided into upward and downward (or sideways) facing heat fluxes. It has been shown that the sideways facing heat flux has an angular distribution, increasing as the angle from the bottom center of the vessel increases. Figure 1-4 shows a typical stratified melt pool and the associated heat transfer phenomena for the separate materials and locations. *Graphic used with permission from Dr. R.R. Nourgaliev* [2].

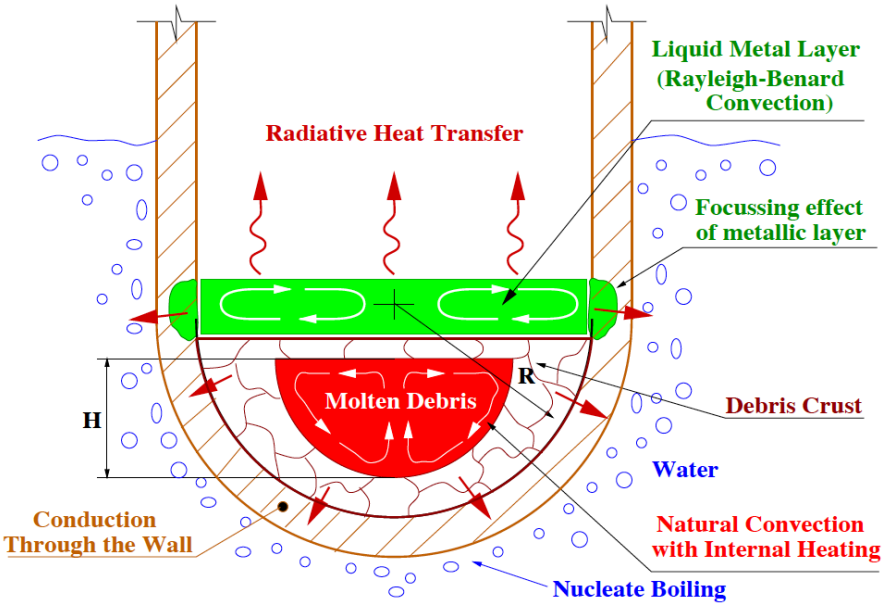

Figure 1-4: Typical heat transfer scheme of stratified corium pool during ERVC

Thus, the highest heat fluxes in the oxide pool occur at the peak of the pool bordering the metallic layer. Fortunately, correlations for the critical heat flux also demonstrate an increasing behavior with the positional angle, allowing for the maximum thermal margin between the two values. In the metallic layer, a similar trend can be shown with heat fluxes increasing up the vertical height of the layer. Thus, in both layers the peak

fluxes may be observed at the corners of the layers. This trend is useful in predicting failure locations as well as qualitatively judging modeling results.

There are multiple uncertainties involved in the determination of the melt pool convection. The degree of stratification in the lower section of the pool determines the conduction dominant effects observed in the area. Meanwhile, the fluid properties drive the formulation of the internal Rayleigh number, which is indicative to the degree of turbulence observed in the convective bulk of the pool. Therefore, the composition of the pool and the formation process become key physics in determining the convective flow in the layer. Uncertainties related to these physics are numerous and include the timing of the accident, the amount of coolant in the pressure vessel at the time of the first core relocation, and the method of relocation including possible jet diameter.

A separate phenomenon which occurs in the heat transfer model is that of the metallic layer focusing effect. A gross majority of the heat in the metallic layer has been received from the oxide pool as only a fraction of the corium decay heat is generated in the top layer. Since the lower thermal boundary of the metallic layer is entirely incoming heat, the transfer must occur either out of the top of the pool via radiation or through the vessel wall via conduction at the sides of the layer. When the metallic layer is fairly thin, however, the low surface area on the sides of the pool create demonstrably higher heat fluxes than are generally seen elsewhere in the scenario. These adversely high heat fluxes can easily surpass CHF values and cut through the vessel wall if not accounted for properly.

1.4 Example Safety Case & Role of IVR in SAM: Westinghouse AP1000® [3] [4]

The Westinghouse AP1000 is a base case example of a reactor design using similar ERVC procedures as part of its SAMG. Following is a summary of the probabilistic risk assessment (PRA) submitted by Westinghouse as part of the AP1000 DCD [5]. Also contained is an overview of the role of IVR in this safety case.

The PRA for the AP1000 is a three tier framework containing information about all stages of accident progression from initiating events to CDF, CFP, and LERF values. In the first level of the PRA, the report covers initiating events and the progression of design basis accidents before the advent of core damage. Once a list of initiating events has been

compiled, it is categorized based on various factors such as plant response or possible accident outcome. These initiating events then provide a basis for event trees documenting the possible accident progression. For the AP1000, 26 initiating events were categorized into three primary sections: LOCA-type events, transients, and ATWS events. Throughout the event tree process, probabilistic distributions provide likelihoods for multiple progression factors ultimately resulting in effective expected values for each end-state in the PRA 1 process. These end-state probabilities are also subject to HRA tests in order to determine the effect of operators on stages of progression.

Once the end states have been determined through the PRA 1, the PRA 2 process takes over to determine the LRF of each PRA 1 end-state. Much like in PRA 1, the end results of PRA 2 can be classified into six main categories corresponding to the magnitude and type of release expected in each case. Not included in the LRF are scenarios resulting in a non-failed/non-bypassed containment; these cases are referred to as "no emergency action" cases. Throughout the PRA 2 process, additional probabilistic distributions and HRA tests are utilized in order to analyze pertinent severe accident phenomena. For the AP1000, the phenomena considered were: FCI/steam explosion, HPME, MCCI, and hydrogen combustion/detonation. Following the end results of PRA 2, the effects on environment, population, logistics for cleanup/evacuation, and long term effects are included in PRA level 3. In conclusion, the AP1000 PRA reported a total core damage frequency (CDF) value of 5.09x10-7/year and a total large early release frequency (LERF) of 5.94x10-8/year. Both of these values are between two to three orders of magnitude smaller than the safety goals presented by the NRC at the time of submission.

The role of IVR in the above safety case involves the mitigation of the accident progression during the PRA 2 phase. During this phase, core damage has been determined and certain event tree items such as successful depressurization of the vessel and flooding of the containment cavity signal the beginning of IVR methods. It is at that point where predictive modeling capability for key physics such as thermal margin, heat flux distribution, critical heat flux ranges, and corium pool formation and distribution inform the PRA approach. By identifying appropriate methods to quantify these key physics in addition to the quantification of the related uncertainties to the process, the overall risk to

the vessel during the IVR phase may be determined within a certain confidence. Therefore, the advancement of these methods and the improvement of the analytic capabilities for not only the single key physics but also the integrated effect allows higher confidence risk assessments and better understanding for the overall LERF.

1.5 SMR Design, Safety, and Coolability

Small modular reactor (SMR) designs focus on smaller form-factor, lower power reactor designs, typically designed with a fully passive safety system. These reactors are attractive to population areas where factors such as energy consumption, access to sufficient fresh water, or capital cost render larger plants such as the AP1000 infeasible. SMRs have also been offered as a means to retrofit coal power facilities and slowly reduce the dependence on coal in the power grid. The SMR to be examined in the project is the Babcock and Wilcox mPower design, currently in the design certification process with the USNRC. Data and information comes from publicly published sources such as Halfinger [6].

Numerous design features in the mPower reactor naturally prevent or greatly reduce key design basis accident scenarios. Reproduced in Figure 1-5, the mPower features a fully integral design where the core, once-through steam generator, control rod structure, and coolant pumps all reside within the pressure vessel housing. This structure has no penetrations in the lower head, preventing failure modes associated with such penetrations such as instrumentation and guide tube failure (IGTF). There are also no steam or coolant lines below the level of the core, effectively preventing LOCA-type accidents. Additionally, the control rod structures are located within the pressure vessel which prevents the pressure differential required for a rod ejection event. The plant uses standard fuel enrichment of <5% U_{235} and operates on a 4-year refueling cycle at which point all core materials are fully exchanged. The core balance for such a fuelling pattern produces lower average linear power densities than in conventional reactors, which improves thermal margins to CHF.

A key design feature in the mPower and other SMR designs is the fully passive safety system for use in severe accident management. Following a reactor trip in an accident scenario, the mPower reactor has been designed such that the containment

structure is flooded and the reactor is cooled via natural circulation for up to three days. Following a slow depressurization of the vessel, the core remains externally covered with coolant and, if the core begins to break down, the system follows an IVR strategy. Differences in the reactor design that impact heat transfer characterization in the lower head during IVR include a lower thermal power rating of 530 MWt, lower total core and structure loading for melt pool formation, and an elliptical lower head geometry which creates a flatter and more evenly distributed platform for the corium pool.

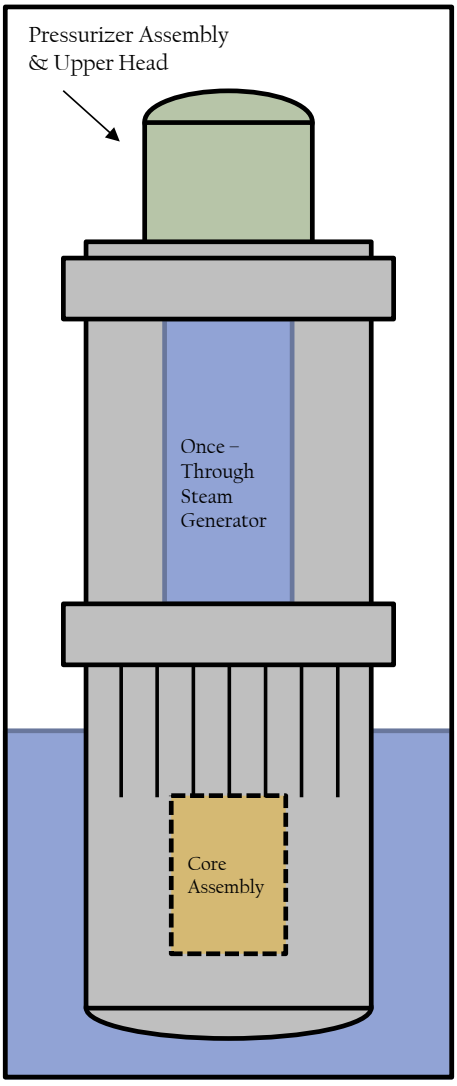

Figure 1-5: Integral SMR pressure vessel layout

1.6 Motivations and Project Goals

Previous sections discussed the necessity for accurately predicting the thermal margin to critical heat flux for the determination of IVR success. In order to obtain the most detailed and accurate view of the heat transfer scenario, high resolution methods may be used to model the lower head system. These methods are extremely computationally expensive, however, and, as a result, have exceedingly long runtimes to produce a solution for a single scenario. When considering the highly dynamic environment of a severe accident as well as the multitude of influencing factors for the heat transfer profile of the vessel, it is vital to have an accurate yet reconfigurable tool to perform multiple calculations and simulations in a given time period. Therefore, the aim of this project is to develop a new analytic model to characterize the heat transfer in the lower head of a reactor vessel during IVR scenarios. The framework for the model is based on work performed by Esmaili et al. (IVRAM) [7] as well as previous work done by Theofanous et al. (FIBS) [8] at UCSB and Rempe et al. (VESPA) [9] at INEEL. Specifically, the model characterizes the heat transfer in a Westinghouse AP-1000 reactor undergoing natural circulation following a reactor cavity flood.

In order to provide new and useful additions to IVR analysis, there are certain characteristics desired of the final design. The goals of the model are:

1. Show a developed analytic capability for characterization of heat transfer throughout a developed corium pool and determination of the thermal margin to critical heat flux on the vessel exterior
2. Provide the above analysis for different plant properties and vessel geometries, ultimately correlating to conventional and SMR reactor designs
3. Showcase alternative applications including quasi-transient behavior and development of real-world tools and aids to SAMG research
4. Perform sensitivity analysis for example parameters or correlations to inform uncertainty and contribute to overall model uncertainty quantification

Part of the novelty in this model's approach concerns the geometric capabilities of the program. By switching readily between hemispherical and elliptical situations, including applying the appropriate correlations, immediate comparisons are able to be shown for thermal margin for both geometries. In addition, with flexibility for reactor parameters such as thermal power and core loading, the model is able to function not only for conventional, high power reactors such as the AP1000 but may also be used for exploring thermal margins in SMR types. Finally, with quasi-transient and fast running calculations, dimensionless number correlations may be compared for sensitivity analysis and uncertainty quantification. This method can be expanded for different distributed parameters to ultimately contribute to the overall uncertainty quantification of the model. Additionally, certain applications such as coolability maps or accident timing analyses may be performed or created for various reactors and conditions.

2 MODEL DEVELOPMENT

2.1 Literature Review

2.1.1 DOE Research, FIBS Model (Theofanous et al., 1996) [8]

Original research for in-vessel retention methods for the AP600 began in 1996 with work by Dr. Theofanous and his group at UCSB. The approach to the work was to develop a risk oriented model for failure modes involved in the IVR strategy. The quantification for said risk was derived from a combination of data sources including energy flow calculations within the structure and molten corium pool, predictions of thermal loading, computer modeling to produce angular positional-based results, and structural work to validate the consideration of DNB as the figure of merit for failure. Certain assumptions for the state of the vessel and pool were made upfront to dictate future work. These assumptions included a pre-conditioning of the lower head to a depressurized saturation situation, a consideration of thermal and creep stresses as the only pertinent failure mechanisms, and a constant nucleate boiling regime on the exterior of the vessel (until conditions dictate a departure scenario). An extension of the third assumption would be that the flow of liquid and vapor remains unobstructed during the analysis.

The presented geometry for the foundation of the research included a hemispherical lower head as was to be expected on the AP600. Inside the vessel, the natural convection research was based on a two-layer molten corium pool: a bottom oxide pool with a surrounding crust and a light metal layer resting on top. Certain assumptions had to be made regarding these layers and the heat transfer mechanisms therein. First, for the pool to be considered as in its most limiting case, the material must be assumed fully melted in order to lose no energy from state conversion. Second, the pool must be considered at its maximum temperature and, thus, at a thermal steady state. Finally, in order to maximize the outlet of heat to the vessel walls, the thermal resistance to the metal layer must be maximized. These assumptions carry over into present analysis using the developed model.

In the study, Theofanous was able to develop a failure criteria curve versus the angular position on the lower head. This CHF correlation for the AP600 was derived from experimental data drawn from the ULPU experiments at UC Santa Barbara. The boiling crisis curve showed that DNB was a viable failure option. In fact, compared to other possible failure criteria examined, the Theofanous group determined that DNB was the only viable failure mode to examine, that failure could in fact not occur without a boiling crisis event. The correlations used in the study ranged from previously established correlations such as the Kulacki & Emara and the Mayinger correlation to newer data at the time from the Mini-ACOPO studies on the AP600.

A major conclusion of the work performed at UCSB was that a thermal failure of the vessel was physically unreasonable, i.e., external heat flux values would always remain below the CHF limit. While the study did observe that the thermal margin to CHF decreased with increasing angular position from the vessel center, the levels were all deemed comfortable so long as the reactor depressurized and had adequate access to cooling. This conclusion was later challenged and rejected by the INEEL review performed by Rempe et al.

2.1.2 INEEL Revision, VESPA Model (Rempe et al., 1997) [9]

Following the DOE funded work at UCSB by Theofanous et al, a revision project was run through INEEL by Rempe et al. The goal of the INEEL revision was to assess uncertainties not considered in the original work and to reconsider certain assumptions (or

assertions) made by the Theofanous group. The work at UCSB centered around two main assertions. First, the reactor vessel would not fail in the prescribed depressurized, saturation environment if the external heat fluxes remained below the CHF limit. Second, their findings showed that the heat flux values never exceeded CHF values and, thus, the vessel had no threat of thermal-induced failure. The Rempe group at INEEL challenged the second assertion on the basis of a variety of factors. First, the UCSB group did not examine a sufficient set of geometric configurations for the molten corium layers. Second, the assumptions and input configurations and correlations used in the analyzed geometry were inaccurate or incomplete. Finally, the sensitivity studies presented by the UCSB group in an effort to address reviewer comments failed to incorporate the integral effects of multiple such factors simultaneously. Overall, the findings of the INEEL review were that the final conclusion that thermal-induced failure due to CHF was unlikely remained valid but the margin presented by the work at UCSB was overstated. While the impact of the findings were not quantified in the INEEL review, a bounding condition showed the long term risk to the reactor design still remained below design goals.

In order to test some of the issues the INEEL review considered, the panel performed calculations using established models such as SCDAP/RELAP and MELCOR. In addition, a new model named VESTA was created. The VESTA model contained many similarities to the UCSB model when it came to heat transfer mechanisms in the layers (i.e. natural convection in the oxide pool, conduction through the ceramic crust etc.). The model differed, however, in its ability to quantify uncertainties using Bayesian and Monte Carlo methods. In addition, the VESTA platform could also account for heat generation in the metallic layer as well as multiple unconsidered uncertainties from sources such as heat transfer correlations, input parameters, emissivity and decay heat load. The VESTA results validated many of the calculations performed at UCSB. The main difference was the calculation of the heat flux at the higher angles form the vessel center. The VESTA platform predicted higher values of the heat flux experienced in those regions. While not high enough to surpass CHF, the VESTA results did indicate that the thermal margin to failure should be smaller than previously expected. The INEEL group did, however,

corroborate the overall finding of UCSB that failure due to insufficient cooling in the prescribed environment is a low probability event.

2.1.3 ERI Study, IVRAM Model (Esmaili et al., 2005) [7]

In 2005, H. Esmaili and his group were tasked by the US NRC through Energy Research Inc. (ERI) to develop a model (IVRAM) based on Westinghouse AP600 data and correlations which could predict failure likelihood in the AP1000 reactor. The developed model used previous one and two-dimensional heat transfer mathematical models as well as previously established correlations and relations. The IVRAM model represents a set of 29 equations which serve to define two different melt pool configurations as postulated in severe accident scenarios. The two melt configurations outlined in the report are a two-layer stratified model (Configuration I) and a three-layer model including a bottom heavy metal layer (Configuration II).

For the basis of the mathematical model presented in the IVRAM paper, three main assumptions were identified. First, there was assumed to be no heat generation in the vessel wall. Second, there is no crust formed on top of the light metal layer as the radiative heat flux from the surface was not viewed as great enough to do so. Lastly, no material interaction was considered. In addition to these main, listed assumptions, additional points can be made regarding the presented model. First, the bottom heavy metal layer has been assumed to only direct heat downwards towards the vessel wall. The interface between the oxide pool and the heavy metal layer is seen as fully reflective. Next, there is no transfer of material between any such layers and, as such, this is a purely static, snapshot model. Finally, the model is limited to the hemispherical geometry of the AP600/1000 designs and develops no correlations for heat transfer.

Similar to the UCSB FIBS [8] and the INEEL VESTA [9] models, the IVRAM model is a lumped parameter approach utilizing an angular distribution on the oxide pool surface in contact with the vessel wall. In order to adapt to the AP1000 scenario, the CHF correlation developed by Park and Dhir [10] for the AP600 was updated to match ULPU configuration IV and V data [11]. The ULPU facility, located at UCSB, originally produced the data for the AP600 correlation. These later configurations of the facility,

however, provided the basis for a multiplication of the original AP600 values to account for the increased thermal power rating.

The results of the IVRAM analysis supported the findings of the FIBS and VESTA models. Overall IVRAM recognized the threat of the metallic layer focusing effect as a primary cause for vessel failure. In addition, the IVRAM results supported the relative probabilities of vessel failure based on melt configuration and corroborated the unlikelihood of vessel failure in the ceramic pool region. In addition, the IVRAM model showed that the addition of a heavy metallic layer (configuration II) did not adversely impact failure probabilities and exhibited the same improbable failure chance below the metallic layer.

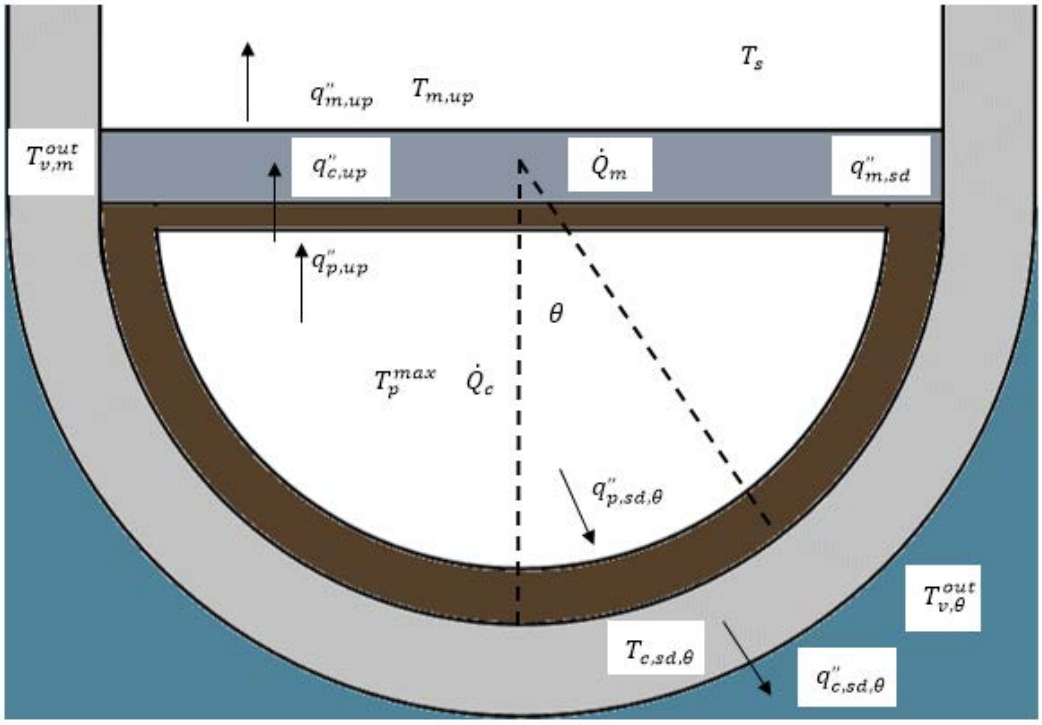

Figure 2-1: Hemispherical lower head showing heat-flux and temperature profile

2.2 Equation Derivation

The goal for this model is to use a simple equation set to characterize the heat transfer in the lower head during IVR scenarios. For analysis a conventional two-layer model of the lower head is considered where the molten corium has separated into an

oxide/ceramic layer surrounded by an oxide crust with a lighter, metallic layer resting on top. The equation set encompasses the heat generated by the layers, convective transfer through the oxide and metallic layers, as well as conductive transfer through the crust and through the vessel. Finally, the boundaries are governed by a radiative condition above the metallic layer and a convective condition on the vessel exterior. The initial values and material properties were provided by the ERI input data used by Esmaili et al [7] in their *IVRAM* study performed for the AP600 and AP1000 in 2005. The platform used to implement our model was the Mathematica Computational Package (v9/v10), developed by Wolfram Research [12]. Table 2-1 outlines the general parameters found in the model.

2.2.1 General Equation Derivation

The equations solved in this model for the most part include derived equations for conductive heat transfer and general equations for convective heat transfer and total energy conservation. Figure 2-2 shows a generic conduction example with internal heat generation as seen in the heat transfer model.

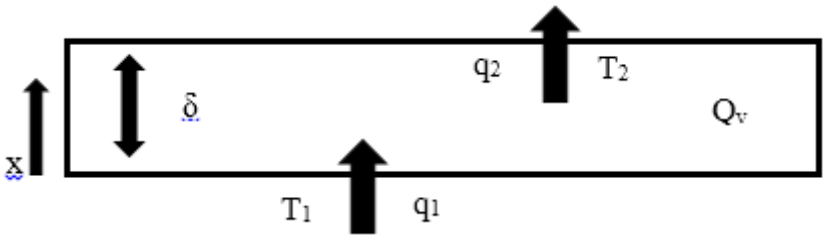

Figure 2-2: Generic conduction scenario

In this example, the general heat balance equation is:

$$k\frac{dT^2}{dx^2} + Q_v = 0$$

Heat flux equations at the boundaries (x = 0 and x = δ) give the following conditions:

$$x = 0 \qquad q_1 = -k\frac{dT}{dx} \qquad T = T_1$$
$$x = \delta \quad q_2 = q_1 + Q_v * \delta \quad T = T_2$$

Integrating the balance equation once and twice yields the following solutions:

1) $$\frac{dT}{dx} = -\frac{Q_v}{k}x + C_1 \Longrightarrow \left.\frac{dT}{dx}\right|_{x=0} = C_1 \Longrightarrow C_1 = -\frac{q_1}{k}$$

2) $$T_x = -\frac{Q_v}{k}\frac{x^2}{2} + C_1 x + C_2 = -\frac{Q_v}{k}\frac{x^2}{2} - \frac{q_1}{k}x + C_2 \Longrightarrow T|_{x=0} = C_2 \Longrightarrow C_2 = T_1$$

The relationship for temperature solved at the far boundary yields:

$$T_x = T_1 - \frac{x}{k}\left(\frac{Q_v x}{2} + q_1\right) \Longrightarrow T|_{x=\delta} \Longrightarrow -k\frac{(T_2 - T_1)}{\delta} = q_1 + \frac{Q_v \delta}{2}$$

Using the final boundary condition the final result for heat flux yields:

$$q_2 = q_1 + Q_v * \delta \Longrightarrow q_2 = -k\frac{(T_2 - T_1)}{\delta} + \frac{Q_v \delta}{2}$$

2.2.2 Oxide Pool

The first constructed mathematical model was a one-layer molten corium pool thermal loading simulator. The design was initially based off of similar models for two and three-layer configurations presented by Esmaili et al (IVRAM) [7]. After difficulty pertaining to adapting the framework of the referenced models, a new set of equations was derived for the one-layer case in order to provide the base of the current iteration of the model. The set of equations used for the one pool model has been presented below. Data concerning corium properties came from the ERI trials outlined in the IVRAM paper by Esmaili et al.

The code uses energy balance as well as basic convective and conductive heat transfer equations (and one radiation heat transfer) in order to characterize the thermal loading of the corium pool. The pool has been split into upward facing heat flux and temperatures and "side" or downward facing values. In future models where a heavy metal layer exists beneath the oxide pool, the current notation of "side" will make more sense given the "downward" moniker will apply to those regions below said heavy metal layer. At first glance this set of equations has 12 unknowns (4 heat flux values, 4 temperatures, 3 thicknesses, and one height). However, the inner vessel temperature and vessel thickness cannot be unknown values at the same time. Either the temperature is below the vessel melting temperature and, thus, the thickness will not change, or the wall temperature is constantly at the melting point and there is ablation of the vessel wall. Thus, for any given scenario the set of 11 equations contains 11 unknowns. Table 2-2 contains the calculated

parameters and Table 2-3 the equations developed for the oxide pool; a short description of the derivation process is included below.

Heat balance equation for oxide pool:

$$\dot{Q}_c * V_{cor} = q''_{c,up} * A_{c,up} + \sum_{\theta} q''_{c,sd,\theta} * A_{c,sd,\theta} \qquad \text{p10}$$

The total generated heat in the pool is the volumetric decay heat multiplied by the pool volume (eq. p10). Due to conservation laws, the total heat leaving the pool at its boundaries must equal this generated decay heat. The boundaries of the pool have been divided into the top facing and side/down facing portions of the ceramic crust which forms around the edge of the oxide pool. Thus, the product of heat flux in these regions by their respective surface areas yields the total heat transfer out from the vessel.

Total heat transfer through the top of the oxide pool:

$$q''_{p,up} = h_{p,up}\left(T_p^{max} - T_{cor}\right) \qquad \text{p1}$$

$$q''_{c,up} = \frac{k_c}{\delta_{c,up}}\left(T_{cor} - T_{c,up}\right) + \frac{1}{2}\dot{Q}_c * \delta_{c,up} \qquad \text{p2}$$

$$q''_{c,up} = q''_{p,up} + \dot{Q}_c * \delta_{c,up} \qquad \text{p3}$$

$$q''_{c,up} = \sigma\left({T_{c,up}}^4 - {T_s}^4\right) * \left(\frac{1}{\varepsilon_c} + \frac{1-\varepsilon_s}{\varepsilon_s} * \frac{A_{c,up}}{A_s}\right)^{-1} \qquad \text{p4}$$

The heat flux on the top pool surface, interfacing with the crust, is a convective transfer governed by the maximum temperature of the oxide pool. The interfacial temperature of the crust is assumed to be the melting temperature of the corium. Thus, this temperature difference drives the convective transfer inside the pool (p1). The transfer through the crust itself is conductive with additional heat generation. This crust heat generation is the same magnitude as the bulk of the oxide pool and the driving temperature difference is that of the corium melting point and the upward crust boundary temperature (p2). However, this is equivalent to saying the crust outward heat flux is the sum of the input flux and the heat generation multiplied by the thickness (p3). Finally, with no metallic layer considered, the top of the ceramic crust radiates heat to the interior structures of the reactor vessel where T_s is a constant for the reactor scenario (p4).

Total heat transfer through the side of the oxide pool:

$$q''_{p,sd,\theta} = h_{p,sd,\theta}\left(T_p^{max} - T_{cor}\right) \quad \text{p5}$$

$$q''_{c,sd,\theta} = \frac{k_c}{\delta_{c,sd,\theta}}\left(T_{cor} - T_{c,sd,\theta}\right) + \frac{1}{2}\dot{Q}_c * \delta_{c,sd,\theta} \quad \text{p6}$$

$$q''_{c,sd,\theta} = q''_{p,sd,\theta} + \dot{Q}_c * \delta_{c,sd,\theta} \quad \text{p7}$$

$$q''_{c,sd,\theta} = \frac{k_v}{\delta_{v,\theta}}\left(T_{c,sd,\theta} - T_{v,\theta}^{out}\right) \quad \text{p8}$$

$$q''_{c,sd,\theta} = C_{boil}\left(T_{v,\theta}^{out} - T_{sat}\right)^3 \quad \text{p9}$$

Similar to the top section of the crust, the side sections undergo convection driven by the bulk pool and conduction through the ceramic crust including additional heat generation (p5, p6, p7). Heat is then conducted through the vessel wall driven by the temperature difference of the crust boundary and the externally cooled vessel surface (p8). With no heat lost to phase changes or other sinks, the heat flux may also be defined as the convective transfer to the coolant bulk fluid, controlled by an empirical boiling constant [13] (p9). These equations are repeated for each of the angular segments created in the model. The convective heat transfer coefficient in (p5) is multiplied by an angular correlation (Park & Dhir) [10] in order to increase values, and thus heat transfer, with increasing angular position along the vessel.

2.2.3 Metallic Layer

The light metal layer which forms on top of the oxide pool is the second layer to be characterized by our model. Results from this layer may provide insight as to the likelihood of different failure modes as well as the position of maximum failure likelihood. Much of the speculation surrounding these phenomena stems from the proposed focusing effect resulting from a thin light metal layer amplifying heat flux values at the interface with the oxide pool and vessel wall.

In order to provide for maximum flexibility, the light metal layer was to be calculated as a separate entity. This allows the model to avoid unnecessary calculations if there is no light metal layer present once the one and two pool codes have been joined

together. The current 6 equations cover 8 variables. However, two of these variables are shared with the oxide pool and the height of the light metal layer should be deterministic for all cases. This leaves 5 variables for the 6 equations, but since the radiation heat transfer equation has been removed from the oxide pool solution and placed into this model, when combined the equation/unknown count will balance. When computing the light metal layer the radiative heat transfer equation is reassigned to describe the upper surface of the metal layer as opposed to the top crust of the oxide pool.

The model progression for the light metal layer included a separate model for simple, uniform heat loading on side walls (one node), spatial discretization of the side wall area with uniform heat flux (multi-node), and finally multi-node non-uniform heat flux distribution on side walls. These three iterations allow for a complete characterization of the layer and will then transition to a two-pool combined model. Table 2-4 contains the calculated parameters and Table 2-5 the equations developed for the metallic layer; a short description of the derivation process is included below.

Heat balance equation for metallic layer:

$$\dot{Q}_m * V_m + q''_{m,dn} * A_{m,dn} = q''_{m,up} * A_{m,up} + q''_{m,sd} * A_{m,sd} \qquad \text{m6}$$

The generated heat in the metallic layer is much smaller and is approximated as 10% of the volumetric heat generation of the oxide pool. The bulk of the input heat to the metallic layer comes from the below oxide pool. Similar to the oxide pool, this heat is released through the top and sides of the layer (m6). Note that when a metallic layer exists, the radiative equation from the oxide pool no longer applies and that heat flux parameter is instead re-equated to the “downward” heat flux of the metallic layer, creating the influx.

Total heat transfer through the top of the metallic layer:

$$q''_{m,up} = h_{m,up}\left(T_{m,dn} - T_{m,up}\right) \qquad \text{m4}$$

$$q''_{m,up} = \sigma\left({T_{m,up}}^4 - {T_s}^4\right) * \left(\frac{1}{\varepsilon_t} + \frac{1-\varepsilon_s}{\varepsilon_s} * \frac{A_{m,up}}{A_s}\right)^{-1} \qquad \text{m5}$$

Similar to the oxide pool, heat transfer in the metallic layer is a convective process driven by the temperature difference between the top and bottom of the layer (m4). At the top of the metallic layer, heat is radiated to the reactor interior structures (m5).
Total heat transfer through the sides of the metallic layer:

$$q''_{m,sd} = h_{m,sd}\left(T_{m,dn} - T_{ves}\right) \quad \text{m1}$$

$$q''_{m,sd} = \frac{k_v}{\delta_{v,m}}\left(T_{ves} - T_{v,m}^{out}\right) \quad \text{m2}$$

$$q''_{m,sd} = C_{boil}\left(T_{v,m}^{out} - T_{sat}\right)^3 \quad \text{m3}$$

Also similar to the oxide pool is the sideways heat transfer in the metallic layer. With no crust to pass through, the convection exists to the inner boundary of the vessel, where heat is conducted through the wall, and removed via convection by the bulk coolant. One assumption here is that the interfacial temperature at the inner wall has an upper limit of the vessel melting temperature. This may not be entirely accurate due to the composition of the metallic layer and the degree to which the vessel wall has been depleted. As materials join the metallic layer, a eutectic composition may form. This eutectic fluid may have thermal properties different than those of either the metallic layer or the vessel wall. Also, it is possible for a “liquid crust” to form at the interface of the metallic pool and the vessel wall. This crust layer would collapse and reform as the vessel wall is depleted, changing the heat transfer characteristics in that region. For the purposes of this model, however, these effects have been neglected and the heat transfer is modeled as above.

2.3 Model Equations and Parameters

2.3.1 General Parameters

Table 2-1: General parameter list

Variable	Description	Units
$\dot{Q}_c$	Volumetric decay heat generated in oxide pool	W/m^3
$\dot{Q}_m$	Volumetric decay heat generated in metallic layer	W/m^3
H_{cor}	Height of oxide pool, including crust thickness	m
V_{cor}	Volume of corium pool and crust	m^3
V_m	Volume of metallic layer	m^3
$A_{c,up}$	Surface area of upward facing oxide crust layer	m^2
$A_{c,sd,\theta}$	Surface area of side & downward facing oxide crust w.r.t angular position	m^2
$A_{m,up}$	Surface area of upward facing metallic layer	m^2
$A_{m,dn}$	Surface area of downward facing metallic layer	m^2
$A_{m,sd}$	Surface area of side facing metallic layer	m^2
A_s	Total surface area of interior structures	m^2
k_p	Thermal conductivity for oxide pool	W/m/K
k_c	Thermal conductivity for crust material	W/m/K
k_v	Thermal conductivity for vessel	W/m/K
ε_s	Emissivity of reactor internal structures	--
ε_c	Emissivity of oxide crust	--
ε_t	Emissivity of metallic layer	--
T_{cor}	Melting temperature for oxide pool materials	K
T_{ves}	Melting temperature for vessel wall	K
T_s	Temperature of internal structures	K
T_{sat}	Saturation temperature of coolant	K
$h_{p,up}$	Upward facing heat transfer coefficient from oxide pool	W/ m^2/K
$h_{p,sd,\theta}$	Side & downward facing heat transfer coefficient from oxide pool w.r.t	W/ m^2/K
$h_{m,up}$	Upward facing heat transfer coefficient from metallic layer	W/ m^2/K
$h_{m,sd}$	Side & downward facing heat transfer coefficient from metallic layer	W/ m^2/K
C_{boil}	Boiling constant [13] $C_{boil} = \left(\frac{g(\rho_{liq}-\rho_{vap})}{\sigma_{liq}}\right)^{0.5}\left(\frac{Cp_{liq}}{Pr_{liq}*1000*h_{fg}*Csf}\right)^3\left(\mu_{liq}*1000*h_{fg}\right)$	W/m^2/K^3
σ	Stefan-Boltzmann constant	W/m^2/K^4

2.3.2 Oxide Pool

Table 2-2: Oxide pool parameter list

Variable	Description	Units
$q''_{p,up}$	Upward facing heat flux from oxide pool to crust	W/m^2
$q''_{p,sd,\theta}$	Side & downward facing heat flux from oxide pool to crust	W/m^2
$q''_{c,up}$	Upward facing heat flux from oxide crust to RV internal structures	W/m^2
$q''_{c,sd,\theta}$	Side & downward facing heat flux from oxide crust to vessel wall	W/m^2
T_p^{max}	Maximum temperature of molten oxide pool	K
$T_{c,up}$	Temperature of upper oxide crust surface	K
$T_{c,sd,\theta}$	Temperature of oxide crust/vessel wall interface w.r.t. angular position	K
$T_{v,\theta}^{out}$	Temperature of cooled exterior of vessel wall w.r.t. angular position	K
$\delta_{c,up}$	Thickness of oxide crust above oxide pool	m
$\delta_{c,sd,\theta}$	Thickness of oxide crust to the side and below oxide pool	m
$\delta_{v,\theta}$	Thickness of vessel wall w.r.t. angular position	m
H_p	Height of oxide pool (excluding crust thicknesses)	m

Table 2-3: Oxide pool equation list

$$q''_{p,up} = h_{p,up}\left(T_p^{max} - T_{cor}\right) \quad \text{p1}$$

$$q''_{c,up} = \frac{k_c}{\delta_{c,up}}\left(T_{cor} - T_{c,up}\right) + \frac{1}{2}\dot{Q}_c * \delta_{c,up} \quad \text{p2}$$

$$q''_{c,up} = q''_{p,up} + \dot{Q}_c * \delta_{c,up} \quad \text{p3}$$

$$q''_{c,up} = \sigma\left({T_{c,up}}^4 - {T_s}^4\right) * \left(\frac{1}{\varepsilon_c} + \frac{1-\varepsilon_s}{\varepsilon_s} * \frac{A_{c,up}}{A_s}\right)^{-1} \quad \text{p4}$$

$$q''_{p,sd,\theta} = h_{p,sd,\theta}\left(T_p^{max} - T_{cor}\right) \quad \text{p5}$$

$$q''_{c,sd,\theta} = \frac{k_c}{\delta_{c,sd,\theta}}\left(T_{cor} - T_{c,sd,\theta}\right) + \frac{1}{2}\dot{Q}_c * \delta_{c,sd,\theta} \quad \text{p6}$$

$$q''_{c,sd,\theta} = q''_{p,sd,\theta} + \dot{Q}_c * \delta_{c,sd,\theta} \quad \text{p7}$$

$$q''_{c,sd,\theta} = \frac{k_v}{\delta_{v,\theta}}\left(T_{c,sd,\theta} - T_{v,\theta}^{out}\right) \quad \text{p8}$$

$$q''_{c,sd,\theta} = C_{boil}\left(T^{out}_{v,\theta} - T_{sat}\right)^3 \quad \text{p9}$$

$$\dot{Q}_c * V_{cor} = q''_{c,up} * A_{c,up} + \sum_{\theta} q''_{c,sd,\theta} * A_{c,sd,\theta} \quad \text{p10}$$

$$H_{cor} = H_p + \delta_{c,up} + \delta_{c,sd}|_0 \quad \text{p11}$$

2.3.3 Metallic Layer

Table 2-4: Metallic layer parameter list

Variable	Description	Units
$q''_{m,up}$	Upward facing heat flux from light metal layer to internal structures	W/m^2
$q''_{m,sd}$	Heat flux from light metal layer to surrounding side vessel wall	W/m^2
$q''_{m,dn}$	Heat flux from upper oxide crust into bottom of light metal layer	W/m^2
$T_{m,up}$	Temperature of upper surface of light metal layer	K
$T_{m,dn}$	Temperature of oxide crust/light metal layer interface	K
$T^{out}_{v,m}$	Temperature of cooled exterior of vessel wall next to light metal layer	K
$\delta_{v,m}$	Thickness of vessel wall surrounding light metal layer	m
H_m	Height of light metal layer	m

Table 2-5: Metallic layer equation list

$$q''_{m,sd} = h_{m,sd}\left(T_{m,dn} - T_{ves}\right) \quad \text{m1}$$

$$q''_{m,sd} = \frac{k_v}{\delta_{v,m}}\left(T_{ves} - T^{out}_{v,m}\right) \quad \text{m2}$$

$$q''_{m,sd} = C_{boil}\left(T^{out}_{v,m} - T_{sat}\right)^3 \quad \text{m3}$$

$$q''_{m,up} = h_{m,up}\left(T_{m,dn} - T_{m,up}\right) \quad \text{m4}$$

$$q''_{m,up} = \sigma\left({T_{m,up}}^4 - {T_s}^4\right) * \left(\frac{1}{\varepsilon_t} + \frac{1-\varepsilon_s}{\varepsilon_s} * \frac{A_{m,up}}{A_s}\right)^{-1} \quad \text{m5}$$

$$\dot{Q}_m * V_m + q''_{m,dn} * A_{m,dn} = q''_{m,up} * A_{m,up} + q''_{m,sd} * A_{m,sd} \quad \text{m6}$$

2.4 Modeling Assumptions

Similar to the approach presented in Theofanous (FIBS) [8], certain pre-conditions are assumed of the current model. First, the pool is well formed and fully relocated to the lower head. Second, the vessel has been depressurized to be even with the 2 bar containment scenario. Next, it is assumed the flow surrounding the reactor vessel is uniform and unhindered. As well, the formation of the melt pool did not cause any jets or other imbalanced attacks on the interior of the reactor vessel. The well-formed assumption also dictates a solid crust with full contact against the vessel wall. This last assumption allows for conduction to be the dominant heat transfer mechanism through the ceramic crust and into the vessel wall.

Overall the model calculates steady state values of a given core loading, decay heat (time dependent) and lower head geometry. Derivation methods utilize static layer geometries and material properties for the moment and the model maintains a two-directional division of heat fluxes in both the oxide pool and light metal layers. Furthermore, it is assumed that the crust interfacial temperatures in the oxide pool remain at the melting point of corium throughout our calculations. Specifically, in the light metal layer the assumed behavior is that of no volumetric heat generation, i.e. heat transfer in the layer is driven solely by the rising heat flux from the oxide pool. However, a volumetric heat generation value in the light metal layer equal to about 10% of that of the oxide pool is utilized.

Another consequence of a steady state assumption is considered when deriving the heat transfer equations for the model. Generally, heat transfer between two surfaces includes a term for phase change such as $q''_{cond} = -k\frac{dT}{dx} + \rho H_f v_{abl}$ where v_{abl} represents the ablation velocity. Since the developed model calculates steady state values, any phase changes in the crust or vessel structure are assumed to have occurred, rendering the ablation term zero. Additionally, as previously stated the material properties are static with respect to time and temperature. This includes the thermal conductivity, which, in the previously presented equation, allows for the thermal conductivity to move outside of the derivative term. This reduces the order of the model set and simplifies the solution structure.

In order to achieve the desired calculation times, the model must maintain a lumped parameter view of the scenario. However, the informational output is increased by subdividing the two layers into separate entities. In the oxide pool the body is divided angularly measured up from the lowest point. This allows an angular parameter distribution as well as a basis for tracking failure locations. In the light metal layer there exist horizontal nodes in order to better characterize the wall heat transfer using the chosen correlation set. These segments act independently of one another and have been modeled by a repetition of certain portions of the equation set per segment.

2.5 Correlations

The correlations used in this study are the ACOPO [14] correlations for the oxide pool, both the upward and side facing heat transfer, for hemispherical scenarios and the COPO (Kymäläinen) [15] [16] correlation for elliptical geometries. The Globe-Dropkin [17] model was used for the top of the metallic layer and the Chawla-Chan [18] correlation for the heat transfer from the side of the metallic layer. Table 2-6 outlines the equations for the correlations used in the model.

When choosing convective heat transfer correlations it is important to understand the conditions on which they were based and the implications of their ranges of applicability. Convective flow is the dominant heat transfer mechanism in the oxide pool. As such, temperature differences from the center of the pool to the boundaries drives movement of both material and heat within the lower head. The convective motion creates a churning effect where material moves from the middle of the pool up upwards towards the boundary and then falls off to the side nearest the vessel wall where the heat removal due to the surrounding coolant cools the fluid as it returns to the bottom of the vessel. Many correlations have been developed by using water as an experimental fluid. Water can have a Prandtl number of up to 7 which is significantly higher than the values for corium of approximately 0.5 as seen in this model. Lower Prandtl numbers $\left(Pr = \frac{Cp*\mu}{k}\right)$, denote fluids with lower viscosities. Lower viscosity improves thermal conductivity which would improve conductive heat transfer, but lower viscosity also means that the fluid returning from the sides of the vessel towards the middle is able to displace a larger amount of hot

fluid due to the lower resistance. This ultimately leads to a trend towards lower heat transfer in the bottom regions of a vessel head filled with lower-Prandtl number fluid.

Regardless of the Prandtl number, it has been shown (Nourgaliev & Dinh) [19] that the effect of Prandtl number on Nusselt number results is minimized in lower Rayleigh number regions (~10^{10}). Uncertainties can increase dramatically, however, when moving to higher Rayleigh number ranges, especially when departing from the original correlation's development range. Therefore, in order to minimize uncertainty it is important to not only consider the Prandtl number range of applicability but, if developed for water, the Rayleigh number range in order to stay within tolerance. If the correlation was developed using high Rayleigh number tests (10^{14}-10^{16}) then the uncertainty will be further minimized.

To that effort, the ACOPO range of applicability includes high Rayleigh numbers and is as such suitable for use in the oxide pool of this model for hemispherical situations. Since the COPO (Kymäläinen) correlation was specifically developed for elliptical cavities as well as for high Rayleigh number ranges, it is the correlation of choice for elliptical scenarios. The Rayleigh number observed in the light metal layer is less than that of the oxide pool and as such the Globe-Dropkin is not only suitable on Rayleigh number but for Prandtl range as well.

The Chawla-Chan correlation was developed in 1982 for convection in vertical, straight-sided containers. Since the metallic layer largely exists in vertical sections of the reactor vessel, the correlation was chosen to model the Nusselt number for this layer. The correlation is based off of the modified Rayleigh number, similar to the other metallic layer correlation, Globe-Dropkin. In the heat transfer coefficient derived from the Chawla-Chan correlation, however, the height used is replaced with a factor *y*. This *y* factor is, in fact, the total height of the metallic layer minus the height of the location of the heat transfer. Figure 2-3 demonstrates the resultant coefficient values for a sample scenario with a simulated segmented metallic layer to the right. As is shown, the value of the heat transfer is asymptotic near the maximum height. This would of course lead to infinite heat transfer in that region. The actual behavior of the boundary layer is such that the heat transfer starts from zero, where there is no material to transfer heat, and continues to a local maximum before following the correlated path back down to a minimum value. This behavior is

shown by the dashed line and represents an approximation made in the current model. Instead of using segment maximum heights to determine the *y* factor, local averages are computed, further splitting the segment into subsections and determining a characteristic coefficient value for the total segment. This process replicates the behavior of the boundary layer and prevents unrealistic infinite heat transfers at the top of the metallic layer.

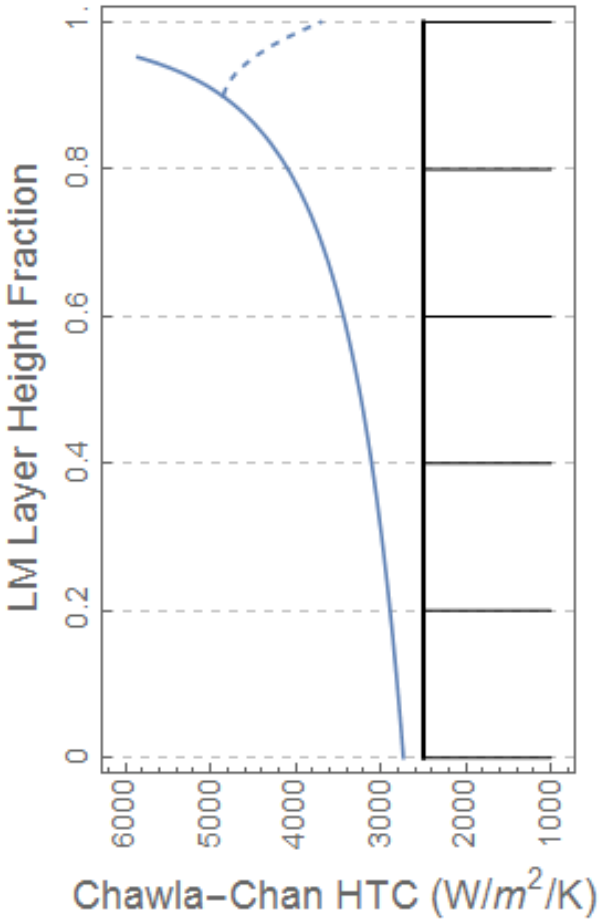

Figure 2-3: Chawla-Chan correlation visualization

In the development of the Chawla-Chan correlation, it was determined that in order for the scaling analyses made to be valid, the following relation had to be satisfied:

$$\epsilon = \frac{\nu^{1/3}}{[(\beta * \Delta T_m + 3\alpha)g]^{2/3}} \frac{Q_m}{\rho C_p \Delta T_m} \ll 1 \Longrightarrow 1.5 * 10^{-7} * \frac{Q_m}{{\Delta T_m}^{5/3}} \ll 1$$

By substituting in material properties for the metallic layer (Appendix B), the relation is reduced above where Q_m is the heat generated in the metallic layer and ΔT_m is the vertical temperature difference in the layer. By assuming low volumetric heat generation values in the metallic layer as compared to the oxide pool, approximately 10%, and recognizing a temperature difference on the order of 10^2, this relation is satisfied.

Table 2-6: List of correlations used

Type	Direction	Correlation & Equation
Oxide Pool Hemispherical	Upward	ACOPO: $Nu = 0.3 * Ra^{0.233} * Pr^{0.064}$
	Side/Down	ACOPO: $Nu = 0.3 * Ra^{0.22}$
Oxide Pool Hemispherical	Upward	INEEL: $Nu = 2.4415 * Ra^{0.1772}$
	Side/Down	INEEL: $Nu = 0.1857 * Ra^{0.2304} \left(\frac{H}{R}\right)^{0.25}$
Oxide Pool Elliptical	Upward	COPO: $Nu = 0.345 * Ra^{0.233}$ (Kymäläinen)
	Sideways	COPO: $Nu = 0.85 * Ra^{0.19}$ (Kymäläinen)
	Downward	COPO: $Nu = 0.54 * Ra_c^{0.182} \left(\frac{H_c}{R_c^{**}}\right)^{0.25}$ (Kymäläinen)
Metallic Layer	Upward	Globe-Dropkin: $Nu = 0.069 * Ra_p^{0.333} * Pr^{0.074}$
	Side/Down	Chawla-Chan: $Nu = 0.508 * Ra_p{}'^{0.25} * Pr^{0.25} \left(\frac{20}{21} + Pr\right)^{-0.25}$
Angular Position	Side/Down	Park & Dhir: $f_\theta = \begin{cases} b_1 * \sin^2(\theta) + b_2, & \theta < \theta_0 \\ b_1 * \sin^2(\theta_0) + b_2, & \theta \geq \theta_0 \end{cases}$, $b_1 = \frac{9.12(1-\cos(\theta))}{8 - 9\cos(\theta) + \cos(3\theta)}$, $b_2 = 0.24$
CHF	Side/Down	ACOPO: $q''_{c,up} = A_{CHF} + B_{CHF}\theta + C_{CHF}\theta^2 + D_{CHF}\theta^3 + E_{CHF}\theta^4$ $A_{CHF} = 4.9 * 10^5, B_{CHF} = 3.02 * 10^4, C_{CHF} = -8.88 * 10^2,$ $D_{CHF} = 13.5, E_{CHF} = -6.65 * 10^{-2}$
Rayleigh Number	Ra	$Ra = \frac{g * \beta * \dot{Q} * H_{eff}^5 * \rho}{\alpha * \mu * k}$, $H_{eff} = effective\ pool\ height$
	Ra_c	$Ra = \frac{g * \beta * \dot{Q} * H_c^5 * \rho}{\alpha * \mu * k}$, $H_c = height\ of\ pool\ curvature$ $^{**}R_c = radius\ of\ curvature$
	Ra_p	$Ra_p = Gr * Pr = \frac{g * \beta * H^3 * \Delta T}{(\mu/\rho)^2} * \frac{Cp * \mu}{k}$
	$Ra_p{}'$	$Ra_p{}' = \frac{g * \beta * y^3 * \Delta T}{(\mu/\rho)^2} * \frac{Cp * \mu}{k}$

Even though most results were obtained using the ACOPO correlation presented above, the INEEL revision correlation (discussed in Section 4.4) is presented for its use in the quasi-transient results. This correlation was a best fit estimate using digitized data of early ACOPO experiment results. Its origin and justification is presented in Appendix B of the INEEL revision to the original DoE research compiled by Rempe et al [9].

2.6 Solution Initialization

2.6.1 Material Properties & Geometry

The developed software assesses a given core loading condition and computes varied results for analysis. In the initialization process, certain quantities or relations are pre-defined for future use. First, the material properties of the system are defined. These values range from corium properties such as density, heat conduction, and melting point to coolant saturation parameters. The input characteristics used for the results of this study were taken from the ERI input data used by Esmaili et al. [7] in the IVRAM development in 2005. This set of material properties can be changed for different situations as dictated by system pressure or temperature. For the cases considered in this project, however, the properties were kept constant.

Following the material property initialization, the program defines the governing equations for decay heat, pool geometry, and basic dimensionless quantities. The geometric equations have been developed for maximum utility by requiring only the lower head radius and an ellipse ratio for full characterization. The ellipse ratio is defined as the ratio of the long to the short axis for the characteristic cross-section of the lower head. For hemispherical shapes such as the AP1000, this ratio is one and for SMR designs this ratio can be thought of as around three. Following the definition of the lower head radius and ellipse ratio, the geometric equations of the program can calculate angle angular position from vessel bottom center and thus layer volume and surface area using layer height inputs. This formulation maximizes flexibility concerning geometric input as well as maximizes information output while limiting the required inputs.

Table 2-7 outlines the set of geometric equations derived for this model. H_{crit} refers to the “equator” of the vessel, or, the point where the curvature ends and the side walls are vertical surfaces. Following the definition for H_{crit} using the radius and ellipse factor, the volume and surface area of both the oxide and metallic layers may be calculated. Note that when one layer exceeds the critical height, the volume equations begin to calculate cylindrical volume whereas the surface area equation for the elliptical section ends in order to leave the rest of the area calculation to the cylindrical version. Using this set of equations, the volume, surface area, and radius for any angle, or range of angles, may be

computed for either hemispherical or elliptical lower head structures. By manipulating the radius equation, the angle from the bottom center of the lower vessel may be found at any height. This is accomplished by solving for the angle in the equation:

$$\theta'(h) \rightarrow r_{ell}(\theta) * \cos(\theta) = Min[h, H_{crit}]$$

$$\theta(h) = \theta'(h) + \begin{bmatrix} 0 & h \leq H_{crit} \\ \tan^{-1}\left(\frac{h}{R_{LP}} - \frac{1}{f_{LP}}\right) & h > H_{crit} \end{bmatrix}$$

As can be seen in the equations, setting f_{LP} to 1 simplifies all the relations to those of the hemispherical special case. Finally, the last geometric value needed for use in the COPO correlations is the radius of curvature for an elliptical lower head. The radius of curvature at a certain point along a Euclidian curve is the radius of the circle that is tangential and has the same curvature as that point. The definition of the radius of curvature is the inverse of the curvature itself and is presented below:

$$R_c = \frac{1}{|\kappa|}, \qquad \begin{matrix} \kappa = curvature \\ R_c = radius\ of\ curvature \end{matrix}$$

For an ellipse defined parametrically, the equation for curvature is given below:

$$For \begin{matrix} x = f(\phi) = a\cos\phi \\ y = g(\phi) = b\sin\phi' \end{matrix} \qquad \kappa = \frac{|x'y'' - y'x''|}{\left(x'^2 + y'^2\right)^{3/2}}$$

Substituting model coefficients and definitions and simplifying:

$$For \begin{matrix} a = r_{LP} \\ b = \frac{r_{LP}}{f_{LP}} \\ \phi = \theta - \frac{\pi}{2} \end{matrix} \Longrightarrow \kappa = \frac{{f_{LP}}^2}{r_{LP}\left({f_{LP}}^2\cos^2\theta + \sin^2\theta\right)^{3/2}}$$

When examining a circle, the radius of curvature is simply the circle radius. By setting f_{LP} to 1, the curvature becomes:

$$\kappa = \frac{1}{r_{LP}(1\cos^2\theta + \sin^2\theta)^{3/2}} = \frac{1}{r_{LP}} \Longrightarrow R_c = \frac{1}{|\kappa|} = r_{LP}$$

Table 2-7: Geometric equation set

$$H_{crit} = \frac{R_{LP}}{f_{LP}} \tag{a1}$$

$$V_H(H_{Lo}, H_{Hi}) = \int_{Max[0,H_{crit}-H_{Lo}]}^{Max[0,H_{crit}-H_{Lo}]} \pi({R_{LP}}^2 - {f_{LP}}^2 x^2)dx \tag{a2}$$

$$V_{OX}(H_{OX}) = V_H(0, H_{OX}) + Max\left[0, \int_{H_{crit}}^{H_{OX}} \pi\left({R_{LP}}^2\right)dx\right] \tag{a3}$$

$$V_{LM}(H_{OX}, H_{LM}) = V_H(H_{OX}, H_{OX} + H_{LM}) + Max\left[0, \int_{H_{crit}}^{H_{OX}+H_{LM}} \pi\left({R_{LP}}^2\right)dx - Max\left[0, \int_{H_{crit}}^{H_{OX}} \pi\left({R_{LP}}^2\right)dx\right]\right] \tag{a4}$$

$$r_{ell}(\theta) = \begin{cases} \frac{{R_{LP}}^2}{f_{LP}}\left(\frac{{R_{LP}}^2({f_{LP}}^2\cos^2(\theta) + \sin^2(\theta))}{{f_{LP}}^2}\right)^{-0.5} & 0 \le \theta \le \frac{\pi}{2} \\ \frac{R_{LP}}{\cos(\theta - \frac{\pi}{2})} & \frac{\pi}{2} < \theta \le \pi \end{cases} \tag{a5}$$

$$A_{flat}(\theta) = \pi\left(r_{ell}\left(Min\left[\theta, \frac{\pi}{2}\right]\right) * \sin\left(Min\left[\theta, \frac{\pi}{2}\right]\right)\right)^2 \tag{a6}$$

$$A1_{ell}(\theta_1, \theta_2) = \begin{cases} \int_0^{2\pi}\int_{\theta_1}^{\theta_2} \sqrt{\frac{1}{2}{R_{LP}}^2\left({R_{LP}}^2 + \frac{{R_{LP}}^2}{{f_{LP}}^2} + \left({R_{LP}}^2 - \frac{{R_{LP}}^2}{{f_{LP}}^2}\right)\cos(2\theta)\right)\sin^2(\theta)}\ d\theta\ d\phi & 0 \le \theta_2 \le \frac{\pi}{2} \\ \int_0^{2\pi}\int_{\theta_1}^{\pi/2} \sqrt{\frac{1}{2}{R_{LP}}^2\left({R_{LP}}^2 + \frac{{R_{LP}}^2}{{f_{LP}}^2} + \left({R_{LP}}^2 - \frac{{R_{LP}}^2}{{f_{LP}}^2}\right)\cos(2\theta)\right)\sin^2(\theta)}\ d\theta\ d\phi & \theta_1 \le \frac{\pi}{2} \end{cases} \tag{a7}$$

$$A2_{ell}(\theta_1, \theta_2) = 2\pi{R_{LP}}^2\left(\tan\left(Max\left[0, \theta_2 - \frac{\pi}{2}\right]\right) - \tan\left(Max\left[0, \theta_1 - \frac{\pi}{2}\right]\right)\right) \tag{a8}$$

$$A_{ell}(\theta_1, \theta_2) = A1_{ell}(\theta_1, \theta_2) + A2_{ell}(\theta_1, \theta_2) \tag{a9}$$

$$A_{cyl}(h) = 2\pi R_{LP} * h \tag{a10}$$

2.6.2 Dimensionless Numbers & Angular Position Correlation

After the decay heat and geometry setup, the code defines correlated values such as Nusselt number and angular factors to be used when calculating downward facing values in the oxide pool. At this stage, the program defines a library of possible correlations for all corium layers and directions. In the solution loop, the program will call a pre-defined correlation and replace the dummy variables with pertinent run values for Rayleigh or Prandtl number, for example. This setup allows for a structure involving conditional assignment of correlations based on individual run parameters. This "best-fit" approach may be a method to reduce uncertainty in future versions of the code by utilizing correlations in their maximum range of applicability. Based on the geometry for the run, the necessary set of heat transfer correlations is chosen from the previously discussed options.

Next, in order to improve stability and decrease nonlinearities in the solution matrix, the height used to calculate the Rayleigh number may be edited depending on the Nusselt correlation used. Nusselt number correlations in the oxide pool are generally of the form $Nu = C * Ra^b$ where b is generally in the range of 0.15-0.3. Since the Rayleigh number, Ra, is proportional to pool height to the 5th power, the following relationship is established:

$$Nu \propto Ra^b, Ra \propto H_p^5 \Longrightarrow Nu \propto H_p^{5b}$$

Thus, in correlations where b > 0.2, a superlinear relation to pool height is created. Due to pool height subsequently informing all equations involving convective heat transfer, this makes the system of equations highly nonlinear. The problem may be easily mitigated by realizing that pool height is an extremely high fraction of total corium height. By assuming $\delta_{c,up} \sim \delta_{c,dn} \ll H_p$, the pool height term in the Rayleigh number may be replaced with an effective height: $H_{eff} = H_{cor}^{0.25} H_p^{0.75}$. By making this substitution in correlations where b > 0.2, a high number of nonlinearities are avoided. Additionally, the error associated with this substitution may be shown as negligible:

$$\frac{\%E}{100} = \frac{H_{eff} - H_p}{H_p} = \frac{x^{0.75} H_{cor} - x H_{cor}}{x H_{cor}} = \frac{1}{x^{0.25}} - 1$$

Substituting the generally observed 0.97 as the pool fraction of total corium height:

$$\%E = 100\left(\frac{1}{0.97^{0.25}} - 1\right) = 0.76\%$$

Next, the angular correlation is defined so that quantities such as the Nusselt number may be calculated at different angular positions on the lower head by virtue of the following relation.

$$Nu_\theta = f_\theta * Nu$$

Figure 2-4 shows a comparison between two considered correlations for the f_θ angular factor. In this model the Park & Dhir [10] model was chosen over the Mini-ACOPO [20] version. This was due to the continuous nature of the function in addition to the belief the P&D correlation would perform better in ellipsoidal scenarios than the mACOPO version. As referenced earlier, this factor models the increasing Nusselt number with increasing angular position which in turn increases the heat transfer coefficient and, thus, the total heat transfer in the segment.

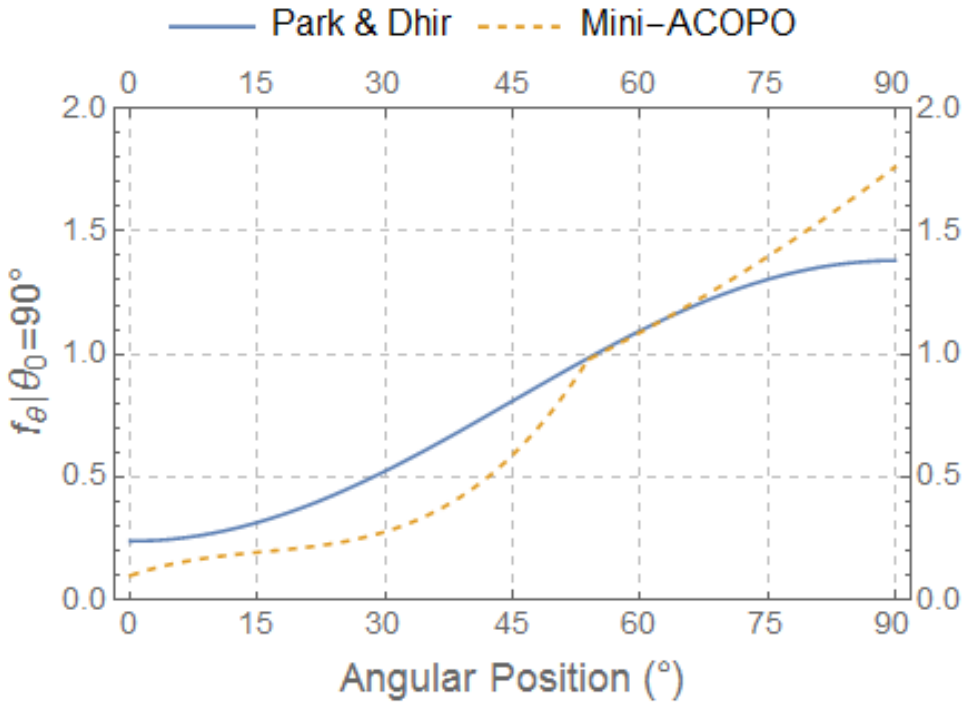

Figure 2-4: Comparison of angular dependence correlations

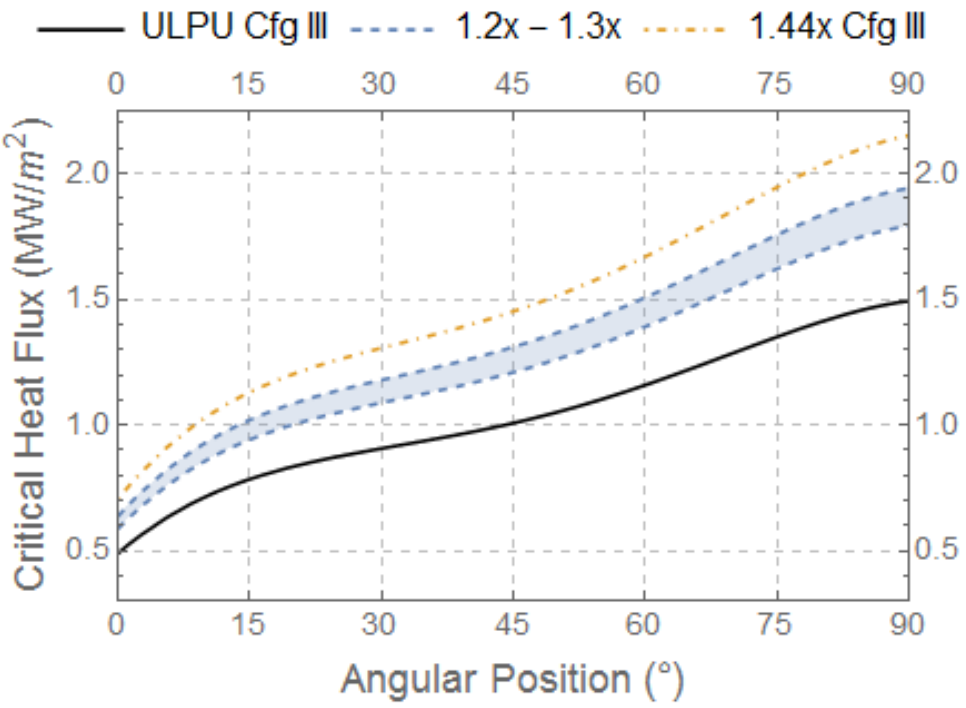

Figure 2-5: Multipliers of ULPU configuration III CHF correlation

2.6.3 CHF Correlation

Finally in the initialization segment of the program the CHF correlation is set. The correlation used is based off of configuration III of the ULPU experiments performed at UCSB [11]. This correlation defines coefficients for a 4th degree function of angular position to define CHF along the vessel exterior. The configuration III tests were performed to create data for the AP600 reactor. Future configurations IV and V were later tested in order to update the experimental setup to differences in geometry with the AP1000. Included in these updates were more detailed baffle geometry and a more defined natural circulation parameters. Ultimately, the work in configuration IV and V resulted in higher observed CHF limits than that of configuration III. To compensate for this, Esmaili [7] showed in their model setup that a factor of 1.44, when applied to the configuration III correlation, adequately fits the data received from the IV and V tests up until approximately 70°. Beyond this point the CHF limit was overstated as beyond 2.0 MW/m^2. The 1.44

factor was, in part, derived from declarations from Westinghouse that the results of the IV testing showed a 20-30% increase from III and that the V tests showed a 20% increase from IV. For the NCSU model, a scalar factor of 1.3 was selected in order to appropriately raise the CHF limit from the configuration III data but also to remain conservative in the higher angular positions of the vessel. Figure 2-5 showcases the configuration III correlation and the various scalar factors considered.

2.7 Solution Procedure

Once the initialization has finished, the model proceeds into the solution structure. The inputs for the model may be divided into two categories, reactor parameters and run parameters. The reactor parameters are the time of interest (time from reactor shutdown used to calculate decay heat), the reactor lower head radius, the ellipse factor for the lower head geometry, and the initial core loading in the form of oxide pool and metallic layer masses. The model has functionality to accept core loading volumes instead, but all runs calculated for the purposes of this report began with core mass inputs. The run parameters include multipliers to four parameters: decay heat, oxide pool mass, metallic layer mass, and ellipse ratio. These factors allow different views of similar situations and offer a means of adapting scenarios for better insight into possible phenomena.

Using the input mass of each layer and the provided material densities, the volume equations (a3) and (a4) are used to solve for the height of the individual layers. This process may be reversed in the case where layer height is an input rather than layer mass. Once the layer heights are established the meshes are created for both the oxide pool and the metallic layer. The oxide pool is divided into $n\theta$ angular segments, typically 24, and the metallic layer into nH horizontal slabs, typically 16. These divisions are equally sized for both layers. The metallic layer is then further subdivided in order to compute average height values for each main segment for use in calculating the Chawla-Chan heat transfer coefficient (see section 2.4).

Following the mesh initialization the geometry of the layers is calculated. The surface area for the top of the oxide crust layer, equal to the surface area for the bottom of the metallic layer, as well as the top of the metallic layer are calculated using equation (a6) with $A_{flat}(\theta)$ solved for the maximum angle of the respective layers. The surface areas of

the segments of both layers in contact with the vessel wall are calculated using equations (a7), (a8), and (a9). For each segment, the span of its minimum and maximum angle are input to the A_{ell} function in order to receive the incremental surface area up the side of the vessel. Following the geometric calculations, an interstitial output shows a grid of all areas, volumes, heights, and section angles for code troubleshooting. Using the calculated volumes, the total energy splitting for the layers is calculated with the assumption that the heat generation in the metallic layer is 10% that of the oxide pool. The sum heat generation in the two layers is equal to the total decay heat found by the plant thermal power rating and time of interest for the run.

Next, the dimensionless numbers and heat transfer correlations are loaded in where previous dummy parameters are replaced for scenario details. Then, the equation models are loaded with, again, dummy parameters swapped for scenario specific solution variables. These equations form a *n* x *n* matrix of linear equations where *n* is equal to 9 + 6p + 3m where p is the number of oxide pool segments and m is the number of light metal layer subdivisions. These calculations were performed with 24 oxide pool segments and 16 light metal subdivisions for a total of 201 equations. The equation matrix is solved using the Newton method for linear approximation of nonlinear systems [12]. The basic premise of this method is to use successive tangential values to a root guess of a nonlinear function in order to eventually arrive at the true root of the function. As seen in Figure 2-6, the function's root lies around 1.5. With an initial guess of 2.5, the tangent line is calculated and intersects with the x-axis. The corresponding value of the function to that intersection is the next guess for the root. The process continues until convergence.
The governing equation, therefore, for moving from guess to guess is:

$$x_{n+1} = x_n - \frac{f(x_n)}{f'(x_n)}$$

This method relies on an accurate initial guess in order to avoid issues such as overshooting the root or finding a secondary solution in a multi-root equation. In order to avoid these issues for sensitive parameters, trust regions are established which bound the root within a given span of values. In order to determine the limits of this region, either logical boundaries can be given (no negative temperatures, for instance) or a fit function

may be utilized in the case of heat flux. This fit function is based off of empirical observations of the shape of the heat flux curve as well as CHF correlations and sets the upper bound in an attempt to maximize the efficiency of the solution method.

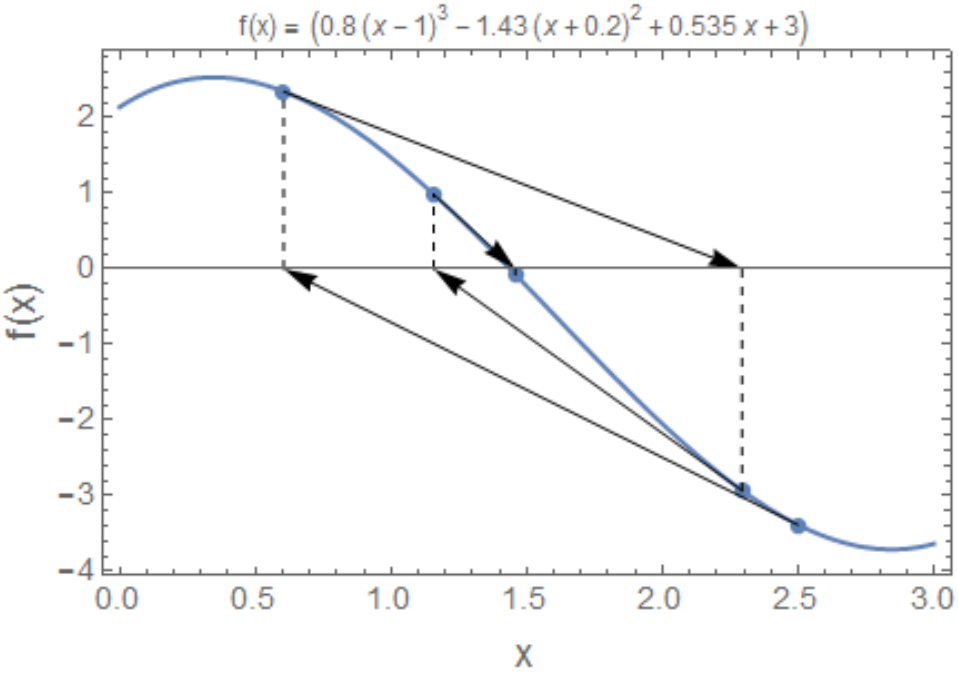

Figure 2-6: Sample Newton method ($x_0 = 2.5$)

The matrix is then solved one a two-pass system. The first pass assumes a constant vessel thickness and allows the crust-vessel interfacial temperature to exceed the vessel melting point. The second pass notes the location in both the oxide and metallic layers where this interfacial temperature exceeds vessel melting and switches variables to instead maintain a constant interfacial temperature of the melting point and instead solve for now a lower vessel thickness. The results are then exported to the resultant tables and figures seen in the following section.

There are multiple types of results which may be output from the model. Individual figures for a single run's oxide and light metal layers are available as well as tables for dimensionless numbers, angular mesh and metallic layer subdividing data, geometric quantities, and local constants such as C_{boil} [13]. More useful, however, are the plots which

show the results across both layers simultaneously. These figures are normalized from 0 to 2 where 0 is the bottom angle of the oxide pool, 1 is the peak angle value for the oxide pool, 1.5 is the middle height of the metallic layer, and 2 is the maximum metallic layer height. These plots, including heat flux, thermal margin, and vessel thickness, allow for observation of trends across the vessel structure.

3 VERIFICATION AND VALIDATION

3.1 V&V Importance and Benchmarks

Model verification and validation is an important consideration in modern research procedures. In the nuclear field especially, research relies on computational process models, mathematical physics models, experimental data from both separate and integral effect tests, and finally full-system simulation. With no full system experiments possible, the results from all these processes must inform each other in an attempt to quantify and ultimately lower the associated results uncertainty. In order for this process to work, however, the results of one particular model, simulation, or experiment must be assessed for accuracy and reliability before they can be deemed acceptable for use in supporting other methods. Part of that assessment is the *verification* that the results of a computational model accurately and reliably represent the mathematical and physical formula foundation and the *validation* that the formulas and processes used to produce the results suitably represent the real-world phenomena being modeled [21]. For this work, the basis for verification will be the comparison of the model results to benchmark cases such as the IVRAM model developed by Esmaili et al. The developed NCSU model differs in correlation and relies on a simpler mathematical model than that found in IVRAM but otherwise represents an identical severe accident scenario for the Westinghouse AP1000 reactor.

The specific branch of verification of interest in this work is code verification. This sub-category can be further divided into the previously mentioned tenants of verification, accuracy and reliability or repeatability. In order to verify code accuracy, a variety of methods may be implemented. The two most common approaches involve the use of analytical or manufactured solutions. In the analytic solution approach, a simplified case is

considered where a solution may be derived by hand with relative ease. This case may involve the removal of geometry elements, nicely constructed ratios between terms, or other simplifications to enable an outside solution. The code or model may then be applied to this simplified case and would be expected to reproduce the derived solution. Manufactured solutions are slightly more complicated. The method involves assuming a form of the solution to the partial differential equation or set of PDEs of interest. Then, a separate, closed, and analytic solution form is created to represent the original PDE. This solution is applied to the original equation and boundary conditions are derived from zero, maximum, or other conditions. The result is an extra source term to be added to the original PDE which, while physically unreasonable, may be used to test the numerical methods of the code. For this work, an analytic solution verification method will be used by observing a simplified geometry and analytically derived dimensionless number ratios.

The final part of verification involves the testing of a code or model's reliability or repeatability. This can be performed in a variety of ways by changing a code parameter rather than a physical or input parameter and observing any difference in the resultant solution. For this work, a comparison will be made between solutions at different discretization levels. By varying the amount of radial nodes in the oxide pool or vertical nodes in the metallic layer, the solution should change in resolution but differ by a negligible if any amount in magnitude. Additionally, the solution may be checked for correct conservation of particular values. To this extent, the conservation of heat produced in the pool may be compared to the outward heat fluxes multiplied by the respective surface areas to confirm that the code is correctly utilizing the equation set.

3.1.1 Accuracy Verification

For purposes of the analytic solution, the core melt scenario was reduced to a simplified version. In a hemispherical lower head, the height of the oxide pool was assumed to be the radius of the lower head, resulting in a maximum angular position from the bottom of the vessel of 90 degrees. There was no metallic layer above the oxide pool with the top boundary instead a radiative heat transfer condition. Additionally, with a lower head radius of 2 meters, the volume the oxide pool occupies is $16\pi/3$ cubic meters. For ease of calculation, the total decay heating in the analytic scenario was assumed to be $16\pi/3$

MWt. For the AP1000 maximum thermal power rating, this correlates to an accident timing of approximately 30 hours and results in a volumetric heat generation rate of 1 MW/m^3.

The parameters for the analytical solution are shown in the re-examination of Figure 2-1 below. By removing the light metal layer and replacing the $q''_{m,up}$ and $T_{m,up}$ terms with a radiation heat transfer boundary and T_{up}, the upper half of the scenario is realized. The lower portion requires only a change in notation from "sd" to "dn" to align with the following solution. The material properties used in the analytic solution are the same as are used in the NCSU model and are presented in Appendix B.

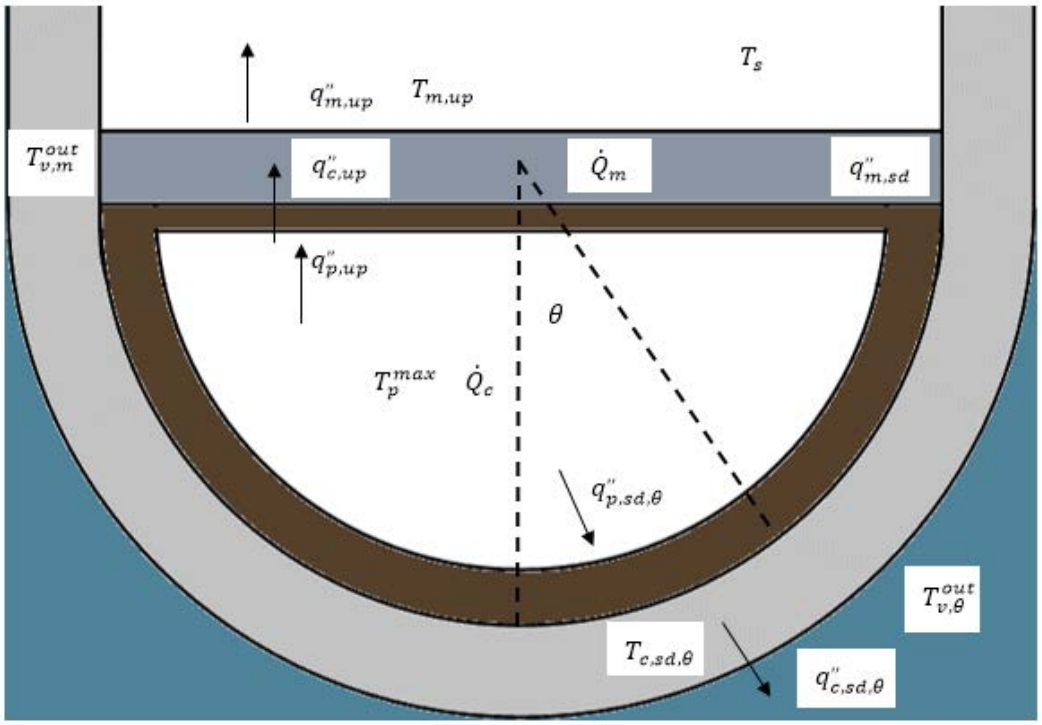

Figure 3-1: Hemispherical lower head showing heat-flux and temperature profile

The analytic solution begins with a process to solve for the maximum pool temperature using the overall heat balance equation and the assumptions made for geometry and decay heating. Using the previously covered geometry, the surface areas for the upward and downward facing regions may be calculated. Due to the layout of the pool,

the downward facing area is exactly twice the upper area: $\left(\frac{1}{2}(4\pi R^2)\ vs\ \pi R^2\right)$. The Rayleigh number, definition presented in Table 2-6, may be calculated directly by assuming the height of the entire pool as the driving metric. Next, the directional Nusselt numbers and resultant heat transfer correlations are found using the ACOPO [14] correlation. These geometric and dimensionless values may be found in the first two rows of Table 3-1, a summary of all the determined values in the analytic solution.

Table 3-1: Summary of analytically derived values

V_{cor}	A_{up}	A_{dn}	Q_{dec}	Q_{vol}
m^3	m^2	m^2	MW	MW/m^3
16.7552	12.5664	25.1327	16.7552	1.
Ra	**NU_{up}**	**NU_{dn}**	**h_{up}**	**h_{dn}**
9.742×10^{15}	1662.81	896.591	4406.46	2375.97
$q''_{p,up}$	$q''_{p,dn}$	R_q	Rs	T_{max}
W/m^2	W/m^2	--	--	K
641518.	345907.	1.8546	0.927298	3118.59
ε_{eff}	$q''_{c,up}$	$\delta_{c,up}$	T_{up}	
--	W/m^2	mm	K	
0.654545	645467.	3.94825	2065.62	
C_{boil}	$q''_{c,dn}$	$\delta_{c,dn}$	T_{dn}	δ_{ves}
$W/m^2/K^3$	W/m^2	mm	K	cm
265.298	356848.	10.9409	411.039	10.6619

Following the set-up of the problem geometry and relevant values, the maximum pool temperature may be solved directly using the overall heat balance equation

$$\dot{Q}_c * V_{cor} = q''_{c,up} * A_{c,up} + \sum_{\theta} q''_{c,dn,\theta} * A_{c,dn,\theta}$$

For ease of calculation, one assumption that can be made in the analytic case is that the downward facing heat flux is not dependent on the angular position from the bottom of the pool. Here, the surface area is assumed to be negligibly impacted by the crust thickness and, thus, is identical on both sides of the crust. Also, by observing that the left hand side is simply decay heat, the equation may be reduced to:

$$\dot{Q}_{dec} = q''_{c,up} * A_{c,up} + q''_{c,dn} * A_{c,dn}$$

The heat flux in the oxide pool may be defined using the equation:

$$q''_{p,up|dn} = h_{p,up|dn}\left(T_p^{max} - T_{int}\right)$$

Here, T_{int} is the interfacial temperature between the oxide pool and the ceramic crust formed along its perimeter. This temperature is assumed to remain constant and is modeled as the melting temperature of the corium ceramic material. Substituting into the balance equation, the pool heat fluxes and maximum pool temperature are found directly:

$$\dot{Q}_{dec} = h_{p,up}\left(T_p^{max} - T_{cor}\right) * A_{c,up} + h_{p,dn}\left(T_p^{max} - T_{cor}\right) * A_{c,dn}$$

Or

$$T_p^{max} = T_{cor} + \frac{\dot{Q}_{dec}}{h_{p,up} * A_{c,up} + h_{p,dn} * A_{c,dn}} = 3118.59\ K$$

$$q''_{p,up} = 641518\ \frac{W}{m^2}, \qquad q''_{p,dn} = 345907\ \frac{W}{m^2}$$

Next, the conduction through the upper ceramic crust is solved using the upper radiation heat transfer boundary. The equations for conduction through the crust material including its internal volumetric generation are derived in Section 2.2.1. In this step, two variables, the upper crust thickness and upper surface temperature are unknown. The following two equations provide the necessary relations to create a simple linear system:

$$q''_{p,up} + \dot{Q}_c * \delta_{c,up} = q''_{c,up} = \frac{k_c}{\delta_{c,up}}\left(T_{cor} - T_{up}\right) + \frac{1}{2}\dot{Q}_c * \delta_{c,up}$$

$$q''_{c,up} = q''_{rad} = \sigma\varepsilon_{eff}\left({T_{up}}^4 - {T_s}^4\right)$$

Where:

$$\varepsilon_{eff} = \left(\frac{1}{\varepsilon_c} + \frac{1-\varepsilon_s}{\varepsilon_s}\right)^{-1} = 0.65, \qquad T_s = 950\ K$$

Solving the two equation system algebraically and selecting the positive root yields:

$$\delta_{c,up} = 0.00395\ m, \qquad T_{up} = 2065.62\ K$$

Finally, the conduction through both the lower ceramic layer and the vessel wall may be calculated. Instead of bounding the heat transfer from the crust to a radiation condition as above, the heat flux becomes an incident conductive term on the vessel. The

heat transfer on the vessel exterior is instead bounded by an empirical convection relation. Overall, a system of three equations is created for the three variables of interest: $\delta_{c,dn}, \delta_{ves}, T_{dn}$

$$q''_{p,dn} + \dot{Q}_c * \delta_{c,dn} = q''_{c,dn} = \frac{k_c}{\delta_{c,dn}}(T_{cor} - T_{CV}) + \frac{1}{2}\dot{Q}_c * \delta_{c,dn}$$

$$q''_{c,dn} = q''_{ves} = \frac{k_v}{\delta_{ves}}(T_{CV} - T_{dn})$$

$$q''_{ves} = q''_{out} = C_{boil}(T_{dn} - T_{sat})^3$$

T_{CV} refers to the interfacial temperature between the ceramic crust and the vessel wall. It is assumed to be constant and valued at the melting temperature for the vessel. C_{boil} is an empirical constant found as part of the Rohsenow correlation [13], recalculated for SI units. This system of three equations may be solved directly to yield:

$$\delta_{c,dn} = 0.01094\ m, \qquad \delta_{ves} = 0.10662\ m, \qquad T_{dn} = 411.04\ K$$

Finally, the resultant boundary heat fluxes are:

$$q''_{c,up} = 645467\ \frac{W}{m^2}, \qquad q''_{c,dn} = 356848\ \frac{W}{m^2}$$

By using the simplified conditions as above in the developed NCSU model, the solution outputs can be compared in order to verify the code process. Before comparing results, however, it is useful to highlight one difference in the model solution and the purely analytical version. The NCSU model uses only the liquid pool height as the driving metric for the Rayleigh number. This height thus becomes a solution variable bounded by the equation $H_{cor} = H_{pool} + \delta_{c,up} + \delta_{c,dn}$. This will produce a slightly smaller Rayleigh number, affecting heat transfer values.

Table 3-2 summarizes the NCSU inputs, geometry values, and dimensionless quantities for the simplified analytic case. As shown, the Rayleigh number is indeed smaller than in the purely analytic case and, as a result, so are the Nusselt numbers and heat transfer coefficients. The final row of this table shows the heat conservation of the system to be discussed in the following section.

Finally, Table 3-3 summarizes the results from the one-layer model case. The model was run using four different angular positions along the vessel from the bottom. Since one assumption for this case was that the heat flux was not dependent on angular

position, these nodes do not produce any different results. The discretization instead showcases this ability to maintain a constant value and also was preserved to ensure ideal code behavior. All the entries in Table 3-3 show the variable, the initial guess value used by the Newton solution method (discussed in Section 2.7), and the calculated value.

Table 3-2: Input summary from one-layer analytic modelled case

A_{crust}^{up} 12.5664	$\Sigma_i A_{\theta_i}$ 25.1327	θ_{cor} 90.	
V_{cor} 16.7552	V_{LM} 0.	m_{cor} 137242.	m_{LM} 0.
$\dot{Q}_{decay}$ 1.67552×10^7	$\dot{Q}_{pool}$ $1. \times 10^6$	$\dot{Q}_{LM}$ 100000.	$q''_{CHF,max}$ 1.94173×10^6
C_{boil} 265.298	Ra_{OX} 9.37386×10^{15}	NU_{up} 1651.51	NU_{dn} 886.964
$A_{c,up} * q''_{c,up}$ 7.96985×10^6	$\Sigma[A_{c,sd} * q''_{c,sd}]$ 8.78531×10^6	Total 1.67552×10^7	Q_{decay} 1.67552×10^7

The first row of Table 3-3 shows the results for the overall pool quantities as well as the upward facing values. Rows 2-6 show the values calculated for each of the angular positions from 0°, the bottom center of the oxide pool, to the maximum pool height angle, 90°. As previously mentioned, the results are identical due to the removal of dependence on angular position.

Lastly, Table 3-4 summarizes the differences in values between the analytic and model solutions for the simplified case. As expected, the difference in Rayleigh number and pool height causes a small deviation in the results. Overall, however, the agreement is within 2% with only the upper crust calculation affected for a difference of 5%.

Table 3-3: Results summary from one-layer analytic modelled case

Var	H_{pool}	$q''_{p,up}$	$q''_{c,up}$	T_p^{max}	$T_{c,up}$	$\delta_{c,up}$
Guess	1.98	400 000	400 000	3200.	2500.	0.05
Actual	1.98466	630 056.	634 221.	3115.86	2032.75	0.00416477

Θ_i	Var	$q''_{p,sd}$	$q''_{c,sd}$	$T_{c,sd}$	T_v^{out}	$\delta_{c,sd}$	δ_v
0	Guess	125 000	175 000	1580.	380.	0.05	0.15
0	Actual	338 380.	349 556.	1600.	410.963	0.0111766	0.10885

Θ_i	Var	$q''_{p,sd}$	$q''_{c,sd}$	$T_{c,sd}$	T_v^{out}	$\delta_{c,sd}$	δ_v
1	Guess	150 000	200 000	1580.	380.	0.05	0.15
22	Actual	338 380.	349 556.	1600.	410.963	0.0111766	0.10885

Θ_i	Var	$q''_{p,sd}$	$q''_{c,sd}$	$T_{c,sd}$	T_v^{out}	$\delta_{c,sd}$	δ_v
2	Guess	275 000	325 000	1580.	380.	0.05	0.15
45	Actual	338 380.	349 556.	1600.	410.963	0.0111766	0.10885

Θ_i	Var	$q''_{p,sd}$	$q''_{c,sd}$	$T_{c,sd}$	T_v^{out}	$\delta_{c,sd}$	δ_v
3	Guess	425 000	475 000	1580.	380.	0.05	0.15
68	Actual	338 380.	349 556.	1600.	410.963	0.0111766	0.10885

Θ_i	Var	$q''_{p,sd}$	$q''_{c,sd}$	$T_{c,sd}$	T_v^{out}	$\delta_{c,sd}$	δ_v
4	Guess	550 000	600 000	1580.	380.	0.05	0.15
90	Actual	338 380.	349 556.	1600.	410.963	0.0111766	0.10885

Table 3-4: Analytic and model comparison with error calculation

Var	$q''_{p,up}$	$q''_{p,dn}$	$q''_{c,up}$	$q''_{c,dn}$	T_p^{max}
Unit	W/m^2	W/m^2	W/m^2	W/m^2	K
Analytic	641 518.	345 907.	645 467.	356 848.	3118.59
Model	630 056.	338 380.	634 221.	349 556.	3115.86
%Error	1.787	2.176	1.742	2.044	0.087

Var	T_{up}	T_{dn}	$\delta_{c,up}$	$\delta_{c,dn}$	δ_{ves}
Unit	K	K	mm	mm	cm
Analytic	2065.62	411.039	3.94825	10.9409	10.6619
Model	2032.75	410.963	4.16477	11.1766	10.885
%Error	1.591	0.018	5.484	2.154	2.093

3.1.2 Reliability Verification

As previously mentioned, one method for testing code reliability and repeatability is to change a non-input parameter and observe the change if any in the result. Below are three plots showing a single run using parameters from the AP1000. In Chapter 4, this case

will be covered under Case H1 and is the base case for the calculations performed for that reactor type. The vertical axis shows heat flux to the coolant water from the exterior of the reactor vessel at various physical locations as denoted by the horizontal axis. The default number of angular partitions in the oxide pool is 24 while the default number of horizontal sections in the metallic layer is 16. For this comparison, cases of 24/16, 48/32, and 12/8 nodes are shown. By comparing Figure 3-2, Figure 3-3, and Figure 3-4, no difference is seen in the results and, thus, the code may be deemed reliable to reproduce results.

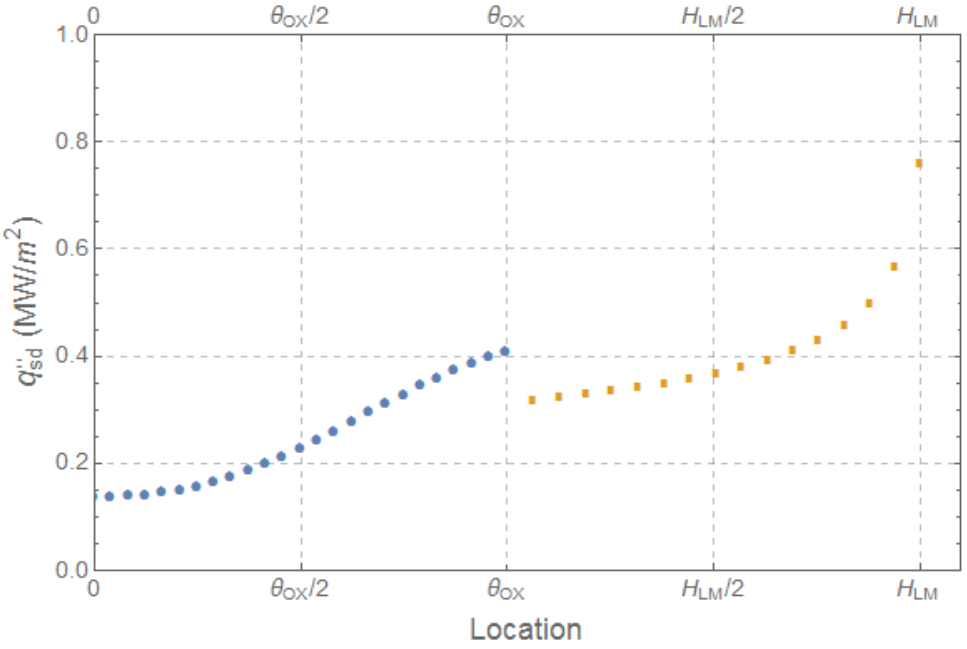

Figure 3-2: Case H1 with 24 oxide pool nodes and 16 metallic layer nodes

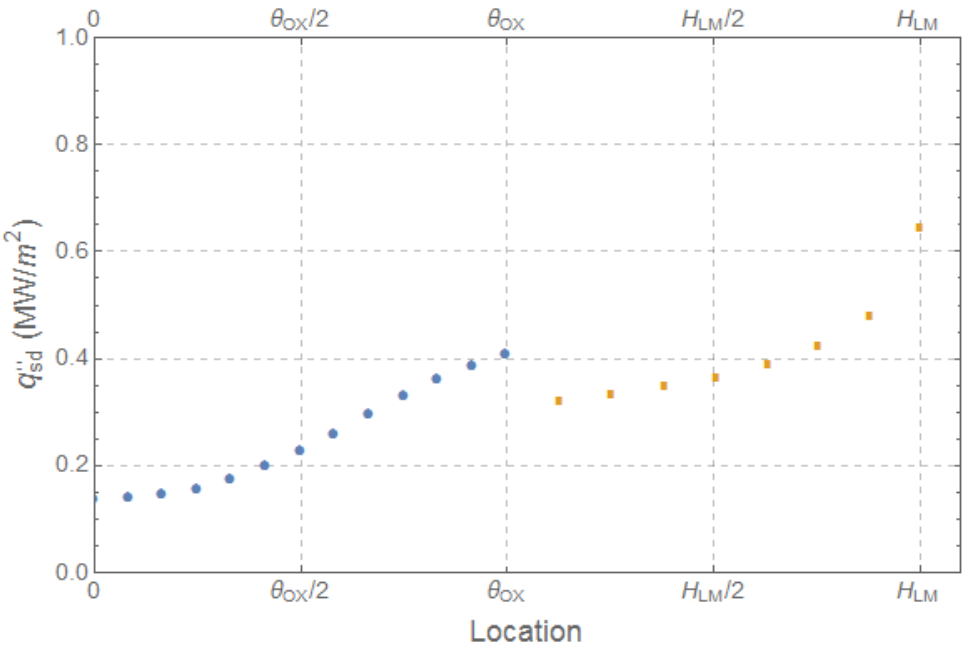

Figure 3-3: Case H1 with 12 oxide pool nodes and 8 metallic layer nodes

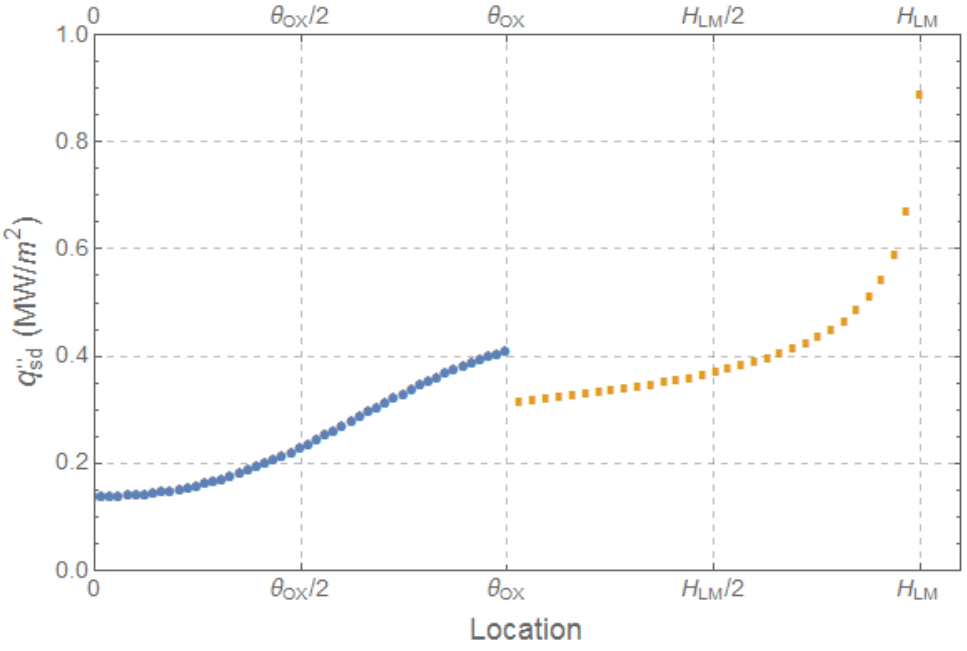

Figure 3-4: Case H1 with 48 oxide pool nodes and 32 metallic layer nodes

Finally, the conservation equations of the model may be verified to ensure that the equation set is properly applied to the input scenario. Table 3-2 shows a portion of the analytic one-loop model results presented in the previous section:

$A_{c,up} * q''_{c,up}$	$\Sigma [A_{c,sd} * q''_{c,sd}]$	Total	Q_{decay}
7.96985×10^6	8.78531×10^6	1.67552×10^7	1.67552×10^7

The first table value represents the product of the heat flux directed upward from the top of the crust and the top crust surface area. Second, the table shows the sum of all the side or downward facing heat fluxes multiplied by their respective surface areas. Since the assumption in the analytic solution was that there was no angular dependence on outward heat flux, this result is the same as multiplying that side heat flux value by the total downward surface area. Next, the table shows the sum of the first two entries and compares to the total decay heat in the system, shown in the final position. As there is no difference in the values, the model has successfully accounted for all heat produced in the system when determining the directional heat fluxes.

3.2 Model Comparison with IVRAM

Below are comparisons with the two layer model developed at NCSU and the results from the IVRAM [7] model using ERI input deck values and AP1000 parameters. The results in Esmaili et al were produced using average parameter values resulting in average volumetric decay heat values in the oxide pool layer of 2.1 MW/m^3 with a peak value of nearly 3.0 MW/m^3. In the configuration used for the below plots, the Esmaili team assumed zero heat generation in the light metal layer and, thus, the NCSU model was adapted to these values to compensate. In the plots generated at NCSU, lines representing the average 2.1 and peak 3.0 MW per cubic meter generation have been shown.

Figure 3-5 shows the comparison between the NCSU and IVRAM heat flux to water results. The NCSU model shows excellent agreement with the IVRAM results, containing most of the data within the bounds of the average and maximum heat flux trials. Sources for the small deviations certainly include the use of different correlations. Both the IVRAM model and the NCSU model utilized the Mayinger [22] correlation for sideways facing heat flux from the oxide pool and the Kulacki-Emara [23] correlation for upward facing heat

flux from the same layer. However, the IVRAM model used the Churchill-Chu [24] correlation in the metallic layer while the NCSU model used the adapted Chawla-Chan model. This level of agreement may be seen mirrored in Figure 3-7 and Figure 3-8 in the crust and vessel thickness results, respectively. At lower angular positions, the IVRAM results stay between the NCSU bounds which have a higher spread in this region. At higher angular positions where the heat flux resides within NCSU bounds, the results for crust thickness show greater agreement. Across all angular positions, the IVRAM vessel thickness results track well with the NCSU upper limit case.

The most varied results may be seen in Figure 3-6 which shows the CHF margin and crust thickness results from both models. The reason the CHF models differ is due to the scalar multiplier for the ULPU configuration III data [11] used by both models. The IVRAM model used a 1.44x multiplier which demonstrated good agreement with ULPU configuration IV and V data until about a 70° position on the lower head, at which point the model over-predicted the CHF levels. The NCSU model uses a more conservative 1.30x multiplier which ensures no over-prediction for CHF at any angular position but results in lower CHF predictions at lower angular positions. Thus, the IVRAM results agree with the NCSU CHF results at lower angular positions before residing between the limits of the NCSU model at higher positions.

Overall, the results produced by the NCSU model show agreement in both trend and magnitude to the counterparts from the IVRAM study. This helps to accomplish two criteria for the model's development that a) the model works as intended to characterize heat transfer in the lower head and that b) the results are concurrent with previous models such as FIBS/VESPA/IVRAM.

3.2.1 Heat Flux and CHF Limit

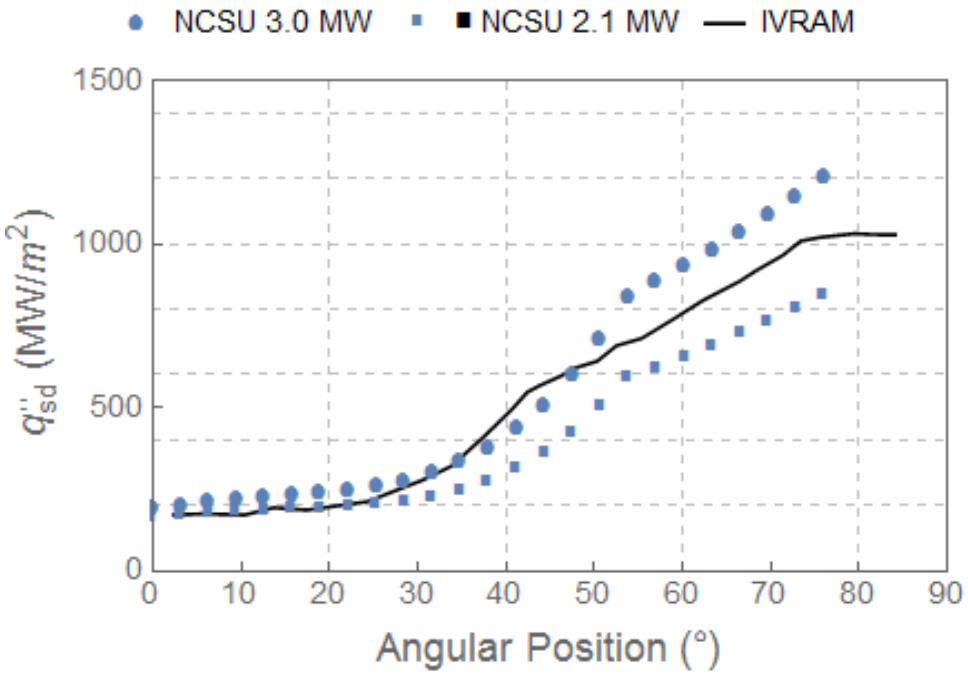

Figure 3-5: Comparison of IVRAM and NCSU heat flux to water results

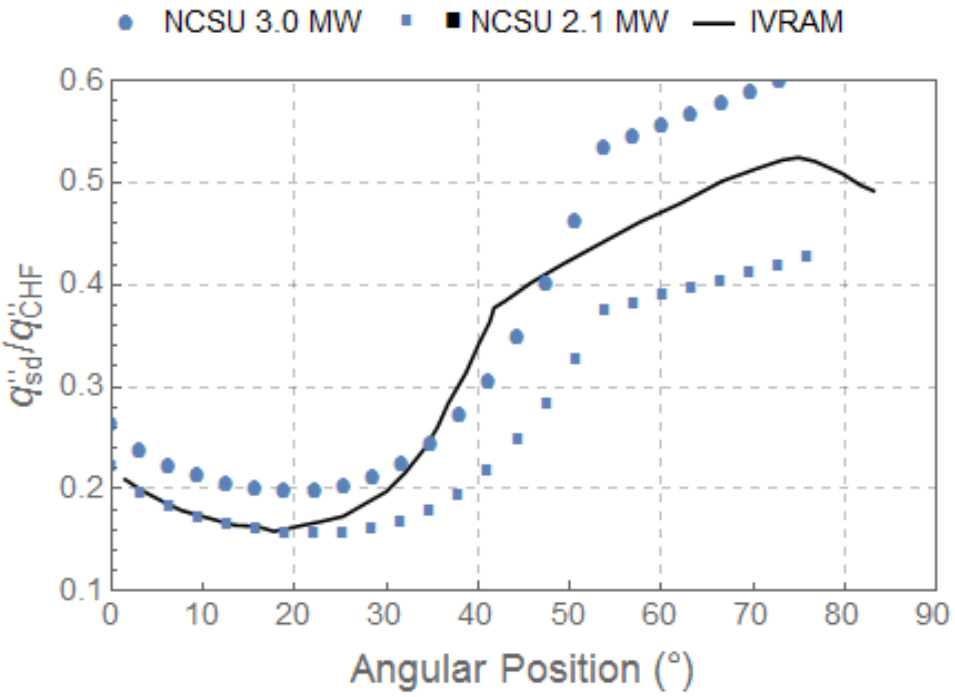

Figure 3-6: Comparison of IVRAM and NCSU CHF margin results

3.2.2 Crust and Vessel Thickness

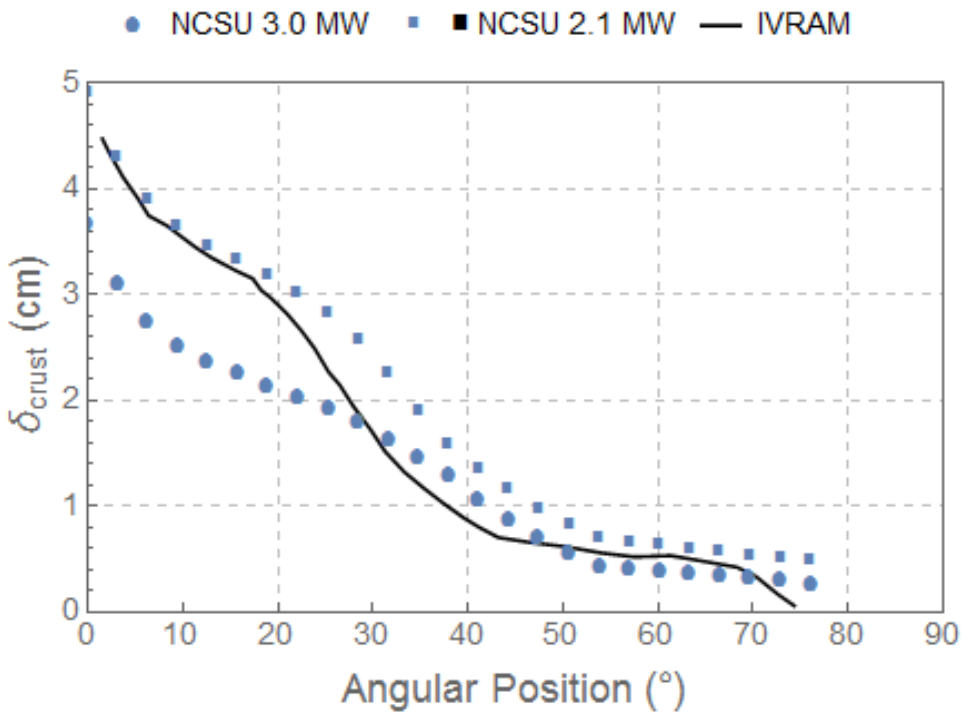

Figure 3-7: Comparison of IVRAM and NCSU crust thickness results

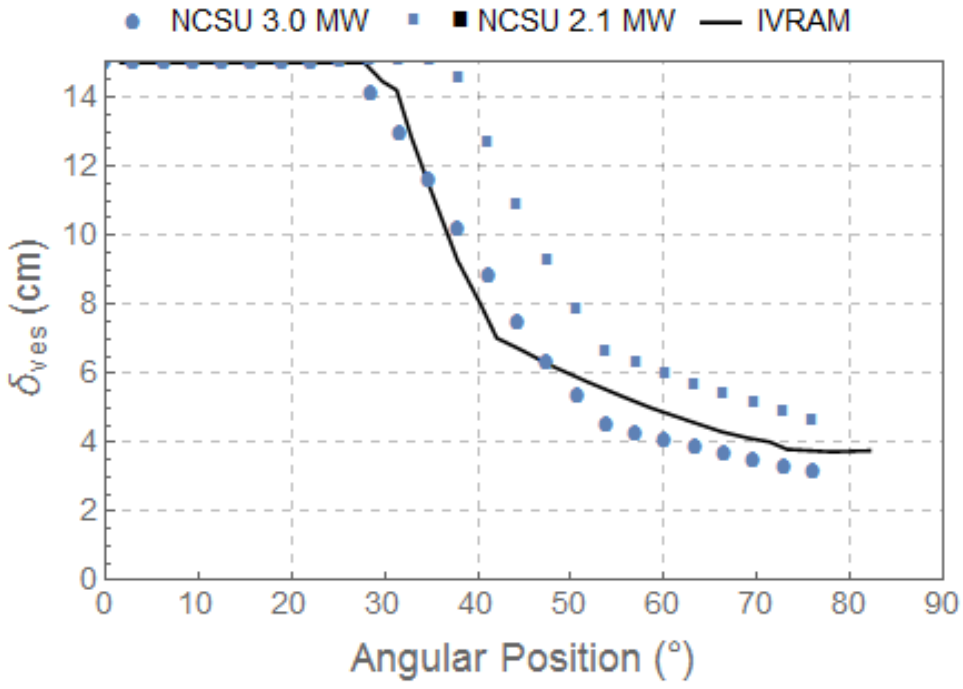

Figure 3-8: Comparison of IVRAM and NCSU vessel thickness results

4 REACTOR APPLICATION

This section contains results from primary applications for the developed model. The three main result types generated were those for the AP1000 geometry, those for SMR type reactors, and quasi-transient results including a correlation sensitivity study. The AP1000 results were used for comparison with previous models by measuring heat flux, thermal margin, and crust and vessel thickness. Multiple cases demonstrated the breadth of capability for the developed model and showcased different phenomena and trends in the heat transfer scheme. The SMR adaptations primarily utilize an elliptical lower head geometry and offer a look into thermal margin capabilities for typical compact reactor designs. The results for these reactors showcase the large margin present in the low-power passive designs and further encourage SMR development. Finally, the quasi-transient results look at a series of steady state results for the AP1000 while adding metallic mass over time. This type of result shows a departure from previous models and sets up future work into fully transient realization. Additionally, the quasi-transient framework was used to compare different Nusselt number correlations in the oxide pool under otherwise identical circumstances. This provided a look at the model's sensitivity to the oxide pool correlations, offered data to support uncertainty quantification, and showcased the ability for the model to duplicate this type of analysis for other parameters.

4.1 AP1000 Results

4.1.1 Overview

The following results detail the cases run for AP1000 geometry based from the ERI input deck used in *Esmaili et al* [7]. The runs varied in decay heat, core mass loading for the two layers, and the geometry of the lower head. Table 4-1 below outlines the different runs using multipliers of the base values as an indicator of the level used. Results of selected cases will be shown in subsequent subsections. The results show the heat transfer across both layers for the hemispherical geometry, a separate view of the thermal margin to CHF for the same geometry, the vessel thickness across the two layers for the given scenario, and finally a comparison of thermal margin for the hemispherical case and the same scenario with elliptical geometry. Note that in many of the repesented cases, the elliptical geometry offers a greater margin than the hemispherical version. Overall, these

parametric results show agreement between this model and previous work such as IVRAM. This fufills one characteristic for the model that the calculations obtained agree with those from the FIBS/VESPA/IVRAM models.

Table 4-1: Base values and case parameter summary for AP1000 results

Base Values – r_{LP} = 2m									
Quantity		Decay Heat		OP Mass		LM Mass		Ellipse Ratio	
Unit		MW		kg*1000		kg*1000		--	
Value		14.625		88.783		79.595		1	
Hemispherical Geometry Cases - Base Multipliers					**Elliptical Geometry Cases - Base Multipliers**				
Case	Decay Heat	OP Mass	LM Mass	Ellipse Ratio	Case	Decay Heat	OP Mass	LM Mass	Ellipse Ratio
H-1	1.0	1.0	1.0	1	E-1	1.0	1.0	1.0	3.0
H-2	2.0	1.0	1.0	1	E-2	2.0	1.0	1.0	3.0
H-3	1.5	1.0	1.0	1	E-3	1.5	1.0	1.0	3.0
H-4	1.0	1.0	2.0	1	E-4	1.0	1.0	2.0	3.0
H-5	2.0	1.0	2.0	1	E-5	2.0	1.0	2.0	3.0
H-6	2.5	1.0	2.0	1	E-6	2.5	1.0	2.0	3.0
H-7	1.0	1.0	0.1	1	E-7	1.0	1.0	0.1	3.0
H-8	2.0	1.0	0.1	1	E-8	2.0	1.0	0.1	3.0

Table 4-1 summarizes the parameters for the completed runs for the AP1000 style. The base values correspond to those found in the input deck supplied by ERI (Appendix B and used by Esmaili et al. in the IVRAM trials. The decay heat of 14.6 MW is indicative of a decay heat two days following a shutdown from full power. This timing of 48 hours is an adequate value for considering the type of fully formed corium pool assumed in this heat transfer model. Throughout the cases, multipliers of the decay heat simulate earlier timeframes for analysis of a more rapid accident progression. In general the light metal layer mass has a profound impact on the coolability of the vessel. Trials with increased multipliers for the LM mass show far greater thermal margins to failure than those with less. This trend is accentuated in the final two cases where the drastically reduced light metal layer simulates the focusing effect phenomena and results in drastically high heat fluxes in excess of CHF.

4.1.2 Selected Cases - Case H1 and E1 [Base Case]

Table 4-2: Case H1 and E1 Parameters

Decay Heat (MW)	Oxide Pool Mass (kg)	Light Metal Mass (kg)
14.625 (1.0x)	88780 (1.0x)	79600 (1.0x)

This is the base case for the runs and calculations. The first series denotes data points taken from the oxide pool section while the second series denotes points from the light metal layer. The sets using (x) plot markers represent the same case but with an ellipse ratio of 3.0. For this case at nominal values for decay heat and core loading, the system does not reach critical heat flux (CHF) on the exterior surface. Thus, the accepted criteria for vessel failure is not reached in this steady state example.

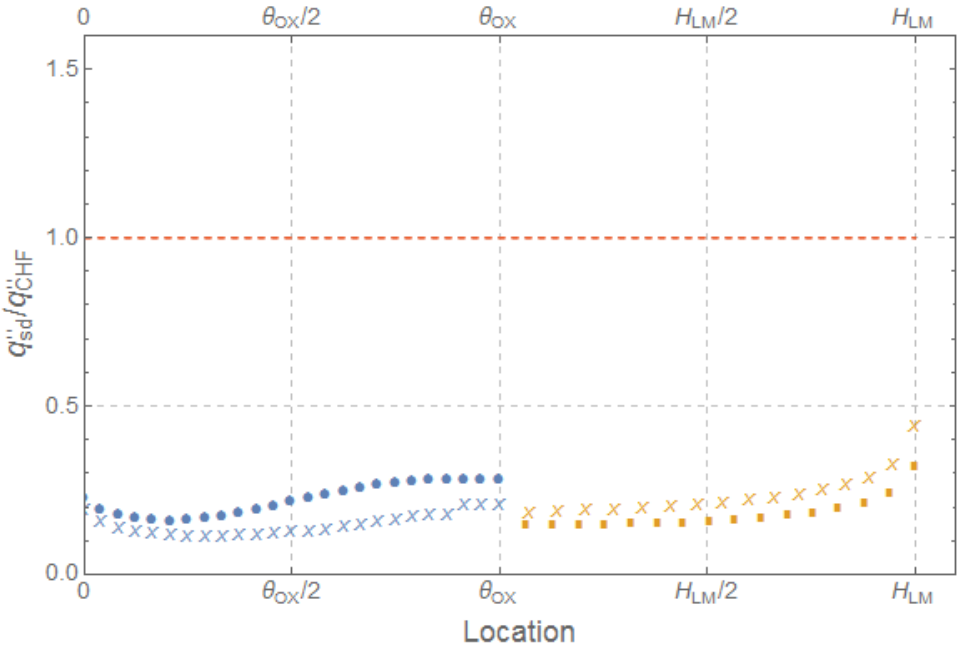

Figure 4-1: Results for cases H1 and E1 thermal margin to CHF

● – hemispherical data series x – elliptical data series

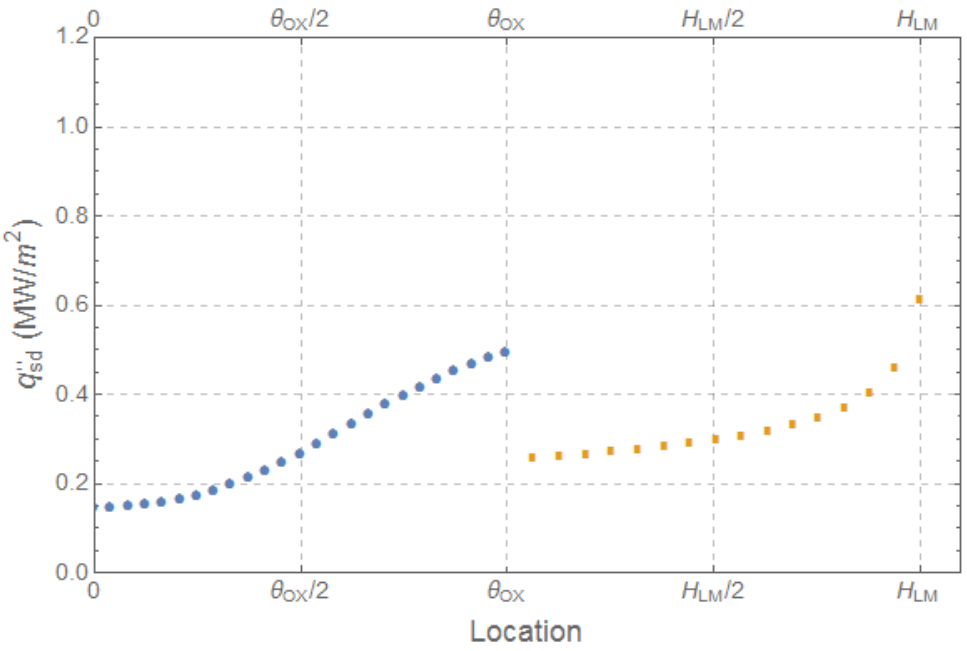

Figure 4-2: Results of case H1 heat flux to coolant by vessel position

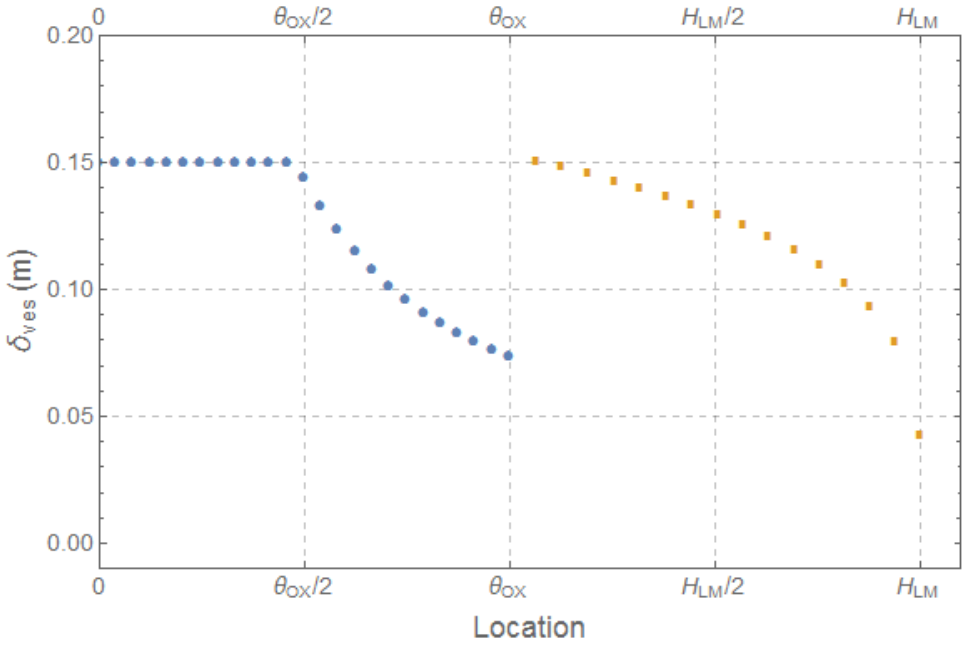

Figure 4-3: Results for case H1 vessel thickness by vessel position

4.1.3 Selected Cases - Case H2 and E2 [Doubled Decay Heat]

Table 4-3: Case H2 and E2 Parameters

Decay Heat (MW)	**Oxide Pool Mass (kg)**	**Light Metal Mass (kg)**
29.25 (2.0x)	88780 (1.0x)	79600 (1.0x)

This case demonstrates the effect of doubling the nominal decay heat expected from the base run. Here the upper nodes in the metallic layer exceed CHF levels and, thus, vessel failure is expected in this scenario. The effects of the COPO correlation are more readily visible in this example. The three oxide pool data points at the end of the elliptical series demonstrate the shift from the "downward" facing COPO heat flux to the "sideways" oriented heat flux correlation.

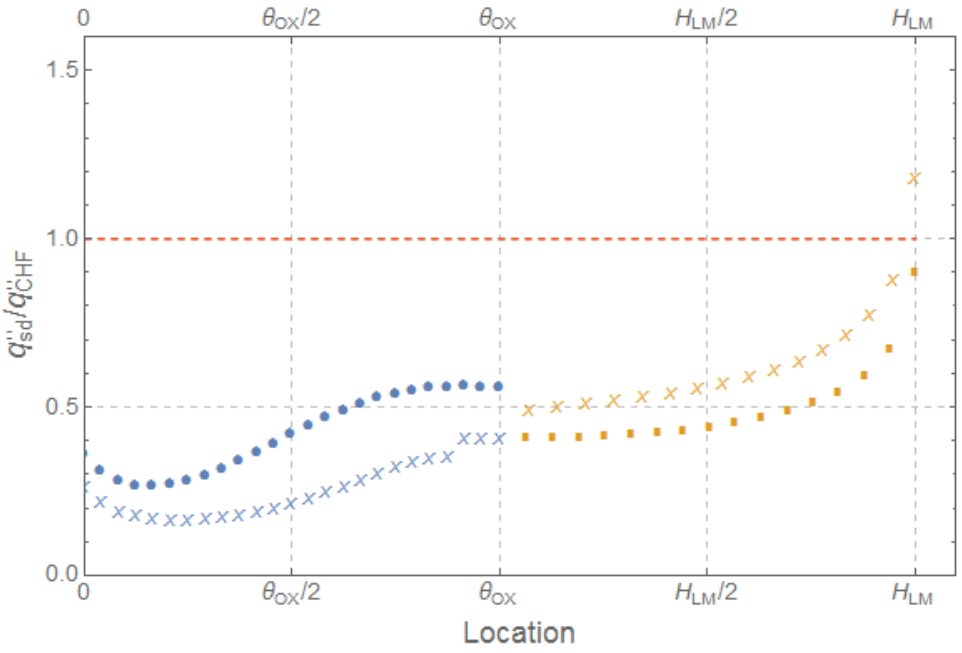

Figure 4-4: Results for cases H2 and E2 thermal margin to CHF

● – hemispherical data series x – elliptical data series

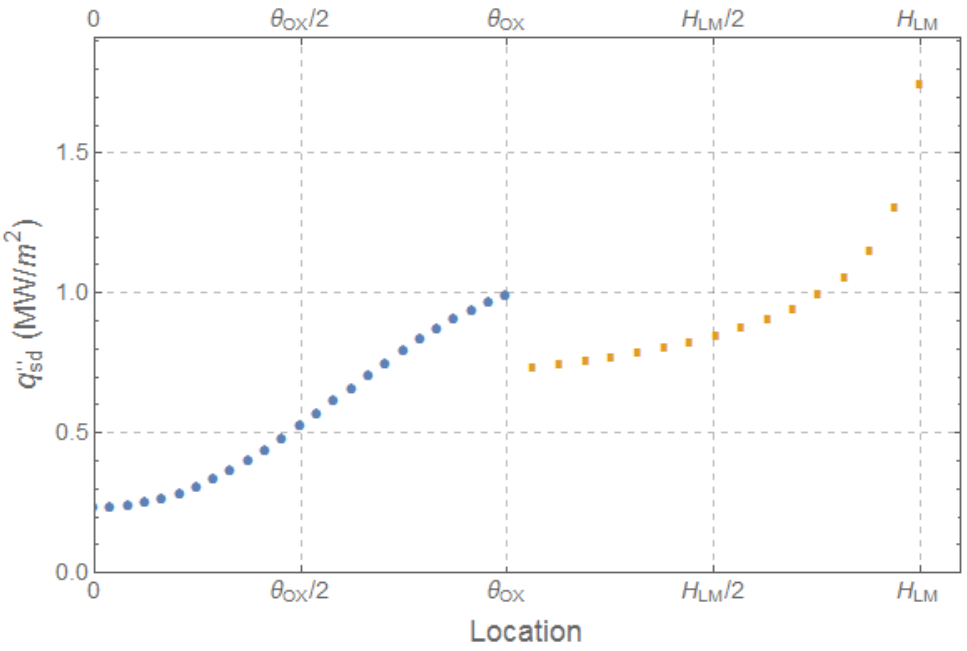

Figure 4-5: Results for case H2 heat flux to coolant by vessel position

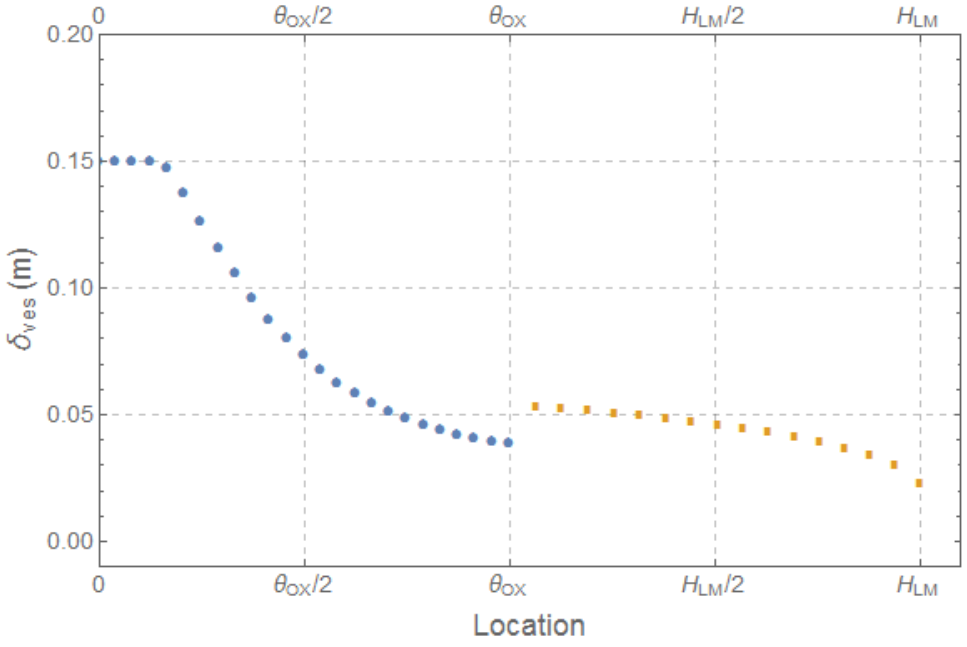

Figure 4-6: Results of case H2 vessel thickness by vessel position

4.1.4 Selected Cases - Case H6 and E6 [Double Metallic Layer Failure]

Table 4-4: Case H6 and E6 Parameters

Decay Heat (MW)	**Oxide Pool Mass (kg)**	**Light Metal Mass (kg)**
36.56 (2.5x)	88780 (1.0x)	159200 (2.0x)

This particular case demonstrates the effect of a massive metallic layer as compared to the base case. Comparing this case to case H2, the CHF levels are not exceeded in the geometry despite an even higher decay heat. This is due to the metallic layer's increased heat dispersion due to its larger volume. Another conclusion from this case is that the gap between the thermal margin for the oxide pool and metallic layer has lessened. By increasing the metallic layer mass further still, the oxide pool would become the layer in danger of exceeding CHF, but due to the disparity between layer masses necessary, this scenario is unlikely.

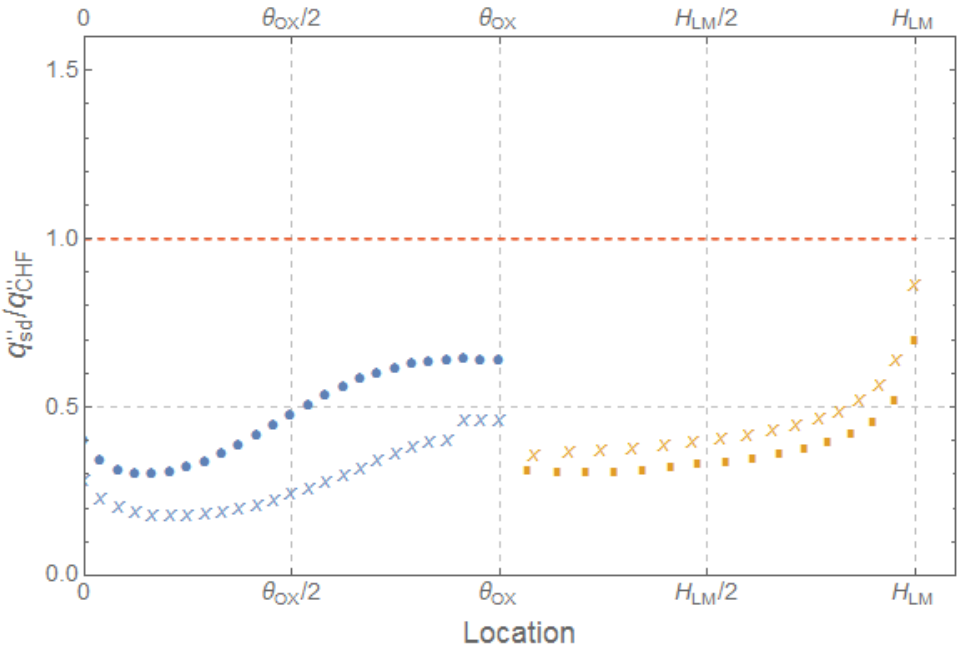

Figure 4-7: Results for cases H6 and E6 thermal margin to CHF

● – hemispherical data series x – elliptical data series

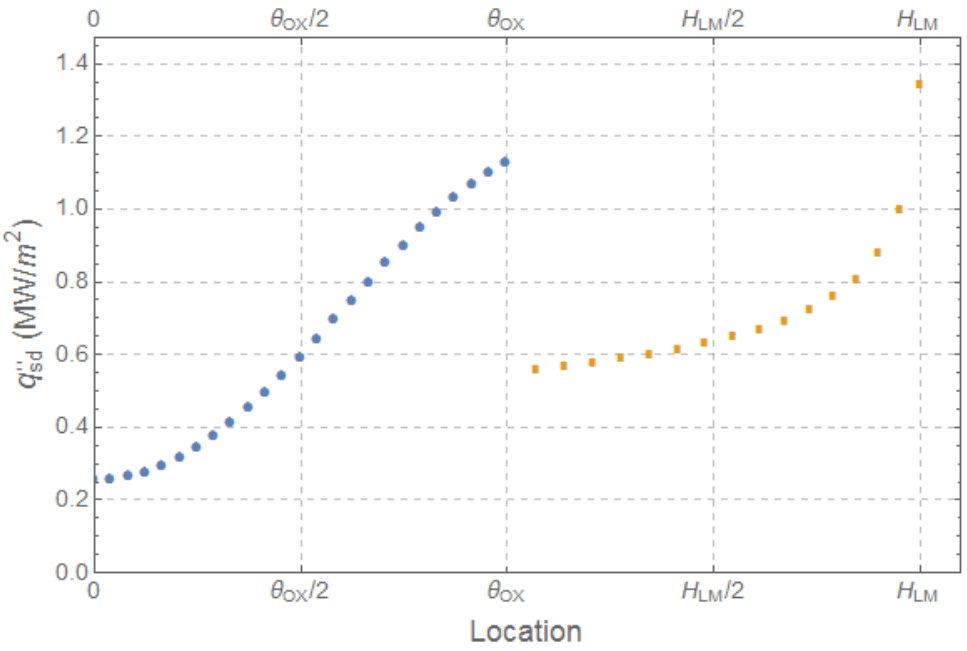

Figure 4-8: Results for case H6 heat flux to coolant by vessel position

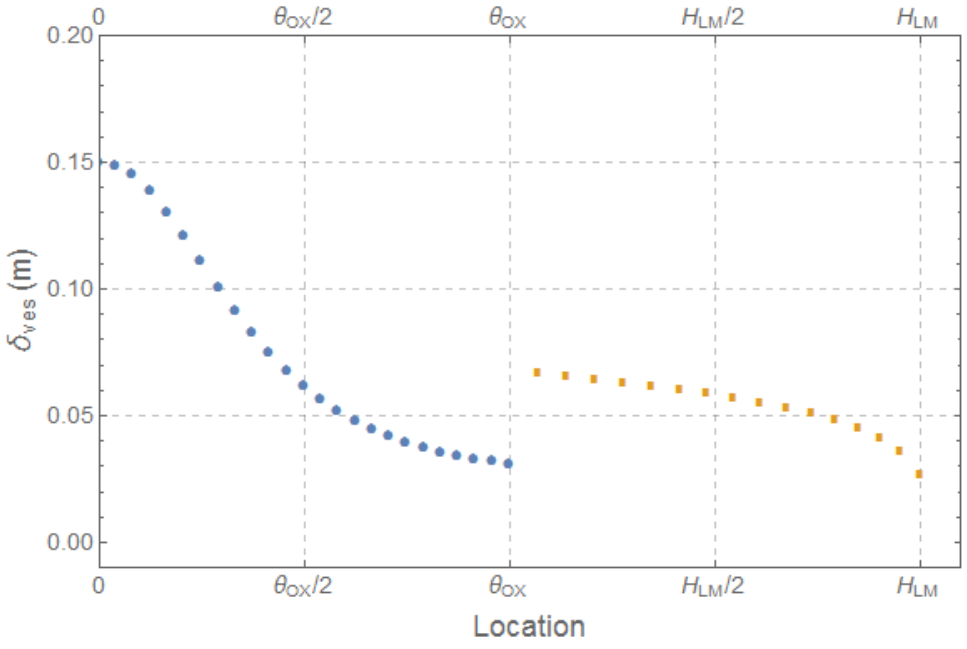

Figure 4-9: Results of case H6 vessel thickness by vessel position

4.1.5 Selected Cases - Case H7 and E7 [Focusing Effect]

Table 4-5: Case H7 and E7 Parameters

Decay Heat (MW)	**Oxide Pool Mass (kg)**	**Light Metal Mass (kg)**
14.625 (1.0x)	88780 (1.0x)	7960 (0.1x)

Finally, this case demonstrates the focusing effect resulting from a thin metallic layer. Under this situation, the thin metallic layer can act as a reflector for the heat traveling from the top of the oxide pool. This reflection combined with the small surface area for the metallic layer to distribute heat leads to a rapid reduction in the vessel wall as heat fluxes greatly increase. Here, CHF has been exceeded entirely in the metallic layer indicating a strong probability for failure of the lower head.

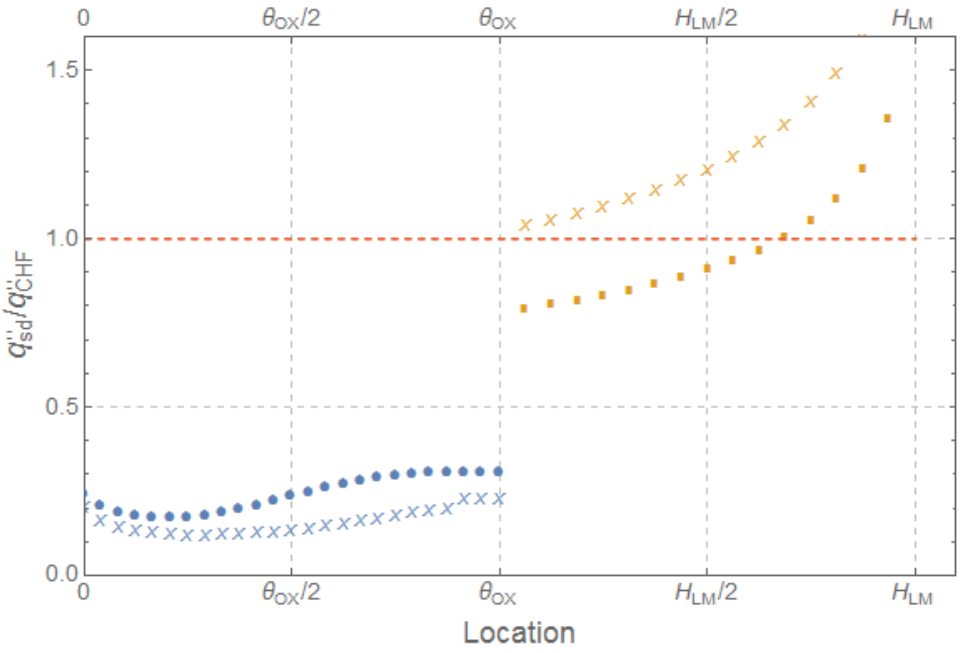

Figure 4-10: Results for cases H7 and E7 thermal margin to CHF

● – hemispherical data series x – elliptical data series

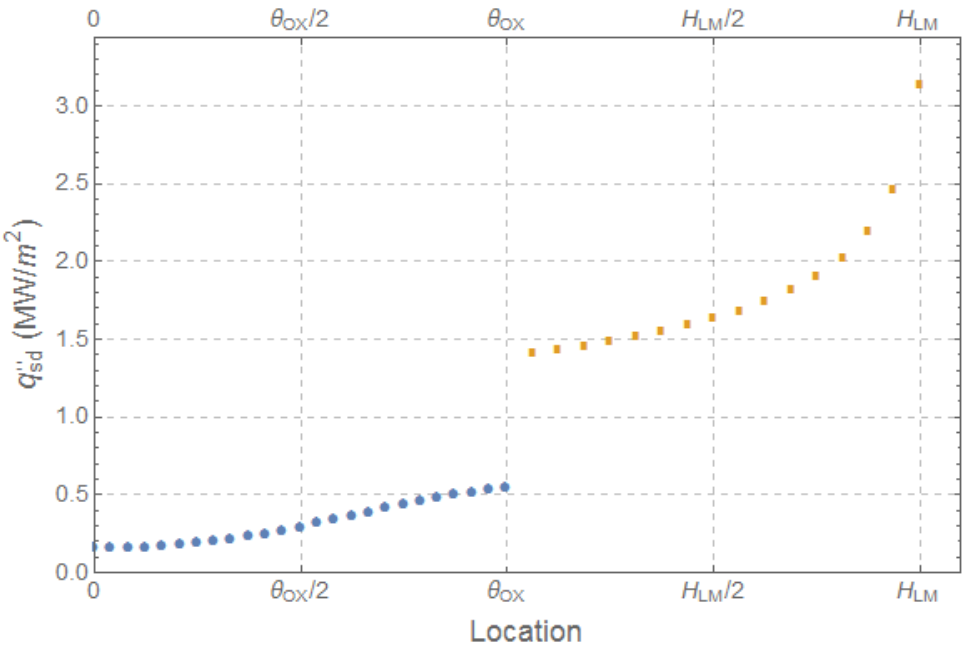

Figure 4-11: Results for case H7 heat flux to coolant by vessel position

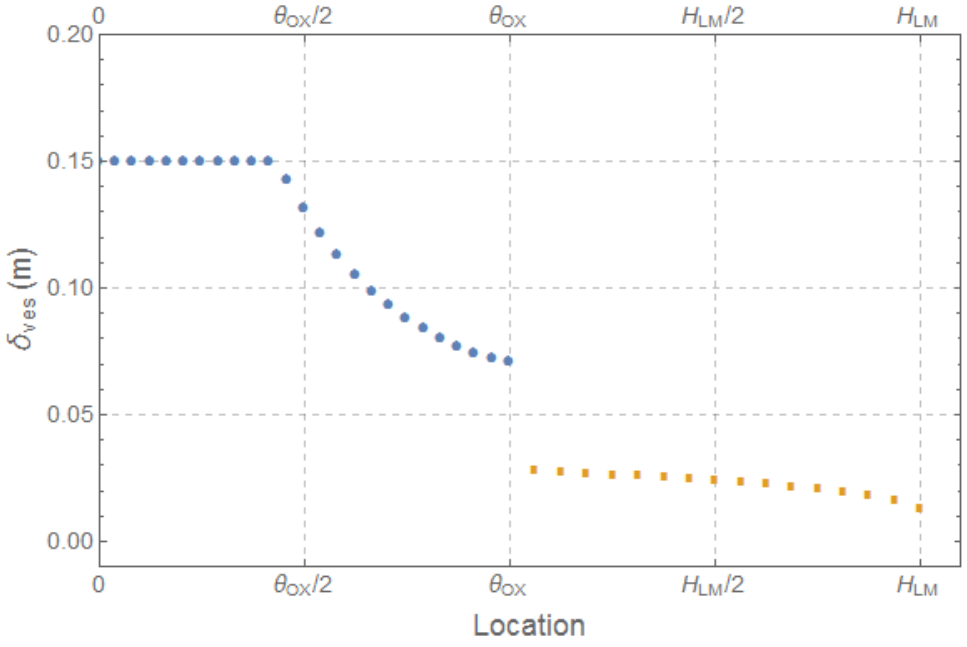

Figure 4-12: Results for case H7 vessel thickness by vessel position

4.2 SMR Results

Public data for the mPower SMR was utilized for determining the characteristics for the typical SMR reactor [6]. The thermal power rating of the plant was lowered to 530 MWt and the core loading was dropped to approximately 2.5 m^3 per layer. This is in contrast to the 10 m^3 per layer found in the AP1000 cases. Figure 4-13 shows the decay heat required to force a failure in the vessel for hemispherical and elliptical geometries.

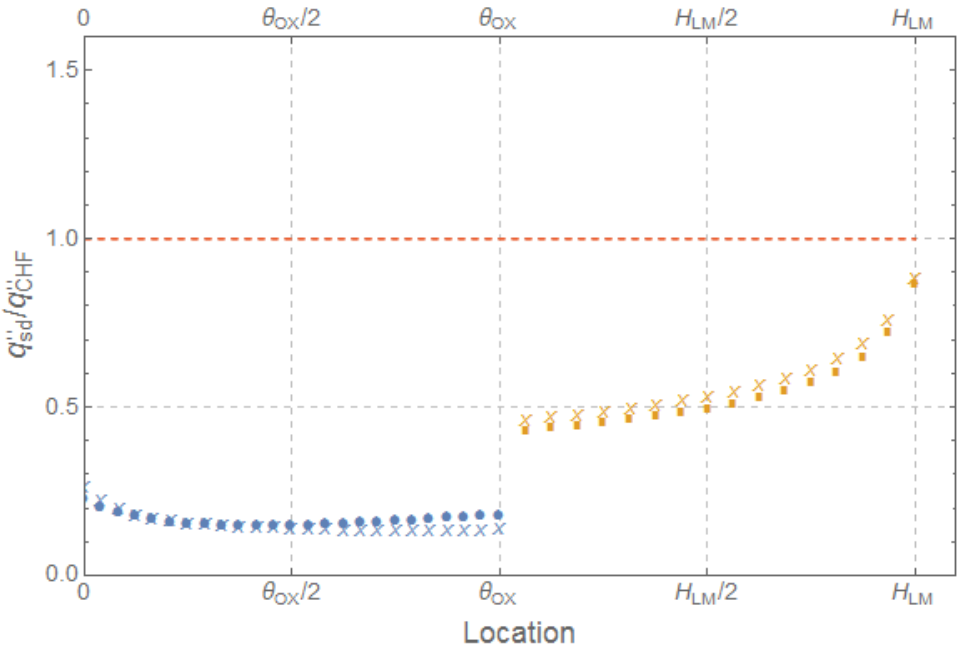

Figure 4-13: Comparison of SMR geometries and respective thermal margins

● – hemispherical data series x – elliptical data series

In the figure, the series denoted by the circle markers represents a hemispherical SMR geometry with a total decay heating of 4.14 MW which is 1.5x the nominal 2.76 MW experienced in this setting at a time of one day. Comparatively, the series denoted by the cross markers represents an identical reactor utilizing an elliptical lower head geometry with an axis ratio of 3.0. For the elliptical series, the total decay heat is 6.63 MW which is 2.4 times nominal. In addition, both situations were performed using a 0.1x multiplier for

the light metal layer, recreating the focusing effect seen earlier in the AP1000 data. Table 4-6 summarizes these run parameters for the SMR trials.

Table 4-6: Run parameters for SMR geometry comparison study

Geometry	Decay Heat (MW)	Oxide Pool Mass (kg)	Light Metal Mass (kg)
Hemispherical	4.14 (1.5x)	20500 (1.0x)	1725 (0.1x)
Elliptical	6.63 (2.4x)	20500 (1.0x)	1725 (0.1x)

In conclusion, the SMR reactor has high threshold for decay heating in order to violate CHF values. This has been demonstrated in a focusing effect scenario assuming both an elliptical and a hemispherical geometry for the lower head. Overall, the results showcase a strong argument for the use of the IVR strategy for SMR severe accident management. In addition, the comparison of lower head designs reinforces the trend seen previously that an elliptical geometry can offer equal or higher thermal margin than a hemispherical version.

4.3 Quasi-Transient Results

In order to improve upon previous models, one method employed by this program is to perform a quasi-transient analysis. Quasi-transient runs involve taking steady state data at different timesteps while changing parameters of the runs at various timesteps. In these cases, the masses of the corium layers were increased every hour while a steady state data point was collected every twenty minutes. For each run, the maximum CHF ratio was collected, providing a transient look at the thermal margin for these conditions taking into account decreasing decay heat and increasing layer mass. This shows the ability for the model to track failure conditions through time and the framework for a full transient analysis.

The first case run (Case QT-1) is summarized by Table 4-7 and Figure 4-14. In this example, the analysis began at t = 1 day with a partially melted core represented by a 50% reduction in metallic mass but 100% of the available oxide mass. The decay heat is assumed to be proportional to the mass of the molten pool by the following equation:

$$\dot{Q}_d = \left(0.9\frac{m_{OX,pool}}{m_{OX,core}} + 0.1\frac{m_{LM,pool}}{m_{LM,core}}\right)\dot{Q}_{d,0}$$

This expression reflects the assumption made in the model that 90% of the decay heating is found in the oxide pool and 10% is due to materials in the metallic layer. With timesteps of 20 minutes, the run increases the mass of the metallic layer by roughly 2% of the full core amount every hour. Combined with the declining decay heat over time this results in a steadily declining CHF ratio over time. This trial run was successful in showcasing the ability for the model to develop this type of analysis but is unrealistic by not increasing both material compositions and assuming one material as fully developed with a fraction of the other.

The second case analyzed (Case QT-2) is summarized by Table 4-8 and Figure 4-15. In this case, a 50% molten core was assumed to be already in place in the lower head. Every hour, an addition of 5% total oxide mass and 2% of the total light metal layer mass is added. These additions are, as before, assumed to be fully developed and as having no impact on the temperature profile of the pool.

The combination of these effects yields the results shown in Figure 4-15. Early in the progression, the thermal margin shrinks as more mass is added and the decay heating is increased in the system. Additionally, the decay heat increases at a rate greater than the addition of metallic layer mass, causing an additional focusing effect threat before the metallic layer develops to a point to adequately distribute the heat. Over time, however, the mass additions stop as all the material relocates and the decay heating continues to diminish. This leads to a plateau and then increase of thermal margin for the remainder of the simulation.

The previous two simulations began at a time 24 hours post-accident or post-reactor trip. These levels aligned with previous result types such as the parametric results from the AP1000 geometry. Accident progression, however, can begin far sooner and it is worthwhile to look at the effects of core formation at a sooner time. Case QT-3 begins with the same 50/50 partially formed pool as in case QT-2. This time, however, the simulation begins 6 hours following the reactor trip. The same mass additions of 5% and 2% for the oxide and metallic layers, respectively, are made hourly and the results for the simulation

are shown by Figure 4-16. The interesting result from this simulation is the roughly constant value of 0.75 for the maximum ratio to CHF experienced up until t = 16 hours. With these starting conditions, the mass additions are a nearly even offset for the declining decay heating, which provides the stagnant values at steady state. Case QT-4 tests the trend set by QT-3 by increasing the rate of addition for the oxide material to 10% per addition. The expected result would be that the total decay heat increases faster than the decline and the thermal margin shrinks as opposed to holding steady as in QT-3. Indeed, Figure 4-17 shows the results of case QT-4 and the increased rate of oxide mass addition drives the thermal margin down and actually exceeds CHF values before declining once the oxide mass is fully incorporated.

As opposed to previous results utilizing the ACOPO correlations, these simulations were performed using the INEEL best fit estimation (see Table 4-11) for its conservative values. Using this approach, accident scenarios may be pre-conditioned and various postulated progression paths may be tested and compared.

4.3.1 Case QT-1 [Basic Metallic Mass Addition]

Table 4-7: Quasi-transient parameter summary for case QT-1

Quantity	**OX Mass, Initial**		**LM Mass, Initial**		**OX Mass, Addition**		**LM Mass, Addition**	
Unit	kg	%	kg	%	kg	%	kg	%
Value	88800	100.0	39800	50.0	0	0	1600	2.0
Quantity	**Time, Initial**		**Time, Step**		**Time, Final**		**Time, Mass Add**	
Unit	hr		min		hr		hr	
Value	24		20		48		1	

In this case metallic mass is added periodically to a fully developed oxide pool and a partially developed metallic layer. The thermal margin increases as expected due to the increased metallic mass and decreasing decay heating.

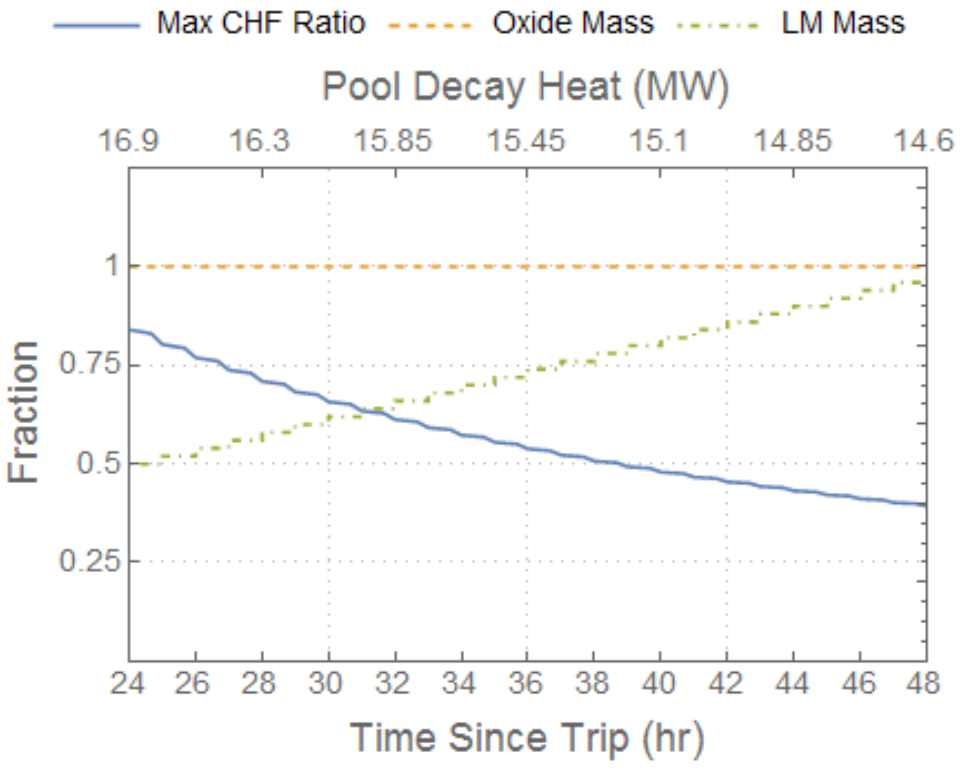

Figure 4-14: Quasi-transient analysis of CHF ratio and layer masses for case QT-1

4.3.2 Case QT-2 [Varied Mass Addition to Both Layers]

Table 4-8: Quasi-transient parameter summary for case QT-2

Quantity	**OX Mass, Initial**		**LM Mass, Initial**		**OX Mass, Addition**		**LM Mass, Addition**	
Unit	kg	%	kg	%	kg	%	kg	%
Value	44500	50.0	39800	50.0	4400	5	1600	2.0
Quantity	**Time, Initial**		**Time, Step**		**Time, Final**		**Time, Mass Add**	
Unit	hr		min		hr		hr	
Value	24		20		48		1	

In this case oxide and metallic mass is added periodically to a partially developed corium pool. The thermal margin decreases as a result of the additional decay heat due to the oxide mass but then decreases as expected due to the increased metallic mass and decreasing decay heating once the oxide layer is fully incorporated.

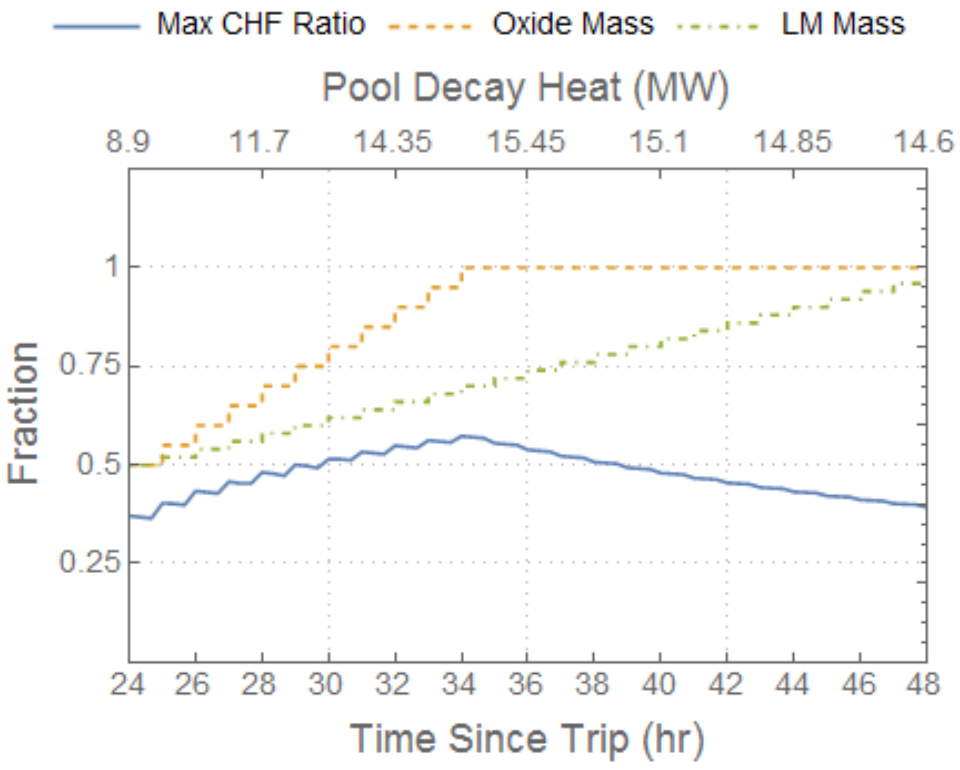

Figure 4-15: Quasi-transient analysis of CHF ratio and layer masses for case QT-2

4.3.3 Case QT-3 [Six Hour Post-Accident Timing]

Table 4-9: Quasi-transient parameter summary for case QT-3

Quantity	**OX Mass, Initial**		**LM Mass, Initial**		**OX Mass, Addition**		**LM Mass, Addition**	
Unit	kg	%	kg	%	kg	%	kg	%
Value	44500	50.0	39800	50.0	4400	5	1600	2.0
Quantity	**Time, Initial**		**Time, Step**		**Time, Final**		**Time, Mass Add**	
Unit	hr		min		hr		hr	
Value	6		20		30		1	

This case mimics the previous trial but at an earlier onset time and, thus, a higher initial decay heat. The oxide mass increases in this example counteract the decreasing decay heat and increasing metallic mass for a time and the system maintains a semi-constant thermal margin. The thermal margin increases once the oxide pool is fully formed.

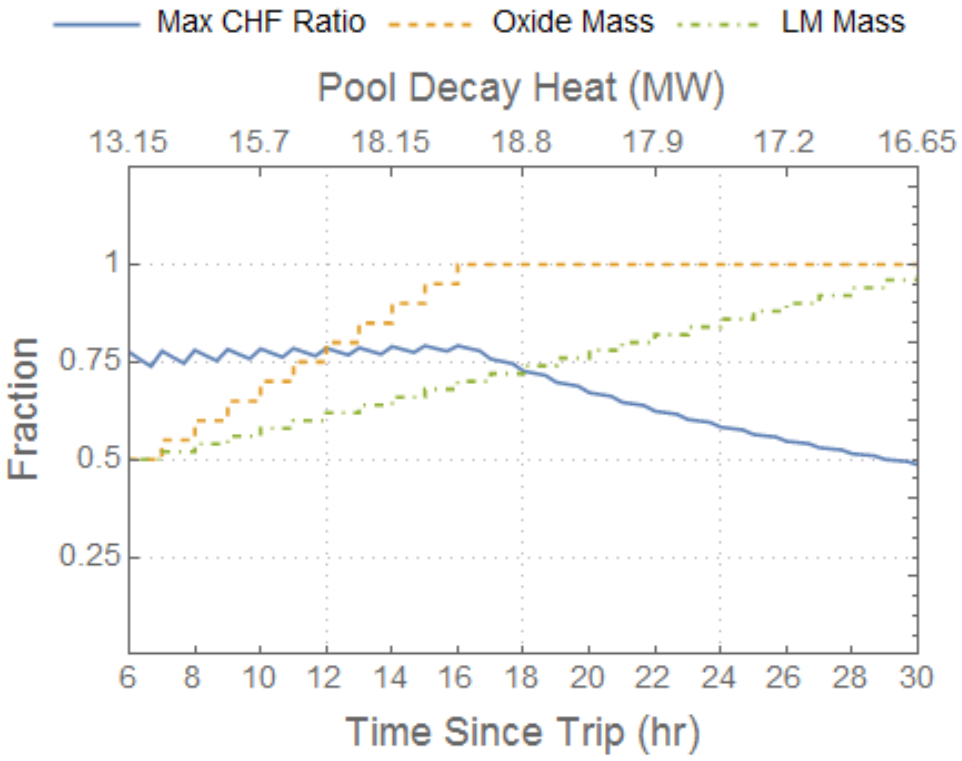

Figure 4-16: Quasi-transient analysis of CHF ratio and layer masses for case QT-3

4.3.4 Case QT-4 [Six Hour Timing, Faster Mass Addition]

Table 4-10: Quasi-transient parameter summary for case QT-4

Quantity	**OX Mass, Initial**		**LM Mass, Initial**		**OX Mass, Addition**		**LM Mass, Addition**	
Unit	kg	%	kg	%	kg	%	kg	%
Value	44500	50.0	39800	50.0	8800	10	1600	2.0
Quantity	**Time, Initial**		**Time, Step**		**Time, Final**		**Time, Mass Add**	
Unit	hr		min		hr		hr	
Value	6		20		30		1	

By increasing the rate of oxide mass addition from the previous case, it is possible to drive the thermal margin to zero and violate the CHF limit of the system.

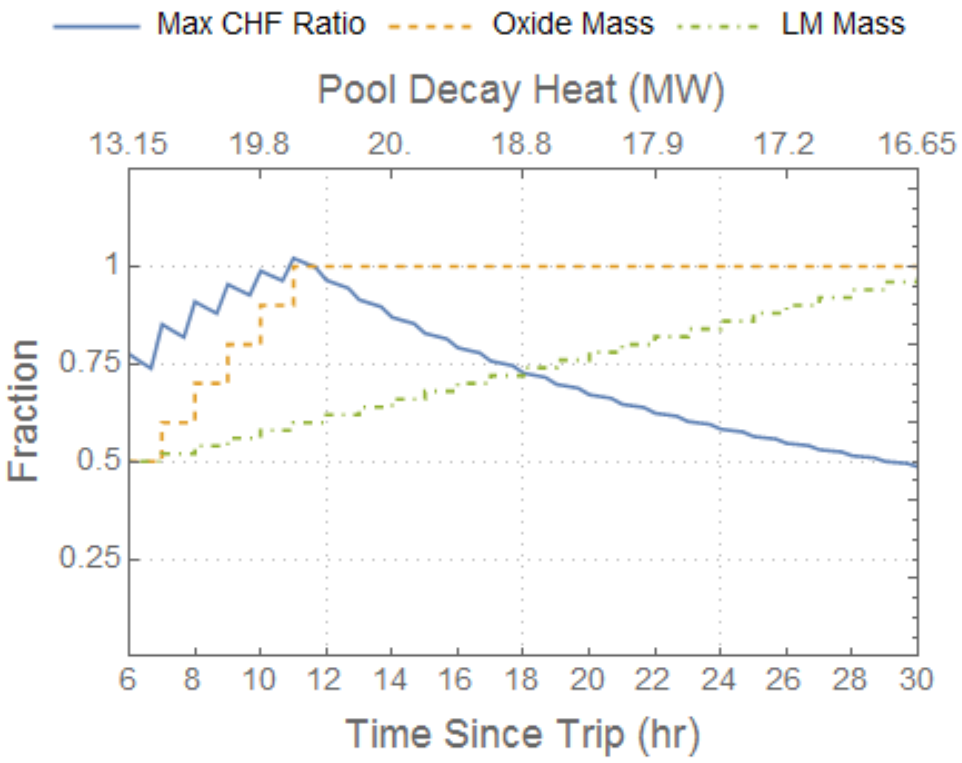

Figure 4-17: Quasi-transient analysis of CHF ratio and layer masses for case QT-4

4.4 Correlation Comparison

The final type of application shown is a comparison of various Nusselt number correlations in the oxide pool and the effect of the correlation on the overall results. For this example, the model simulated a quasi-transient run similar to Section 4.3. Beginning at a time of 6 hours, the pool was assumed to already be fully formed with 100% of available oxide and metallic mass incorporated and no further added mass. Thus, this example represents a progression of steady state values tracking only the decline in decay heat over time. Outlined in Table 4-11 are the five main correlation sets used: ACOPO [14] [25], the INEEL digitized "best-fit" estimate for the ACOPO data [9], mini-ACOPO [8] [20], Kulacki-Emara [23] and Mayinger [22], and an early version of the ACOPO correlation which does not rely on the fluid Prandtl number discussed by Theofanous et al [14].

Table 4-11: Correlations used in comparison study

Correlation Set	Direction	Correlation & Equation	Ra Applicability
ACOPO [14] [25]	Upward	$Nu = 0.3 * Ra^{0.233} * Pr^{0.064}$	$10^{12} \longrightarrow 2x10^{16}$
	Side/Down	$Nu = 0.3 * Ra^{0.22}$	
INEEL [9]	Upward	$Nu = 2.4415 * Ra^{0.1772}$	$10^{12} \longrightarrow 2x10^{16}$
	Side/Down	$Nu = 0.1857 * Ra^{0.2304} \left(\frac{H}{R}\right)^{0.25}$	
Mini-ACOPO [8]	Upward	$Nu = 0.345 * Ra^{0.233}$	$10^{12} \longrightarrow 7x10^{14}$
	Side/Down	$Nu = 0.0038 * Ra^{0.35} \left(\frac{H}{R}\right)^{0.25}$	$3x10^{13} \longrightarrow 7x10^{14}$
Kulacki-Emara & Mayinger [23] [22]	Upward (K-E)	$Nu = 0.345 * Ra^{0.226}$	$2x10^{4} \longrightarrow 4.4x10^{12}$
	Side/Down (M)	$Nu = 0.55 * Ra^{0.2}$	$7x10^{6} \longrightarrow 5x10^{14}$
Early ACOPO [14]	Upward	$Nu = 1.95 * Ra^{0.18}$	$10^{12} \longrightarrow 2x10^{16}$
	Side/Down	$Nu = 0.3 * Ra^{0.22}$	

These correlations were chosen based on their use in previous models and studies, as well as the use of the ACOPO correlation in the developed NCSU model. The original work performed for the DoE by Theofanous et al utilized the mini-ACOPO correlations

developed by experiments using AP600 parameters. The INEEL revision by Rempe et al utilized the ACOPO data and created their own “best fit” correlation set while the IVRAM model developed by Esmaili et al used a combination of the Kulacki-Emara correlation for upward facing heat transfer in the oxide pool and the Mayinger correlation for downward facing transfer. The early ACOPO correlation represents the correlation without the dependence of the Prandtl number. This Prandtl number effect and reliance was discussed in a report prepared for the US NRC from the UCSB Center for Risk Studies and Safety (CRSS) [25] as well as work by Dinh and Nourgaliev [19].

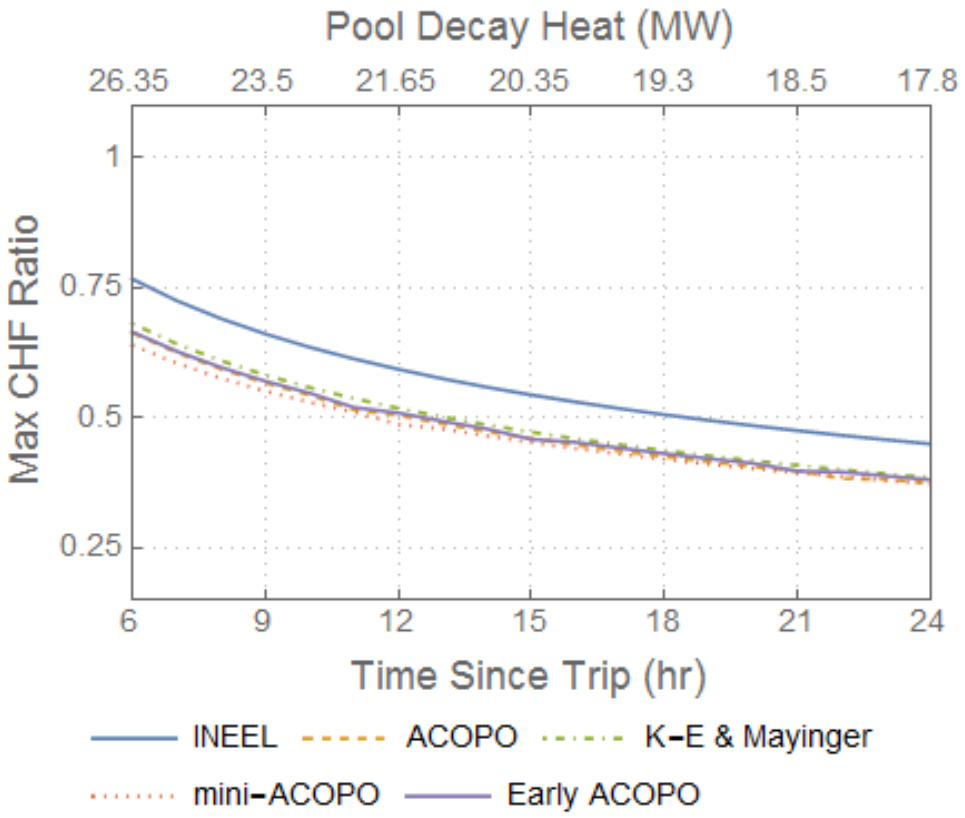

Figure 4-18: Analysis of model sensitivity to Nusselt correlation

Figure 4-18 shows the results of the correlation comparison study. The results indicate that the INEEL correlation produces the most conservative assessment of thermal margin while the ACOPO family and Kulacki-Emara/Mayinger combination produce less

conservative results. The maximum values for local CHF ratio at the onset of the simulation at t = 6 hours range from 0.7665 for the INEEL to 0.6395 for mini-ACOPO. At t = 24 hours, the values range from 0.3719 to 0.4491. In both cases, the INEEL correlation represents an approximate 20% increase in maximum CHF ratio from the ACOPO results. This value represents a partial uncertainty specifically due to the oxide pool Nusselt correlations and constitutes a small portion of the overall model uncertainty. By utilizing the fast running nature of the model coupled with the quasi-transient ability demonstrated previously, this type of sensitivity analysis may be performed for a variety of parameters.

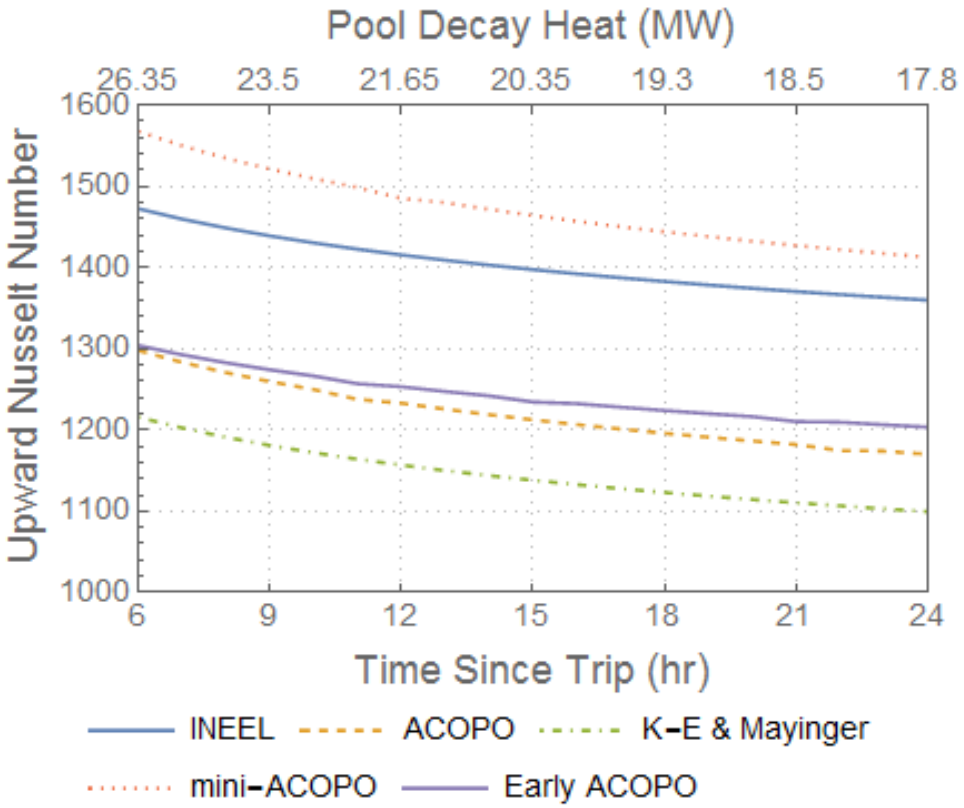

Figure 4-19: Upward facing Nusselt number in OX pool for various correlations

Figure 4-19 and Figure 4-20 show values for the upward and downward facing Nusselt numbers for the correlation sensitivity study. Higher downward facing Nusselt numbers and lower upward Nusselt numbers lower the heat transferred to the metallic layer. It has been established in the parametric studies presented previously that the highest

heat flux is generally observed in the metallic layer. Thus, the limiting of heat flux to this layer will raise the overall minimum thermal margin in a given scenario. Based on Figure 4-20, the results for the downward facing Nusselt number, it is easy to see the trend established by Figure 4-18. Looking at the upward facing results, however, it is not as obvious, especially when considering the combination of effects. In order to understand this combinative effect, a comparison must be made between the energy splitting values for each trial.

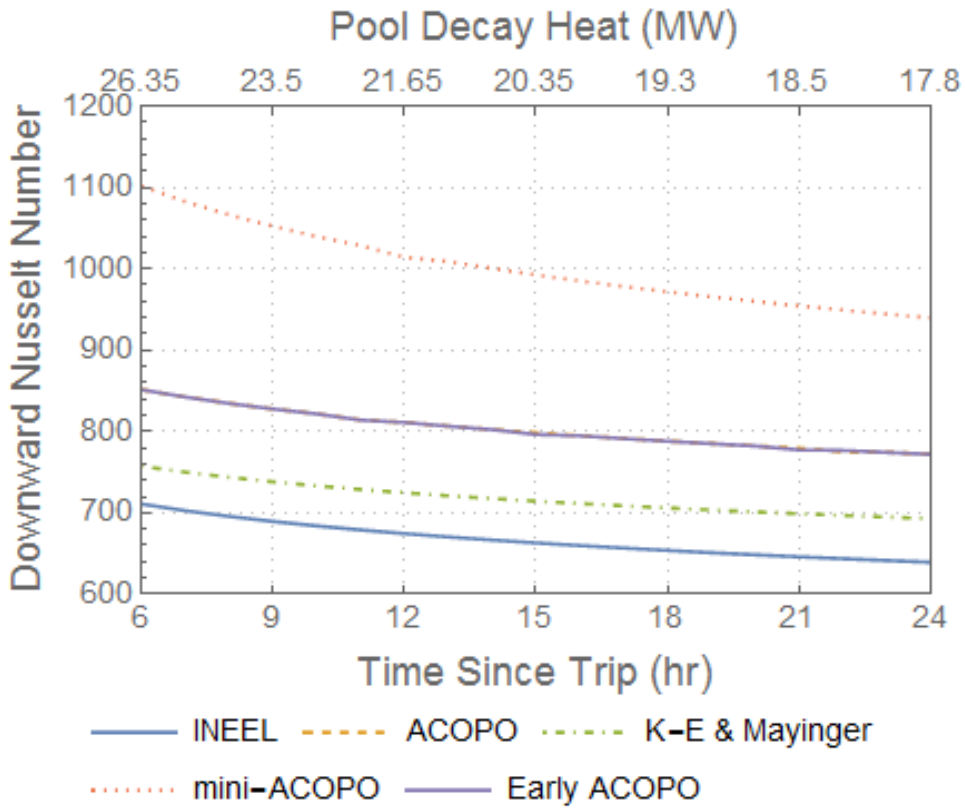

Figure 4-20: Downward facing Nusselt number in OX pool for various correlations

Energy splitting refers to the ratio of heat imparted to the upward facing area of the oxide pool to that of the downward facing area. It is governed by the following equation:

$$R_{ES} = \frac{q''_{up} A_{up}}{q''_{dn} A_{dn}}$$

Here, the areas denote total surface area for that direction. With no geometric or pool composition changes in this comparative study, the ratio of the top area to the bottom remains constant at 0.62. Additionally, since the rest of the scenario remains identical, the heat flux ratio may be realized as a ratio of Nu numbers instead. Thus, by substituting the previously determined Nu numbers, the energy splitting may be found for all cases and is presented in Figure 4-21.

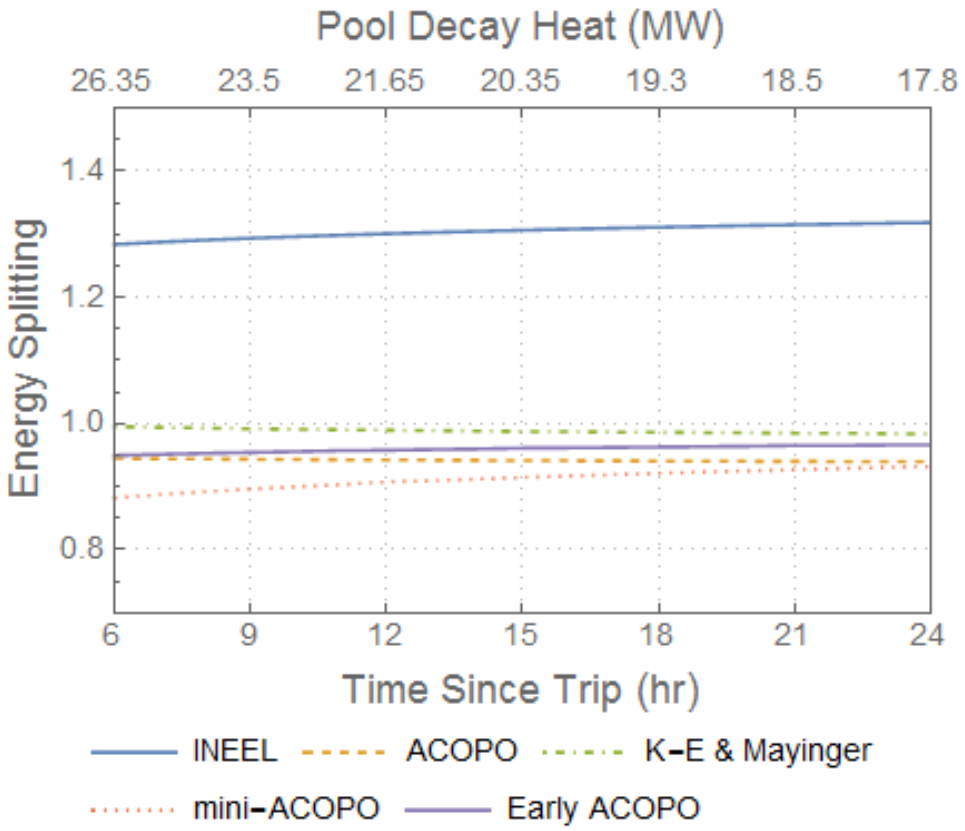

Figure 4-21: Energy splitting comparison for various correlations

Now it is possible to see the combinative effects of both directional Nu numbers for each correlation. The values of the INEEL energy splitting indicate that while the development of their best-fit correlation may track well with the ACOPO data, it produces abnormal results concerning the physics of melt pool convection.

4.5 Future Work

One possible application of the current model is to create a map of different core loading, geometric, and decay heating scenarios in order to provide quick reference for failure regimes. Such a map is presented in Figure 4-22. The map was created by running seven different decay heating values for three different oxide pool loading situations and five different metallic layer loadings. This procedure was repeated for hemispherical and elliptical geometries. The result is a dynamic view of 210 different accident scenarios. Quick reference levels provide CHF thresholds as well as the associated times when the chosen decay heat levels would be experienced.

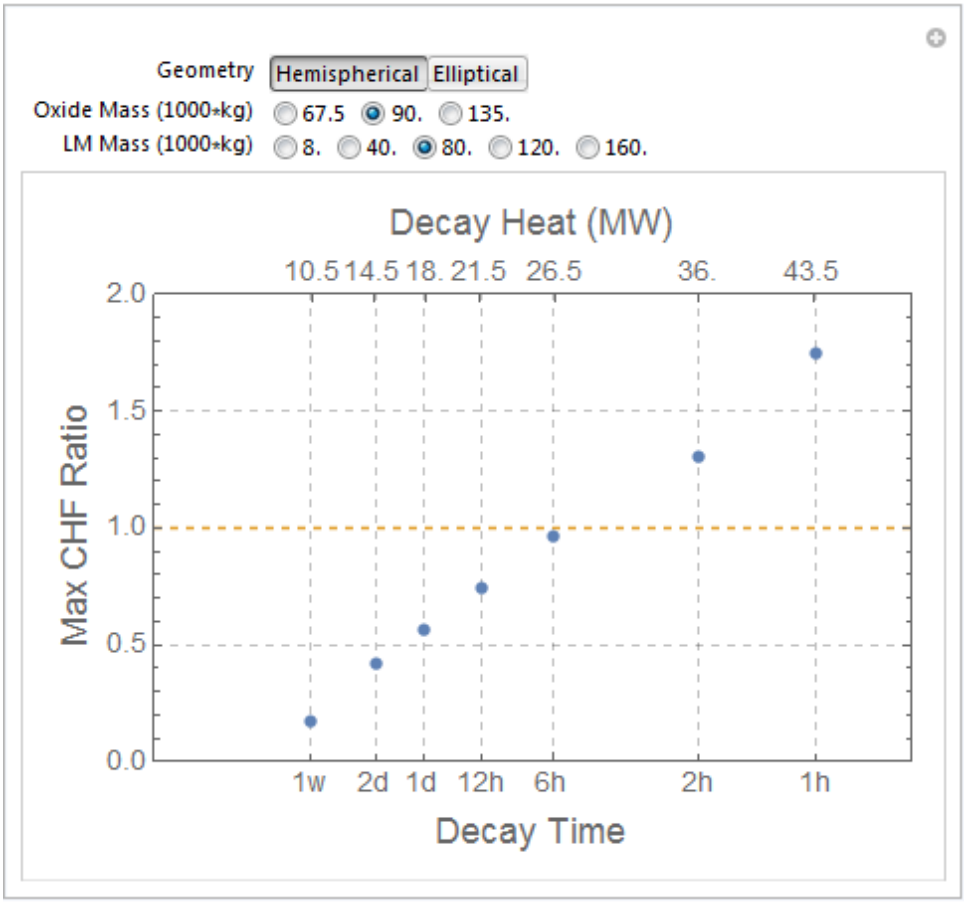

Figure 4-22: Example minimum thermal margin progression over time for selected conditions

This type of product from the model demonstrates a meaningful summary of a scenario and a quick reference for the expected safety margin. Repetition of this analysis for an increased spectrum of core loading values would create a predictive aid for steady state coolability regimes. This type of information could be used in an accident scenario to inform SAMG procedures based on current and predicted future conditions.

Additional work for this project would include a better assessment of the process uncertainty as well as measures to provide uncertainty reduction to IVR analysis. Such a reduction would come from an adaptive process for determining heat transfer correlations based on run parameters and fluid properties. By utilizing the ranges of applicability for each individual correlation for a given heat flux direction in a layer, a best-fit approach determines the lowest uncertainty correlation for the current Rayleigh and Prandtl numbers which then ultimately reduces the uncertainty of the entire analysis. By testing the sensitivity of such an approach to that of a constant heat transfer correlation, a broader determination to the effect of correlation on overall system analysis may be made as well.

Other modules of interest and areas for improvement to be considered include the utilization of live determination of fluid properties in a computationally transient environment, inclusion of pool formation models to allow mass transfer determination between corium layers, an individual vessel wall heat transfer model coupled to the system for improved determination of ablation physics, and, finally, integration into a module-based platform such as *Modelica* for easier coupling to external data and assimilation into larger system models.

5 CONCLUSIONS

The developed analytic capability was able to characterize heat transfer throughout a well-formed pool of corium in a reactor lower head. The heat transfer results were then used to predict vessel failure by determining thermal margin to critical heat flux on the exterior of the vessel. This analysis was performed for both AP1000 reactor conditions, with a hemispherical lower head geometry, and also for a SMR design [6] including an elliptical lower head geometry. The results for the AP1000 design trended with those of previous studies such as the IVRAM [7] analysis performed by Esmaili et al. Two key differences in the two models were the selection of correlations for the oxide pool and

metallic layer as well as the treatment of ULPU-derived CHF correlations [11] for the vessel. Due to these selections, the NCSU model proved overall to be more conservative when predicting thermal margin, especially in the region of the vessel bottom. Overall, the AP1000 parametric studies identified conditions when the metallic layer of a formed corium pool becomes the major threat to vessel integrity. This confirms the mass of the light metal layer is a crucial accident progression parameter due to the focusing effect phenomena.

The developed model provided equivalent analysis of an SMR type design. Public data for the B&W mPower reactor provided the required specifications for the SMR exercises. Overall the SMR design was more resistant to vessel failure due to CHF, largely due to the lower thermal power rating of the design. It was also shown that the elliptical lower head utilized in the SMR design offered a 50% increased higher decay heating threshold to reach CHF values than an equivalent hemispherical model. Both geometries, however, required at least a 40% higher decay heating than would normally be experienced at a time of one day post-reactor trip in order to see boiling crisis conditions on the vessel exterior. This evaluation strongly supports IVR as a viable strategy for severe accident management for the SMR safety case.

Finally, a quasi-transient analysis was performed and an application utilizing run aggregation to develop accident progression insight was created. The quasi-transient results used updating decay heating properties along with time-dependent parameter changes such as mass additions to plot a progression of steady state values for maximum CHF ratio over time. This application was a stepping stone to fully transient analysis and demonstrates the ability to contribute to SAMG research by pre-conditioning to certain event tree locations and simulating accident progression from that point. This will help to better inform approaches such as PRA which rely on a transient structure. The developed application can quickly display thermal margin results for a variety of scenarios and would be useful to guide SAMG planning based on future situations.

The quasi-transient framework was then used to perform a sensitivity study for the model's response to different Nusselt number correlations in the oxide pool layer. The study revealed the relative conservative nature of each correlation in addition to a

quantified range of values and thus an idea of the contribution to total uncertainty provided by the oxide pool correlations. Future applications and developments could inform uncertainty values for other parameters and thus inform the uncertainty of the entire model. Overall these results reflect and fulfill the stated goals of the project and contribute to the development of IVR methods for light water reactor safety design.

REFERENCES

[1] B. R. Sehgal, Ed., Nuclear safety in light water reactors: Severe accident phenomenology, Academic Press, 2012.

[2] R. R. Nourgaliev, "Modeling and analysis of heat and mass transfer processes during in-vessel melt progression stage of light water reactor (LWR) severe accidents," Stockholm, Sweden, 1998.

[3] T. L. Schulz, J. H. Scobel and D. T. McLaughlin, "Westinghouse AP1000 PRA maturity," in *Proc. of International Congress on Advances in Nuclear Power Plants (ICAPP)*, Seoul, Korea, 2005.

[4] J. H. Scobel, Y. Masset, R. Lutz, R. Solano, C. Zozula, J. Kitzmiller, L. Oriani and M. G. Plys, "Using accident management to address phenomenological uncertainties related to lower plenum debris bed chemistry and mixing during in-vessel retention (IVR) of molten core debris in the AP1000 passive plant," in *Proc. of International Congress on Advances in Nuclear Power Plants (ICAPP)*, Nice, France, 2011.

[5] T. L. Schulz, "Westinghouse AP1000 advanced passive plant," *Nuclear Engineering and Design*, vol. 236, no. 14, pp. 1547-1557, 2006.

[6] J. A. Halfinger and M. D. Haggerty, "The B&W mPower™ Scalable, Practical Nuclear Reactor Design," *Nuclear Technology*, vol. 178, no. 2, pp. 164-169, 2012.

[7] H. Esmaili and M. Khatib-Rahbar, "Analysis of likelihood of lower head failure and ex-vessel fuel coolant interaction energetics for AP1000," *Nuclear Engineering and Design*, vol. 235, no. 15, pp. 1583-1605, 2005.

[8] T. G. Theofanous, C. Liu, S. Additon, S. Angelini, O. Kymäläinen and T. Salmassi, "In-vessel coolability and retention of a core melt," *Nuclear Engineering and Design*, vol. 169, no. 1, pp. 1-48, 1997.

[9] J. L. Rempe, D. L. Knudson, C. M. Allison, G. L. Thinnes and C. L. Atwood, "Potential for AP600 in-vessel retention through ex-vessel flooding," Idaho Falls, ID, 1997.

[10] H. Park and V. K. Dhir, "Effect of Outside Cooling on the Thermal Behavior of a Pressurized Water Reactor Vessel Lower Head," *Nuclear Technology,* vol. 100, no. 3, pp. 331-346, 1992.

[11] T. N. Dinh, J. P. Tu, T. Salmassi and T. G. Theofanous, "Limits of coolability in the AP1000-related ULPU-2400 configuration V facility," in *The 10th International Topical Meeting on Nuclear Reactor Thermal Hydraulics (NURETH-10)*, Seoul, Korea, 2003.

[12] Wolfram Research, Inc., *Mathematica, Version 10.0,* Champaign, IL, 2014.

[13] W. M. Rohsenow, *A method of correlating heat transfer data for surface boiling of liquids*, Cambridge, Mass: M.I.T. Division of Industrial Cooporation, 1951.

[14] T. G. Theofanous and S. Angelini, "Natural Convection for In-Vessel Retention at Prototypic Rayleigh Numbers," *Nuclear Engineering and Design,* vol. 200, no. 1-2, pp. 1-9, 2000.

[15] O. Kymäläinen, H. Tuomisto, O. Hongisto and T. G. Theofanous, "Heat flux distribution from a volumetrically heated pool with high Rayleigh number," *Nuclear Engineering and Design,* vol. 149, no. 1, pp. 401-408, 1994.

[16] T. N. Dinh and R. R. Nourgaliev, "Turbulence modelling for large volumetrically heated liquid pools," *Nuclear Engineering and Design,* vol. 169, no. 1, pp. 131-150, 1997.

[17] S. Globe and D. Dropkin, "Natural Convection Heat Transfer in Liquid Confined by Two Horizontal Plates and Heated from Below," *J. Heat Transfer,* vol. 81, no. 1, pp. 24-28, 1959.

[18] T. C. Chawla and S. H. Chan, "Heat transfer from vertical/inclined boundaries of heat-generating boiling pools," *Journal of Heat Transfer,* vol. 104, no. 3, pp. 465-473, 1982.

[19] R. R. Nourgaliev, T. N. Dinh and B. R. Sehgal, "Effect of fluid Prandtl number on heat transfer characteristics in internally heated liquid pools with Rayleigh numbers up to 10^12," *Nuclear Engineering and Design,* vol. 169, no. 1, pp. 165-184, 1997.

[20] T. G. Theofanous and C. Liu, "Natural convection experiments in a hemisphere with Rayleigh numbers up to 10^15," in *ANS National Heat Transfer Conference*, Portland, OR, 1995.

[21] W. L. Oberkampf and T. G. Trucano, "Verification and Validation Benchmarks," *Nuclear Engineering and Design,* vol. 238, no. 3, pp. 716-743, 2008.

[22] F. Mayinger, M. Jahn, H. H. Reineke and V. Steinbrenner, "Examination of thermohydraulic processes and heat transfer in a core melt," *BMFT RS,* vol. 48, no. 1, 1976.

[23] F. A. Kulacki and A. A. Emara, "High Rayleigh number convection in enclosed fluid layers with internal heat sources," Ohio State University, Dept. of Mechanical Engineering, Columbus, OH, 1975.

[24] S. W. Churchill and H. H. Chu, "Correlating equations for laminar and turbulent free convection from a vertical plate," *International Journal of Heat and Mass Transfer,* vol. 18, no. 11, pp. 1323-1329, 1975.

[25] T. G. Theofanous and T.-N. Dinh, "In-Vessel Coolability and Melt Retention," 2002.

APPENDIX

APPENDIX A AP1000 GEOMETRY PARAMETRIC RESULTS

A.1 Case H1/E1

Table 7-1: Case H1 and E1 Parameters

Decay Heat (MW)	Oxide Pool Mass (kg)	Light Metal Mass (kg)
14.625 (1.0x)	88780 (1.0x)	79600 (1.0x)

This is the base case for the runs and calculations. The first series denotes data points taken from the oxide pool section while the second series denotes points from the light metal layer. The sets using (x) plot markers represent the same case but with an ellipse ratio of 3.0 (correlating to the ratio between the axes of the ellipse). For this case at nominal values for decay heat and core loading, the system does not reach critical heat flux (CHF) on the exterior surface. Thus, the accepted criteria for vessel failure is not reached in this steady state example. Additionally, this case confirms logical trends to be expected in the results: the heat flux increases with angular position or vertical position, the metallic layer demonstrates greater heat flux values than the oxide pool, and the vessel thickness decreases once the vessel melting point has been established.

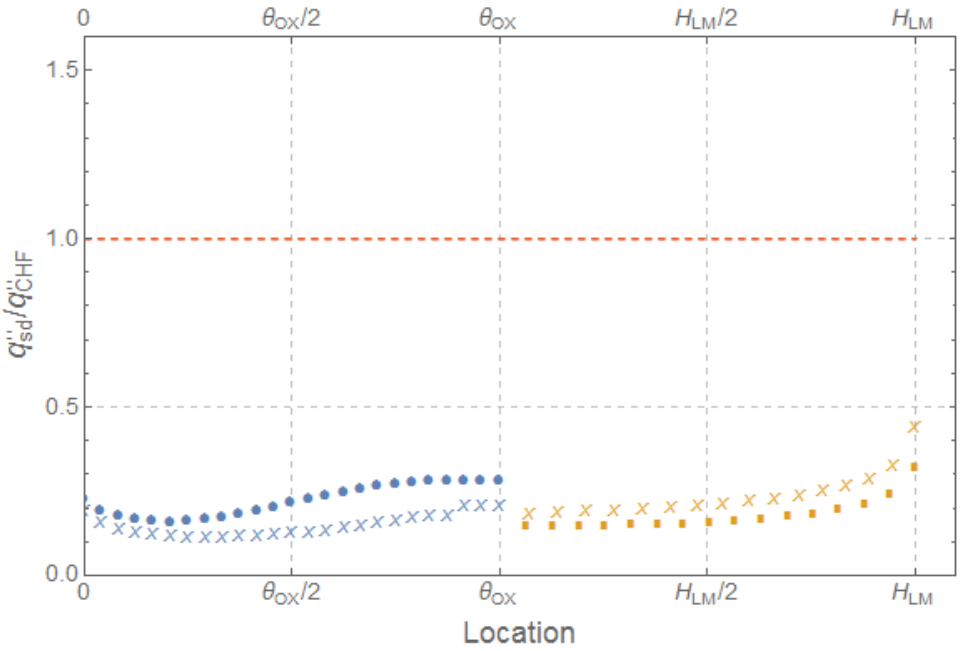

Figure 7-1: Results for cases H1 and E1 thermal margin to CHF

● – hemispherical data series x – elliptical data series

A.2 Case H2/E2

Table 7-2: Case H2 and E2 Parameters

Decay Heat (MW)	Oxide Pool Mass (kg)	Light Metal Mass (kg)
29.25 (2.0x)	88780 (1.0x)	79600 (1.0x)

This case demonstrates the effect of doubling the nominal decay heat expected from the base run. Here the upper nodes in the metallic layer exceed CHF levels and, thus, vessel failure is expected in this scenario. The effects of the COPO correlation are more readily visible in this example. The three oxide pool data points at the end of the elliptical series demonstrate the shift from the "downward" facing COPO heat flux to the "sideways" oriented heat flux correlation.

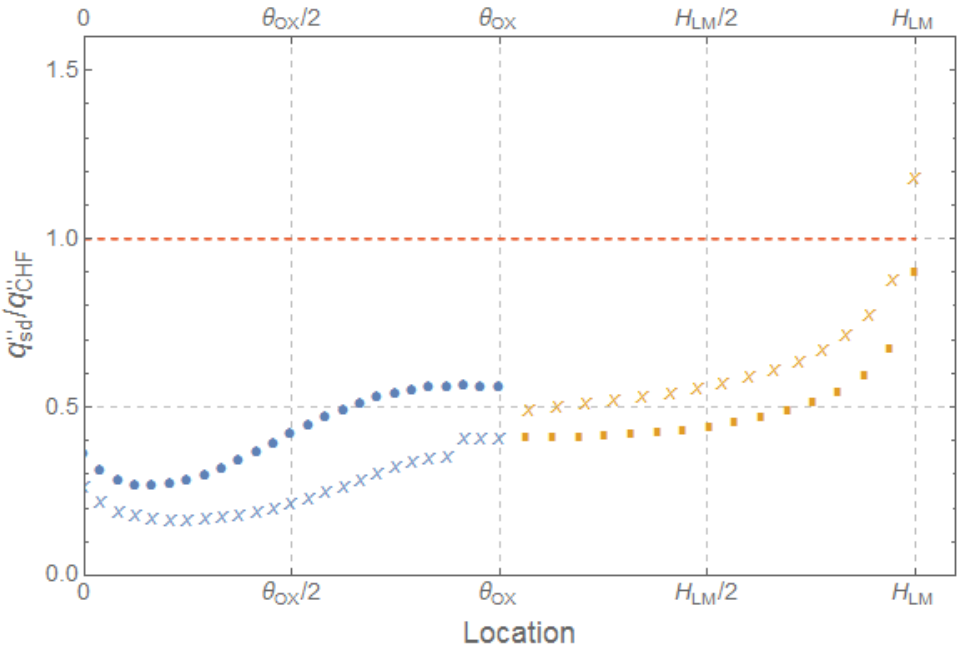

Figure 7-2: Results for cases H2 and E2 thermal margin to CHF

● – hemispherical data series x – elliptical data series

A.3 Case H3/E3

Table 7-3: Case H3 and E3 Parameters

Decay Heat (MW)	Oxide Pool Mass (kg)	Light Metal Mass (kg)
21.937 (1.5x)	88780 (1.0x)	79600 (1.0x)

Case 3 shows an intermediary view between cases 1 and 2. This is roughly the maximum value of decay heat allowable before a failure is observed for this core loading. Fortunately, as this is a 50% increase over nominal decay heat levels at a time of 2 days, this signals a representable margin to CHF for the nominal case.

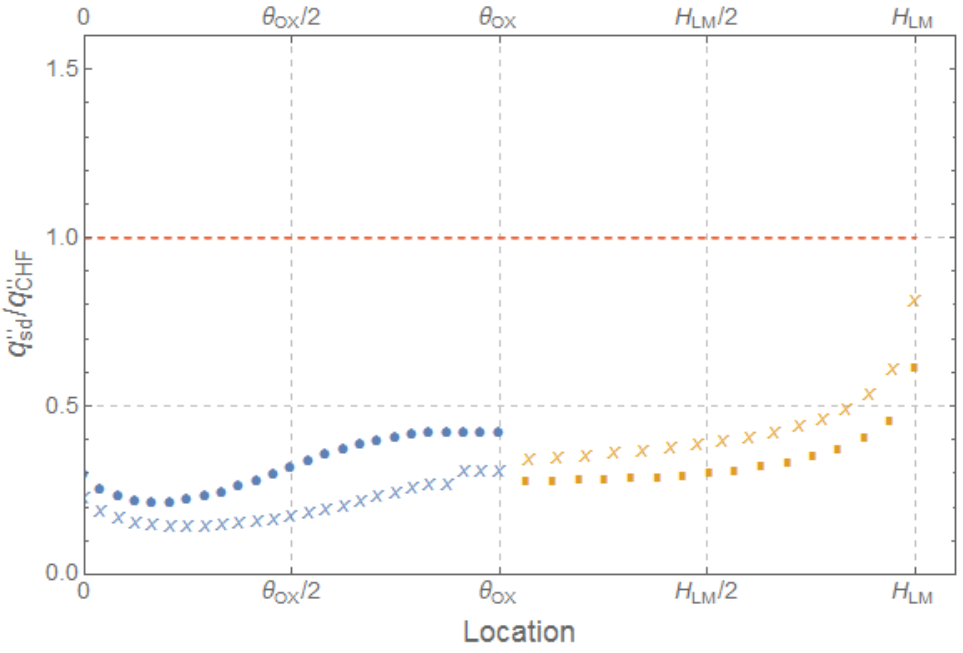

Figure 7-3: Results for cases H3 and E3 thermal margin to CHF

● – hemispherical data series x – elliptical data series

A.4 Case H4/E4

Table 7-4: Case H4 and E4 Parameters

Decay Heat (MW)	Oxide Pool Mass (kg)	Light Metal Mass (kg)
14.625 (1.0x)	88780 (1.0x)	159200 (2.0x)

Cases 4, 5, and 6 demonstrate the effect of a more massive metallic layer on the thermal margin of the vessel. At nominal decay heating as shown in Figure 7-4, the maximum heat flux determined is approximately 20% of the local CHF value. Compared to case 1, this is a reduction of the maximum fraction of CHF by 50%.

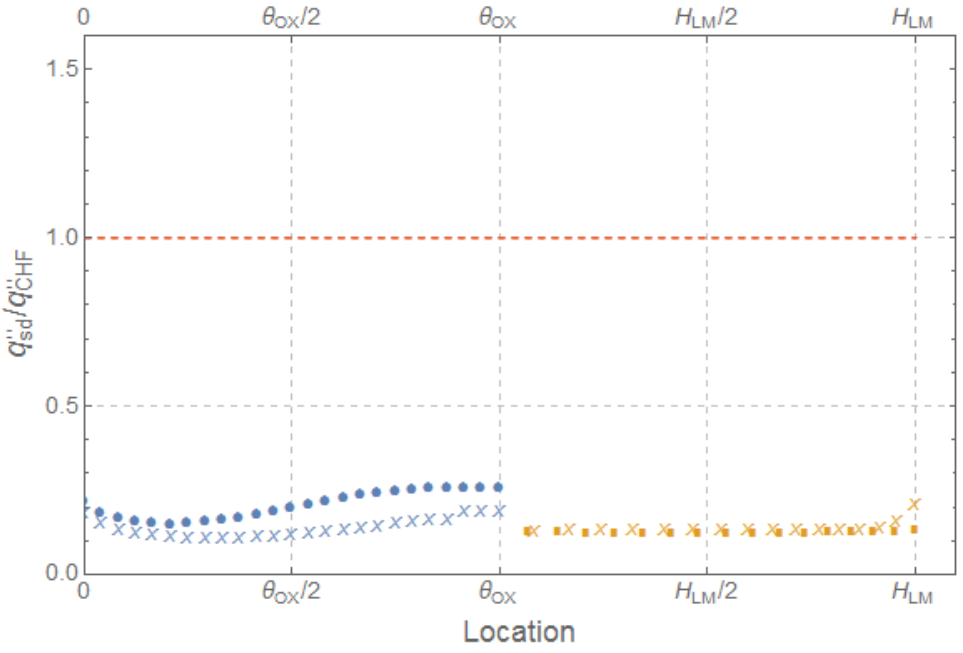

Figure 7-4: Results for cases H4 and E4 thermal margin to CHF

● – hemispherical data series x – elliptical data series

A.5 Case H5/E5

Table 7-5: Case H5 and E5 Parameters

Decay Heat (MW)	Oxide Pool Mass (kg)	Light Metal Mass (kg)
29.25 (2.0x)	88780 (1.0x)	159192 (2.0x)

Figure 7-5 shows the effect of a doubled nominal decay heat on a massive metallic layer. Compared to case 2 where the vessel exceeded CHF under similar decay heating conditions, this case shows heat flux levels remain well below the threat of CHF.

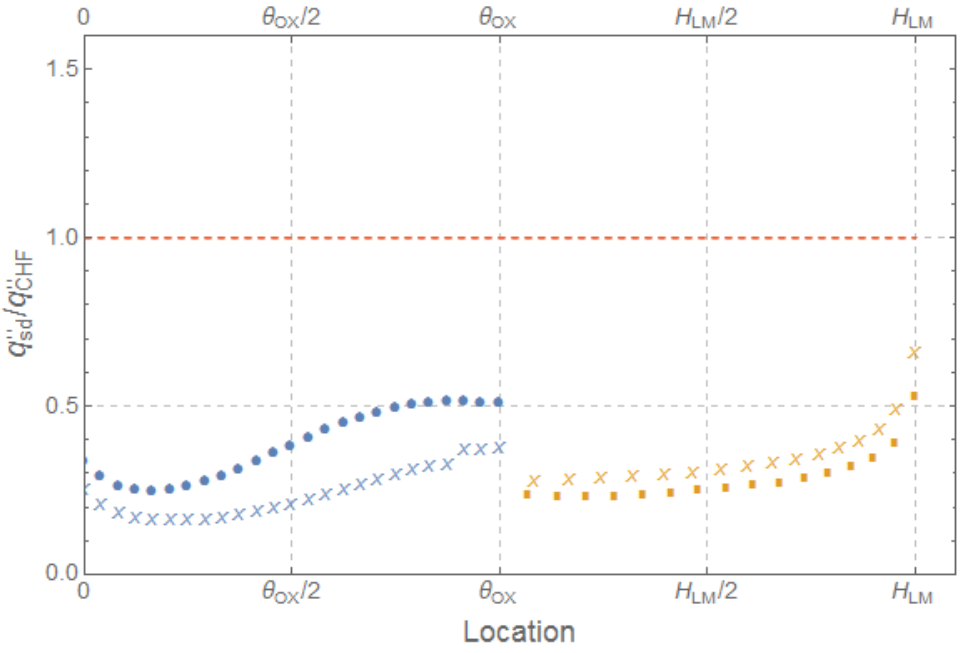

Figure 7-5: Results for cases H5 and E5 thermal margin to CHF

● – hemispherical data series x – elliptical data series

A.6 Case H6/E6

Table 7-6: Case H6 and E6 Parameters

Decay Heat (MW)	Oxide Pool Mass (kg)	Light Metal Mass (kg)
36.562 (2.5x)	88780 (1.0x)	159192 (2.0x)

This particular case demonstrates the effect of a massive metallic layer as compared to the base case. Comparing this case to case H2, the CHF levels are not exceeded in the geometry despite an even higher decay heat. This is due to the metallic layer's increased heat dispersion due to its larger volume. Another conclusion from this case is that the gap between the thermal margin for the oxide pool and metallic layer has lessened. By increasing the metallic layer mass further still, the oxide pool would become the layer in danger of exceeding CHF, but due to the disparity between layer masses necessary, this scenario is unlikely.

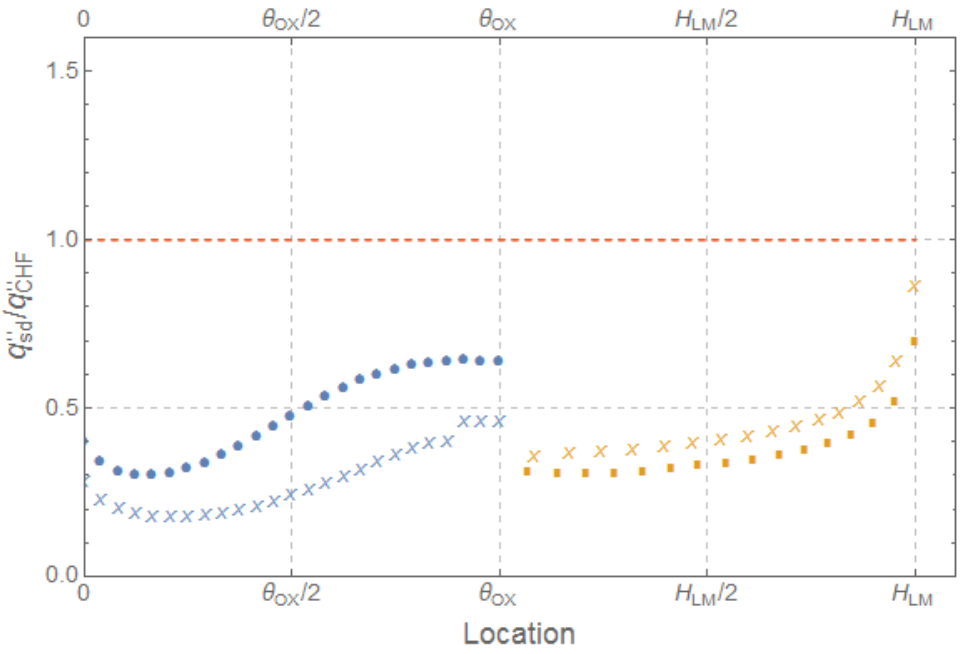

Figure 7-6: Results for cases H6 and E6 thermal margin to CHF

● – hemispherical data series x – elliptical data series

A.7 Case H7/E7

Table 7-7: Case H7 and E7 Parameters

Decay Heat (MW)	Oxide Pool Mass (kg)	Light Metal Mass (kg)
14.625 (1.0x)	88780 (1.0x)	7960 (0.1x)

Figure 7-7 demonstrates the focusing effect resulting from a thin metallic layer. Under this situation, the thin metallic layer can act as a reflector for the heat traveling from the top of the oxide pool. This reflection combined with the small surface area for the metallic layer to distribute heat leads to a rapid reduction in the vessel wall as heat fluxes greatly increase. Here, CHF has been exceeded throughout the metallic layer indicating a strong probability for failure of the lower head.

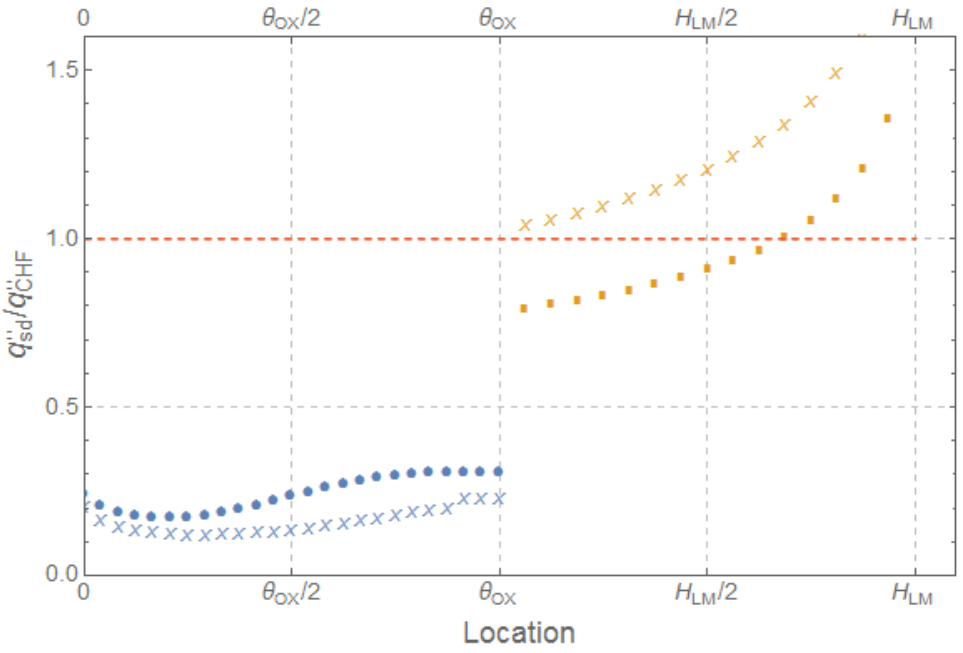

Figure 7-7: Results for cases H7 and E7 thermal margin to CHF

● – hemispherical data series x – elliptical data series

A.8 Case H8/E8

Table 7-8: Case H8 and E8 Parameters

Decay Heat (MW)	Oxide Pool Mass (kg)	Light Metal Mass (kg)
29.25 (2.0x)	88780 (1.0x)	7960 (0.1x)

Finally, Figure 7-8 demonstrates the combined effects of higher heat flux with the focusing effect. Here the total surface area in the metallic layer is utterly insufficient to distribute the incoming heat from the oxide pool well enough to avoid CHF. The entirety of the metallic layer shows heat flux levels more than double that of the CHF limit. Ultimately, the focusing effect remains the largest demonstrated threat to vessel integrity when considering thermal margin.

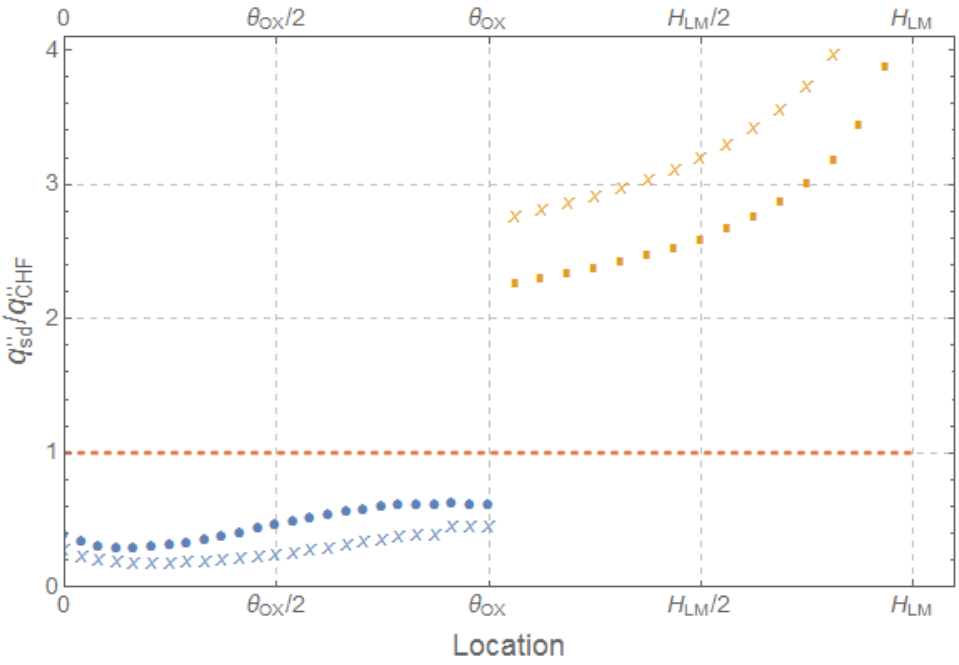

Figure 7-8: Results for cases H8 and E8 thermal margin to CHF

● – hemispherical data series x – elliptical data series

APPENDIX B MATERIAL PROPERTIES (ERI INPUT DECK)

Table 7-9: Material properties

Variable	Description	Units	Value
General			
C_{sf}	Empirical constant for C_{boil}	--	$1.30*10^{-2}$
T_{sat}	Coolant saturation temperature	K	400
σ	Stefan-Boltzmann constant	$W/m^2/K^4$	$5.6704*10^{-8}$
Upper Structures			
ε_s	Emissivity of reactor internal structures	--	0.45
A_s	Total surface area of interior structures	m^2	75.4
T_s	Temperature of internal structures	K	950
Oxide Pool and Ceramic Crust			
ρ_p, ρ_c	Density of pool and crust	kg/m^3	8191
$C_{p,p}, C_{p,c}$	Specific heat capacity of pool and crust	J/kg/K	533.2
T_{cor}	Melting temperature for oxide pool materials	K	2973
α_p	Thermal diffusivity for oxide pool	m^2/s	$1.12*10^{-6}$
α_c	Thermal diffusivity for crust material	m^2/s	$5.7*10^{-7}$
k_p	Thermal conductivity for oxide pool	W/m/K	5.3
k_c	Thermal conductivity for crust material	W/m/K	2.8
β_p	Thermal expansion coefficient for oxide pool	K^{-1}	$1.05*10^{-4}$
ν_p	Kinematic viscosity of oxide pool	m^2/s	$5.7*10^{-7}$
ε_c	Emissivity of oxide crust	--	0.8

Table 7-10: Material properties, continued

Metallic Layer			
ρ_m	Density of metallic layer	kg/m^3	6899.2
$C_{p,m}$	Specific heat capacity of metallic layer	J/kg/K	789.5
α_p	Thermal diffusivity for metallic layer	m^2/s	$4.59*10^{-6}$
k_p	Thermal conductivity for metallic layer	W/m/K	25.0
β_p	Thermal expansion coefficient for metallic layer	K^{-1}	$1.11*10^{-4}$
ν_p	Kinematic viscosity of metallic layer	m^2/s	$5.9*10^{-7}$
ε_c	Emissivity of metallic layer	--	0.8
Vessel			
k_v	Thermal conductivity for vessel	W/m/K	32.0
T_{ves}	Melting temperature for vessel	K	1600

APPENDIX C NCSU MODEL CODE AND BLOCK DIAGRAM

C.1 Block Diagram

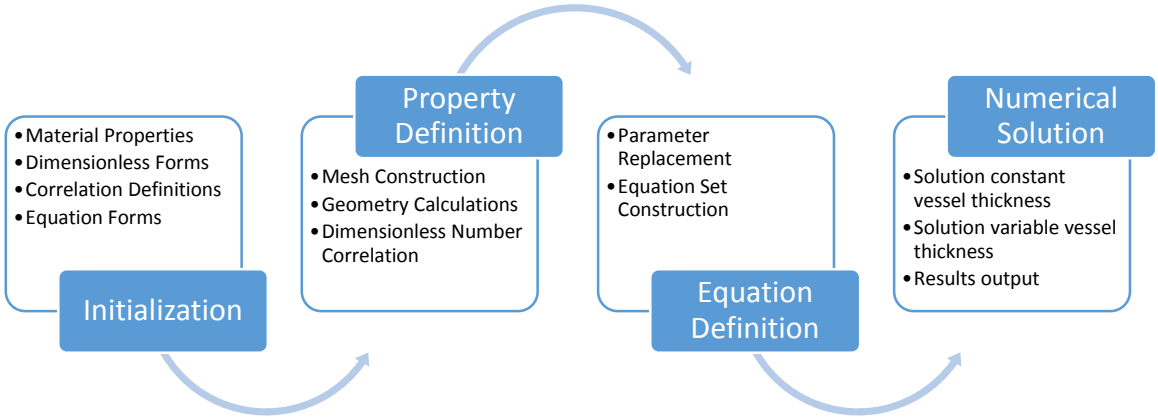

C.2 NCSU Model

Model presented on following page

Will Colmer

IVR Thermal Margin Model

General

```
Off[Solve::ifun, NSolve::ratnz, NIntegrate::izero]
```

Material Properties (ERI)

Misc.

```
σ = 5.670373 * 10^-8;
g = 9.81;

Tsat = 400. (*K*);
εs = 0.45;
εt = 0.8;
Csf = 1.3 * 10^-2;
As = 75.4 (*m^2*);
Ts = 950. (*K*);
```

Lower Head

```
kv = 32 (*W/(m*K)*);
Tves = 1600 (*K*);
δvo = 15 / 100 (*m*);
```

Oxide Pool

```
ρp = 8191(*kg/m^3*);
kp = 5.3(*W/(m*K)*);
νp = 5.7`*^-7(*m^2/s*);
μp = ρp * νp(*kg/(m*s)*);
Cpp = 533.2(*J/(kg*K)*);
αp = 1.12`*^-6(*m^2/s*);
βp = 1.05`*^-4(*K^-1*);
Tcor = 2973(*K*);
```

Crust

```
ρc = 8191(*kg/m^3*);
kc = 2.8(*W/(m*K)*);
Cpc = 533.2(*J/(kg*K)*);
αc = 5.7`*^-7(*m^2/s*);
εc = 0.8;
```

LM Layer

```
ρm = 6899.2(*kg/m^3*);
km = 25.0(*W/(m*K)*);
νm = 5.9`*^-7(*m^2/s*);
μm = ρm * νm(*kg/(m*s)*);
Cpm = 789.5(*J/(kg*K)*);
αm = 4.59`*^-6(*m^2/s*);
βm = 1.11`*^-4(*K^-1*);
```

Saturation

```
ρfsat = 937.361(*kg/m^3*);
hfsat = 533.592(*kJ/kg*);
μfsat = 218.32 * 10^-6(*kg/(m*s)*);
Cpfsat = 4255.79(*J/(kg*K)*);
σfsat = 0.0535473(*kg/s^2*);
kfsat = 0.683644(*W/(m*K)*);
Prfsat = 1.35908;

ρgsat = 1.37528(*kg/m^3*);
hgsat = 2715.91(*kJ/kg*);
Cpgsat = 2219.26(*J/(kg*K)*);
kgsat = 0.0283671(*W/(m*K)*);

hfgsat = hgsat - hfsat;
```

Decay Heat

$$\text{Pdecay}[\text{Po\_}, \text{t\_}] := \text{Po} * \begin{cases} 0.0603 * t^{-0.0639} & 0 \le t < 10 \\ 0.0766 * t^{-0.1810} & 10 \le t < 150 \\ 0.1300 * t^{-0.2830} & 150 \le t \end{cases};$$

$$\text{DecayFraction}[\text{t\_}] := \begin{cases} 0.0603 * t^{-0.0639} & 0 \le t < 10 \\ 0.0766 * t^{-0.1810} & 10 \le t < 150 \\ 0.1300 * t^{-0.2830} & 150 \le t \end{cases};$$

$$\text{PdPlot} := \text{Plot}\left[\frac{\text{Pdecay}[3415. * 10^6, \text{t}]}{10^6}, \{\text{t}, 600, 3 * 3600\}, \text{PlotRange} \to \text{All}, \text{AxesOrigin} \to \{600, \text{Automatic}\}, \text{AxesLabel} \to \{\text{"time (s)"}, \text{"}Q_{decay}\text{ (MW)"}\}\right];$$

PdPlot

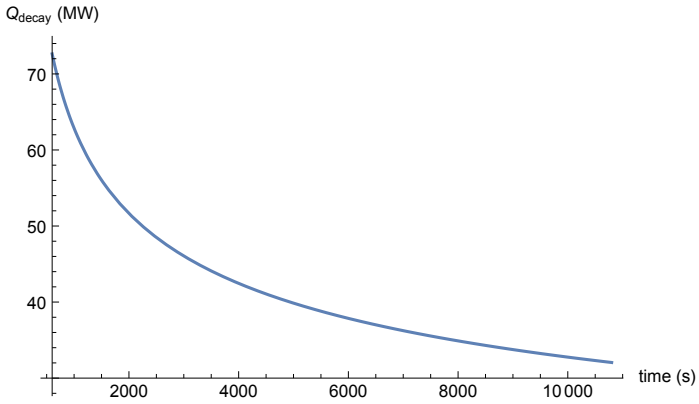

Geometry

Heights

$$\text{Hcrit} := \frac{\text{rLP}}{\text{fLP}};$$

Volume

$$\text{Vcint}[\text{Hlo\_}, \text{Hhi\_}] := -\int_{\text{Max}[0.0,\text{Hcrit}-\text{Hhi}]}^{\text{Max}[0.0,\text{Hcrit}-\text{Hlo}]} \pi \left(\text{rLP}^2 - \text{fLP}^2\, y^2\right) dy;$$

$$\text{Vox}[\text{Hhm\_}, \text{Hox\_}] :=$$
$$\text{Vcint}[\text{Hhm}, \text{Hhm} + \text{Hox}] + \text{Max}\left[0.0, \int_{\text{Hcrit}}^{\text{Hox}+\text{Hhm}} \pi\, \text{rLP}^2\, dx - \text{Max}\left[0.0, \int_{\text{Hcrit}}^{\text{Hhm}} \pi\, \text{rLP}^2\, dx\right]\right];$$

$$\text{Vlm}[\text{Hhm\_}, \text{Hox\_}, \text{Hlm\_}] := \text{Vcint}[\text{Hhm} + \text{Hox}, \text{Hhm} + \text{Hox} + \text{Hlm}] +$$
$$\text{Max}\left[0.0, \int_{\text{Hcrit}}^{\text{Hox}+\text{Hhm}+\text{Hlm}} \pi\, \text{rLP}^2\, dx - \text{Max}\left[0.0, \int_{\text{Hcrit}}^{\text{Hhm}+\text{Hox}} \pi\, \text{rLP}^2\, dx\right]\right];$$

Area & Angle

$$\text{rell}[\theta\_] := \begin{cases} \frac{\text{rLP}^2}{\text{fLP}} \left(\frac{\text{rLP}^2 \left(\text{fLP}^2 \text{Cos}[\theta]^2 + \text{Sin}[\theta]^2\right)}{\text{fLP}^2}\right)^{-0.5} & 0 \le \theta \le \frac{\pi}{2} \\ \frac{\text{rLP}}{\text{Cos}\left[\theta - \frac{\pi}{2}\right]} & \frac{\pi}{2} < \theta \le \pi \end{cases};$$

$$\kappa[\theta\_] := \frac{\text{Abs}\left[\frac{4\,\text{Cos}[\theta]^2}{3} + \frac{4\,\text{Sin}[\theta]^2}{3}\right]}{\left(4\,\text{Cos}[\theta]^2 + \frac{4\,\text{Sin}[\theta]^2}{9}\right)^{3/2}};$$

$$\text{rcurv}[\theta\_] := \frac{1}{\kappa[\theta]};$$

$$\theta\text{h}[\text{h\_}] :=$$
$$\text{Abs}\left[\theta /. \text{Solve}\left[\frac{\text{rLP}}{\text{fLP}} - \frac{\text{rLP}^2}{\text{fLP}} \left(\frac{\text{rLP}^2 \left(\text{fLP}^2 \text{Cos}[\theta]^2 + \text{Sin}[\theta]^2\right)}{\text{fLP}^2}\right)^{-0.5} * \text{Cos}[\theta] ==$$
$$\text{Min}[\text{h}, \text{Hcrit}], \theta\right][[1]]\right] + \text{If}\left[\text{h} > \text{Hcrit}, \text{N}\left[\text{ArcTan}\left[\frac{\text{h} - \text{rLP} / \text{fLP}}{\text{rLP}}\right]\right], 0\right];$$

$$\text{Aflat}[\theta\_] := \pi \left(\text{rell}\left[\text{Min}\left[\theta, \frac{\pi}{2}\right]\right] * \text{Sin}\left[\text{Min}\left[\theta, \frac{\pi}{2}\right]\right]\right)^2;$$

$$\text{Aflat}\delta[\theta\_, \delta\_] := \pi * \text{Max}\left[0, \left(\text{rell}\left[\text{Min}\left[\theta, \frac{\pi}{2}\right]\right] * \text{Sin}\left[\text{Min}\left[\theta, \frac{\pi}{2}\right]\right] - \delta\right)\right]^2;$$

```
Aell[θ1_, θ2_] := { NIntegrate[NIntegrate[
    Sqrt[(1/2) rLP^2 (rLP^2 + rLP^2/fLP^2 + (rLP^2 - rLP^2/fLP^2) Cos[2 θ]) Sin[θ]^2],
    {θ, θ1, θ2}], {ϕ, 0, 2 π}]
  NIntegrate[NIntegrate[
    Sqrt[(1/2) rLP^2 (rLP^2 + rLP^2/fLP^2 + (rLP^2 - rLP^2/fLP^2) Cos[2 θ]) Sin[θ]^2],
    {θ, θ1, π/2}], {ϕ, 0, 2 π}]
  0
```

```
Aellδ[θ1_, θ2_, δ_] :=

 { NIntegrate[                                                          0 < θ2 ≤ π/2
    NIntegrate[Sqrt[(1/2) (rLP - δ)^2 (rLP^2 + rLP^2/fLP^2 - 2 rLP δ - 2 rLP δ/fLP +
          2 δ^2 + (rLP - rLP/fLP) (rLP + rLP/fLP - 2 δ) Cos[2 θ])
        Sin[θ]^2], {θ, θ1, θ2}], {ϕ, 0, 2 π}]
   NIntegrate[                                                          θ1 ≤ π/2 && θ2 >
    NIntegrate[Sqrt[(1/2) (rLP - δ)^2 (rLP^2 + rLP^2/fLP^2 - 2 rLP δ - 2 rLP δ/fLP +
          2 δ^2 + (rLP - rLP/fLP) (rLP + rLP/fLP - 2 δ) Cos[2 θ])
        Sin[θ]^2], {θ, θ1, θ2}], {ϕ, 0, 2 π}]
   0                                                                    □
```

```
Acyl[h_] := 2 π rLP * h;
Acylδ[h_, δ_] := 2 π (rLP - δ) h;
```

Dimensionless Numbers

```
Pr := Cp * μ / k;
Gr := g * β * H^3 * ΔT / (μ / ρ)^2;
Ra := g * β * Q * H^5 * ρ / (α * μ * k)
Ra' := Gr * Pr;
h := NU * k / H;
```

Nusselt Correlations

ACOPO & Mini-ACOPO

$$NUupAC := 0.3\, RaAC^{0.233}\, PrAC^{0.064};$$

$$NUdnAC := 0.3 * RaAC^{0.22};$$

$$NUupmAC := 0.345 * RamAC^{0.233};$$

$$NUdnmAC := 0.0038 * RamAC^{0.35} * \left(\frac{H}{R}\right)^{0.25};$$

COPO (Kymäläinen)

$$NUupCO := 0.345\, RaCO^{0.233};$$

$$NUsdCO := 0.85\, RaCO^{0.19};$$

$$NUdnCO := 0.54\, RacCO^{0.182} \left(\frac{Hc}{Rc}\right)^{0.26};$$

INEEL Best-Fit for ACOPO Data

$$NUupIN := 2.4415 * RaIN^{0.1772};$$

$$NUdnIN := 0.1857 * RaIN^{0.2304} * \left(\frac{H}{R}\right)^{0.25};$$

Globe-Dropkin & GDSpecial

$$NUupGD := 0.069\, RaGD^{0.333}\, PrGD^{0.074};$$

$$NUupGDs := 0.15\, RaGDs^{0.333};$$

Churchill-Chu & CCSpecial

$$NUsdCC := \left(0.825 + \frac{0.387\, RaCC^{1/6}}{\left(1 + \left(\frac{0.492}{PrCC}\right)^{9/16}\right)^{8/27}}\right)^2;$$

$$NUsdCCs := 0.076\, RaCCs^{1/3};$$

Chawla Chan

$$NUsdCh := 0.508\, PrCh^{0.25} \left(\frac{20}{21} + PrCh\right)^{-0.25} RaCh^{0.25};$$

Kulacki-Emara & Mayinger

$$NUupKE := 0.345\ (RaKE)^{0.226};$$

$$NUdnMA := 0.55\ (RaMA)^{0.2};$$

Early ACOPO

$$NUupTH := 1.95\ RaTH^{0.18};$$

$$NUdnTH := 0.3\ RaTH^{0.22};$$

Transient Adaptations

$$NUupTR := 0.25\ (RaTR)^{0.304};$$

$$NUdnTR := 0.472\ (RaTR)^{0.22} * \left(\frac{H}{R}\right)^{0.317};$$

Angular Dependence on downward facing oxide layer Nusselt number

$$f1\theta[\theta o\_, \theta\_] := 0.1 + 1.08\left(\frac{\theta}{\theta o}\right) - 4.5\left(\frac{\theta}{\theta o}\right)^2 + 8.6\left(\frac{\theta}{\theta o}\right)^3;$$

$$f2\theta[\theta o\_, \theta\_] := 0.41 + 0.35\left(\frac{\theta}{\theta o}\right) + \left(\frac{\theta}{\theta o}\right)^2;$$

$$f\theta[\theta o\_, \theta\_] := \begin{cases} f1\theta[\theta o, \theta] & 0.0 \le \left(\frac{\theta}{\theta o}\right) \le 0.6 \\ f2\theta[\theta o, \theta] & 0.6 < \left(\frac{\theta}{\theta o}\right) \le 1 \\ f2\theta[\theta o, \theta o] & \left(\frac{\theta}{\theta o}\right) > 1 \end{cases};$$

$$g\theta[\theta o\_, \theta\_] := \begin{cases} \left(b1 * \mathrm{Sin}[\theta]^2 + b2\right) & \theta \le \theta o \\ \left(b1 * \mathrm{Sin}[\theta o]^2 + b2\right) & \theta > \theta o \end{cases} /. \left\{b1 \to \frac{9.12\left(1 - \mathrm{Cos}[\theta o]\right)}{8 - 9\,\mathrm{Cos}[\theta o] + \mathrm{Cos}[3\,\theta o]},\ b2 \to 0.24\right\};$$

```
fθPlot := Show[Plot[gθ[π/2, x], {x, 0, π/2}, PlotStyle → ColorData[97, 1]],
   Plot[fθ[π/2, x], {x, 0, π/2}, PlotStyle → ColorData[97, 2]],
   Graphics[{DotDashed, Line[{{3 π/10, 0}, {3 π/10, 2}}]}],
   PlotRange → {All, {0, 2}}, AxesOrigin → {0, 0}, Frame → True,
   FrameTicks → {Table[{i π/12, i * 15}, {i, 0, 6}], All},
   FrameTicksStyle → 14, FrameLabel →
    {Style["Angular Position (°)", 18], Style["f_θ|θ_0=90°", 18]},
   Frame → True, GridLines → {Table[i π/12, {i, 0, 6}], Automatic},
   GridLinesStyle → Directive[Opacity[0.25], Dashed]];
fθPlot
```

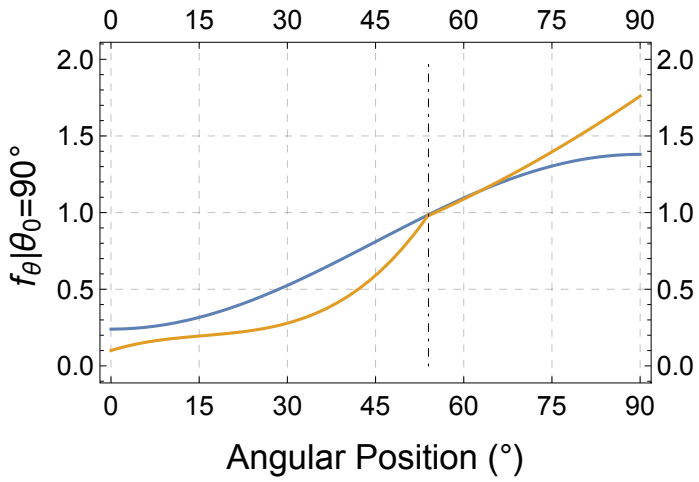

CHF Coefficients (AP600)

```
{Achf, Bchf, Cchf, Dchf, Echf} =
  {4.9`*^5, 3.02`*^4, -8.88`*^2, 13.5, -6.65`*^-2};
```

Equations

Oxide Pool

Top

$$peq[1] := qpup == hpup\ (Tpmx - Tcor);$$

$$peq[2] := qcup == \frac{kc}{\delta cup}\ (Tcor - Tcup) + \frac{1}{2}\ Qc * \delta cup;$$

$$peq[3] := qcup == qpup + Qc * \delta cup;$$

$$peq[4] := qrad == \sigma\left(Tcup^4 - Ts^4\right) * \left(\frac{1}{\varepsilon c} + \frac{1-\varepsilon s}{\varepsilon s} * \frac{Acup}{As}\right)^{-1};$$

Side

$$peq[5] := qpsd\theta == hpsd\theta\ (Tpmx - Tcor);$$

$$peq[6] := qcsd\theta == \frac{kc}{\delta csd\theta}\ (Tcor - Tcsd\theta) + \frac{1}{2}\ Qc * \delta csd\theta;$$

$$peq[7] := qcsd\theta == qpsd\theta + Qc * \delta csd\theta;$$

$$peq[8] := qcsd\theta == \frac{kv}{\delta v\theta}\ (Tcsd\theta - Tvo\theta);$$

$$peq[9] := qcsd\theta == Cboil\ (Tvo\theta - Tsat)^3;$$

Balance

$$peq[10] := Qp * Vcor == qcup * Acup + \Sigma qA\theta;$$

$$peq[11] := Hcor == Hp + \delta cup + \delta csd0;$$

LM Layer

$$meq[1] := qmsdH == hmsdH\ (Tmdn - TmsdH);$$

$$meq[2] := qmsdH == \frac{kv}{\delta vmH}\ (TmsdH - TvomH);$$

$$meq[3] := qmsdH == Cboil\ (TvomH - Tsat)^3;$$

$$meq[4] := qmup == hmup\ (Tmdn - Tmup);$$

$$meq[5] := qrad == \sigma\frac{\left(Tmup^4 - Ts^4\right)}{\frac{1}{\varepsilon t} - \frac{1-\varepsilon s}{\varepsilon s}\ \frac{Amup}{As}};$$

$$meq[6] := Qm * Vm + qsrc * Amdn == qmup * Amup + \Sigma qAH;$$

Coupled 2-Layer Solution

Solution Loop

```
solloop[QDM_, CMM_, LMM_, REM_] := Do[
    ρpen = 0;
    Label[start];
    (*--------------------------------------------------*)
    (*Input Variables*)
    Qt = 3415. * 10^6;
    td := trun;

    rLP = 2;
    fLP = REM * 1.0;

    mcor = CMM * 88 783.187;
    mLM = LMM * 79 595.958;

    nθ = 24;
    nH = 16;
    (*--------------------------------------------------*)
(*Height Determination (mass input only)*)
    Hcor = hh /. FindRoot[Vox[0, hh] == mcor/ρc, {hh, 1.0}];

    Hm = hh /. FindRoot[Vlm[0, Hcor, hh] == mLM/ρm, {hh, 1.0}];

    (*Hcor=1.52;
    Hm=1*0.9273;*)
    genout[0] := Grid[{{"H_OX", "H_LM"}, {Hcor, Hm}},
      Alignment → {Left, Bottom}, Frame → {All, False}];
    (*--------------------------------------------------*)
    (*Discretization*)
Clear[θi, Hmi, Hhmi];
    θmax = θh[Hcor];
    θgθ = Max[π/2, θmax];
    θmmax = θh[Hcor + Hm];
    Δθ = θmax/nθ;
For[i = 1, i ≤ nθ, i++,
```

```
    θi[0] = 0; θi[i] = i * Δθ;]
   Hmax = Hm;
  ΔH := Hmax/nH;
  nHh = 4 nH;
  ΔHh := Hmax/nHh;
  For[i = 0, i ≤ nH, i++,
   Hmi[i] = i * ΔH;
   θm[i] = θh[Hcor + i * ΔH];
  ];
  For[i = 0, i ≤ nHh, i++,
   Hhmi[i] = i * ΔHh;];
  genout[1] := Grid[Transpose[Prepend[
      Table[{i, θi[i], θi[i] * 180/π}, {i, 0, nθ}], {"i", "θi", "θi°"}]],
    Alignment → {Left, Bottom}, Frame → {All, False}];
(*-------------------------------------------------*)
  (*Geometry*)
  (*Area*)
  θcor = θh[Hcor];
Clear[Acsdθ, AmsdH];
  Acup = Aflat[θcor];
  For[i = 1, i ≤ nθ, i++,
   Acsdθ[i] = Aell[θi[i - 1], θi[i]];];
  Acsd = Aell[0, θcor] + Max[0, Acyl[Hcor - Hcrit]];

  Amdn = Acup;
  Amup = Aflat[θmmax];
  For[i = 1, i ≤ nH, i++,
   AmsdH[i] = Aell[θm[i - 1], θm[i]];];


  genout[2] := Grid[{{"A^up_crust", "ΣiAθi", "θcor"}, {Acup, Acsd, (θcor * 180/π)}},
    Alignment → {Left, Bottom}, Frame → {All, False}];
  genout[3] := Grid[MapThread[Append, {MapThread[Prepend, {Transpose[
        Table[{Round[θi[i - 1] * 180/π] ° → Round[θi[i] * 180/π] °, Acsdθ[i]},
         {i, 1, nθ}]], {"Δθ", "Aθi"}}], {"Total", Sum[Acsdθ[i], {i, 1, nθ}]}}],
```

```
    Alignment → {Left, Bottom}, Frame → {All, False}];
  genout[4] := Grid[{{"A_LM^up", "A_LM^down", "Σ_i A_Hi"},
     {Amup, Amdn, Aell[θcor, θmmax]}},
    Alignment → {Left, Bottom}, Frame → {All, False}];
  genout[5] := Grid[MapThread[Append, {MapThread[Prepend,
       {Transpose[Table[{Round[Hmi[i - 1], .0001] → Round[Hmi[i], .0001],
           AmsdH[i], Round[θm[i] * 180/π, .001] "°"}, {i, 1, nH}]],
        {"ΔH", "A_Hi", "θ_H"}}], {"Total", Sum_{i=1}^{nH} AmsdH[i], "--"}}],
    Alignment → {Left, Bottom}, Frame → {All, False}];
(*Volume*)
  Clear[Vcor, Vm];
  Vcor = Vox[0, Hcor];
  Vm = Vlm[0, Hcor, Hm];
  genout[6] :=
   Grid[{{"V_cor", "V_LM", "m_cor", "m_LM"}, {Vcor, Vm, Vcor ρc, Vm ρm}},
    Alignment → {Left, Bottom}, Frame → {All, False}];
(*Energy Splitting*)
  Qd = (QDM - ρpen * 0.01) * Pdecay[Qt, td];
  Qp = Qc = Qd / (Vcor + 0.1 Vm);
  Qm = 0.1 Qp;
(*------------------------------------------------------*)
  (*Dimensionless Numbers*)
  Cboil =
   Sqrt[g (ρliq - ρvap) / σliq] (Cpliq / (Prliq * (hfg * 1000) * Csf))^3 (μliq * 1000 * hfg) /.
    {ρliq → ρfsat, ρvap → ρgsat, σliq → σfsat, Prliq → Prfsat,
     Cpliq → Cpfsat, μliq → μfsat, hfg → hfgsat};
Prp = Pr /. {Cp → Cpp, μ → μp, k → kp};
  Rap = { Ra /. {β → βp, Q → Qp, H → (Hp),
      ρ → ρp, α → αp, μ → μp, k → kp}        corrALT == 0
          Ra /. {β → βp, Q → Qp,
      H → (Hcor^0.25 * Hp^0.75), ρ → ρp,
      α → αp, μ → μp, k → kp}                corrALT > 0 ||
                                              ValueQ[corrALT] == False
  Prm = Pr /. {Cp → Cpm, μ → μm, k → km};
  Ramup = Ra' /.
    {β → βm, H → Hm, ρ → ρm, μ → μm, k → km, Cp → Cpm, ΔT → (Tmdn - Tmup)};
```

```
Ramsd = Ra𝓁 /. {β → βm, H → y, ρ → ρm, μ → μm, k → km,
    Cp → Cpm, ΔT → (Tmup - TmsdH)};

(*-------------------------------------------------*)
  (*HTC Calculation*)
  If[ValueQ[corrALT], corrALT, corrALT = 1];
  If[fLP == 1,

                  ⎧ Simplify[NUupIN /. {RaIN → Rap},                  corrALT == 0
                   Assumptions :→ Hp ≥ 0]
                  ⎪ Simplify[NUupAC /. {RaAC → Rap, PrAC → Prp},      corrALT == 1
                   Assumptions :→ Hp ≥ 0]
                  ⎪ Simplify[NUupKE /. {RaKE → Rap},                  corrALT == 2
                   Assumptions :→ Hp ≥ 0]
   NUpup = Piecewise⎨ Simplify[NUupmAC /. {RamAC → Rap},                 corrALT == 3
                   Assumptions :→ Hp ≥ 0]
                  ⎪ Simplify[NUupTH /. {RaTH → Rap},                  corrALT == 4
                   Assumptions :→ Hp ≥ 0]
                  ⎪ Simplify[NUupAC /. {RaAC → Rap, PrAC → Prp},      ValueQ[corrA
                   Assumptions :→ Hp ≥ 0]
                  ⎩

   NUpup = Simplify[NUupCO /. {RaCO → Rap}, Assumptions :→ Hp ≥ 0];
  ];
  If[fLP == 1,

                  ⎧ Simplify[NUdnIN /. {RaIN → Rap, H → Hp, R → rLP},  corrALT == 0
                   Assumptions :→ Hp ≥ 0]
                  ⎪ Simplify[NUdnAC /. {RaAC → Rap, H → Hp, R → rLP},  corrALT == 1
                   Assumptions :→ Hp ≥ 0]
                  ⎪ Simplify[NUdnMA /. {RaMA → Rap},                   corrALT == 2
                   Assumptions :→ Hp ≥ 0]
   NUpsd = Piecewise⎨ Simplify[NUdnmAC /. {RamAC → Rap, H → Hp, R → rLP}, corrALT == 3
                   Assumptions :→ Hp ≥ 0]
                  ⎪ Simplify[NUdnTH /. {RaTH → Rap},                   corrALT == 4
                   Assumptions :→ Hp ≥ 0]
                  ⎪ Simplify[NUdnAC /. {RaAC → Rap, H → Hp, R → rLP},  ValueQ[corrA
                   Assumptions :→ Hp ≥ 0]
                  ⎩

   NUpsd = Simplify[NUsdCO /. {RaCO → Rap}, Assumptions :→ Hp ≥ 0];
  ];
  NUpspec =
```

```
    Simplify[NUdnCO /. {RacCO → Ra /. {β → βp, Q → Qp, H → Hcrit, ρ → ρp,
          α → αp, μ → μp, k → kp}, Hc → Hcrit}, Assumptions :→ Hp ≥ 0];

  hpup = Simplify[h /. {NU → NUpup, k → kp, H → Hp}, Assumptions :→ Hp ≥ 0];
  hpsd = Simplify[h /. {NU → NUpsd, k → kp, H → Hp}, Assumptions :→ Hp ≥ 0];
  hpspec =
   Simplify[h /. {NU → NUpspec, k → kp, H → Hcrit}, Assumptions :→ Hp ≥ 0];

  NUmup = FullSimplify[
    NUupGD /. {RaGD → Ramup, PrGD → Prm}, Assumptions :→ Hm > 0];
  NUmsd = FullSimplify[NUsdCh /. {RaCh → Ramsd, PrCh → Prm},
    Assumptions :→ Hm > 0];

  hmup = FullSimplify[
    h /. {NU → NUmup, k → km, H → Hm}, Assumptions :→ Tmdn > Tmup];
  hmsd = FullSimplify[h /. {NU → NUmsd, k → km, H → y},
    Assumptions :→ Tmdn > Tmup && y ∈ Reals];
(*-------------------------------------------------*)
  (*CHF Correlation*)

  qchf0[θ_] := Achf + Bchf * (θ * 180/π) + Cchf * (θ * 180/π)^2 +
                 Dchf * (θ * 180/π)^3 + Echf * (θ * 180/π)^4
               Achf + Bchf * (π/2 * 180/π) + Cchf * (π/2 * 180/π)^2 +
                 Dchf * (π/2 * 180/π)^3 + Echf * (π/2 * 180/π)^4

  qchf[θ_] := 1.3 * qchf0[θ];
For[i = 0, i ≤ nθ, i++,
   qchfpθ[i] = qchf[θi[i]]];
  genout[7] :=
   Grid[{{"Q̇decay", "Q̇pool", "Q̇LM", "q''CHF,max"}, {Qd, Qp, Qm, qchf[π/2]}},
    Alignment → {Left, Bottom}, Frame → {All, False}];
  (*-------------------------------------------------*)
(*Solution Equations*)
  (*Oxide Pool Solutions*)
  Clear[peqs, qpsdi, qcsdi, δcsdi, Tcsdi, Tvoi, δvoi];
  peqs[1] = Simplify[peq[1] /. {qpup → (qpup), Tpmx → (Tpmx), hpup → hpup},
    Assumptions :→ Hp ≥ 0];
  peqs[2] = Simplify[peq[2] /. {qcup → (qcup), Tcup → (Tcup),
      δcup → (δcup)}, Assumptions :→ δcup > 0];
```

```
peqs[3] = Simplify[peq[3] /. {qcup → (qcup),
     qpup → (qpup), δcup → (δcup)}];
peqs[4] = { Simplify[peq[4] /. {qrad → (qcup), Tcup → (Tcup)},
            Assumptions :→ Tcup ≥ 0]
          { 0

For[i = 0, i ≤ nθ, i++,
 peqs[5 + 7 i] = Simplify[peq[5] /. {qpsdθ → (qpsdi[i]), hpsdθ →
       gθ[θgθ, θi[i]] * { hpspec /. Rc → rcurv[θi[i]]   θi[i] ≤ π/2 && fLP > 1
                       { hpsd / gθ[θgθ, θi[i]]          θi[i] > π/2 && fLP > 1,
                       { hpsd                           fLP == 1
      Tpmx → (Tpmx)}, Assumptions :→ Hp ≥ 0];
 peqs[6 + 7 i] = Simplify[peq[6] /. {qcsdθ → (qcsdi[i]), Tcsdθ →
       (Tcsdi[i]), δcsdθ → (δcsdi[i])}, Assumptions :→ δcsdi[i] > 0];
 peqs[7 + 7 i] = Simplify[peq[7] /. {qcsdθ → (qcsdi[i]),
      qpsdθ → (qpsdi[i]), δcsdθ → (δcsdi[i])}];
 peqs[8 + 7 i] = Simplify[peq[8] /. {qcsdθ → (qcsdi[i]),
      Tcsdθ → (Tcsdi[i]), Tvoθ → (Tvoi[i]), δvθ → (δvoi[i])}];
 peqs[9 + 7 i] = Simplify[peq[9] /. {qcsdθ → (qcsdi[i]), Tvoθ → (Tvoi[i])},
   Assumptions :→ Tvoi[i] > 0];
 peqs[10 + 7 i] = δvoi[i] == 1.0 (δvo);
 peqs[11 + 7 i] = Tcsdi[i] == 1.0 (Tves);
];
peqs[12 + 7 nθ] = Simplify[peq[10] /. {qcup → (qcup),
     ΣqAθ → (Sum_{i=1}^{nθ} (Mean[{qcsdi[i - 1], qcsdi[i]}] * Acsdθ[i]))}];
peqs[13 + 7 nθ] = Simplify[peq[11] /. {δcup → (δcup),
     δcsd0 → (δcsdi[0])}];
(*LM Layer Substitutions*)
Clear[meqs, qmsdi, Tvomi, Tmsdi, δvmi]
 For[i = 1, i ≤ nH, i++,
  meqs[1 + 5 (i - 1)] =
   Simplify[meq[1] /. {qmsdH → qmsdi[i], hmsdH → (Mean[Table[hmsd /.
            {y → (Hm - Hhmi[nHh/nH (i) - j] + 0.001), TmsdH → Tmsdi[nH]},
            {j, 1, nHh/nH - 1}]]), Tmdn → Tcup, TmsdH → Tmsdi[i]}];
  meqs[2 + 5 (i - 1)] = Simplify[meq[2] /. {qmsdH → qmsdi[i],
      TvomH → Tvomi[i], TmsdH → Tmsdi[i], δvmH → δvmi[i]}];
  meqs[3 + 5 (i - 1)] = Simplify[meq[3] /.
```

```
        {qmsdH → qmsdi[i], TvomH → Tvomi[i]}];
      meqs[4 + 5 (i - 1)] = δvmi[i] == 1.0 (δvo);
      meqs[5 + 5 (i - 1)] = Tmsdi[i] == 1.0 (Tves);];
   meqs[6 + 5 (nH - 1)] = Simplify[meq[4] /. {Tmdn → Tcup}];
   meqs[7 + 5 (nH - 1)] = Simplify[meq[5] /. {qrad → (qmup)}];
   meqs[8 + 5 (nH - 1)] =
    Simplify[meq[6] /. {qsrc → qcup, ΣqAH → Σ_{i=1}^{nH} (qmsdi[i] * AmsdH[i])}];

(*-------------------------------------------------*)
   (*-------------------------------------------------*)
   (*-------------------------------------------------*)
   (*Solution Loop*)
   Do[
    Clear[peqsetall, peqset, peqsetinit, pvarset,
     pscaleset, pguessset, pvarsetθ, pscalesetθ, pguesssetθ,
     papproxset, ptopgrid, psidegrid, meqset, mvarset,
     mvarsetH, mscaleset, mscalesetH, mguessset, mguesssetH,
     mapproxset, msolset, mtopgrid, msidegrid, nmelt, nmmelt];
    FitFunc[x_] = -0.086437370675640 x^4 + 0.060424130274896 x^3 +
      0.106173867809616 x^2 - 0.007379075912866 x + 0.028884325800016;
    peqsetall = Table[peqs[m], {m, 1, 13 + 7 nθ}];
    κup := { 0.5  LMM < 1
           { 0.   LMM ≥ 1 ;
    For[i = 0, i ≤ nθ, i++,
     pvarsetθ[i] =
      {qpsdi[i], qcsdi[i], Tcsdi[i], Tvoi[i], δcsdi[i], δvoi[i]};
     pscalesetθ[i] = {10^0, 10^0, 10^3, 10^2, 10^-2, 10^-1};
     pguesssetθ[i] = {
       {Round[(0.35 Qd FitFunc[i/nθ]) - 0.05 Qc, 25000],
        Max[Floor[(0.4 + 0.3 i/nθ) .35 (Qd FitFunc[i/nθ]) - 0.05 Qc, 25000]
          10.^-6, 1.0], Ceiling[1.5 qchf[π/2] - 0.05 Qc, 25000]},
       {Round[(0.35 Qd FitFunc[i/nθ]), 25000],
        Floor[(0.4 + 0.3 i/nθ) .35 (Qd FitFunc[i/nθ]), 25000] 10.^-6,
        Ceiling[1.5 qchf[π/2], 25000]},
       1.58, 4.1, {5., 10.^-4, 10.}, {1.5, 10.^-4, 1.5}};
    ];
    pvarset = Flatten[Append[{Hp, qpup, qcup, Tpmx, Tcup, δcup},
```

```
    Table[pvarsetθ[i], {i, 0, nθ}]]];
pscaleset = Flatten[Append[{10^0, 10^0, 10^0, 10^3, 10^3, 10^-3},
    Table[pscalesetθ[i], {i, 0, nθ}]]];
pguessset = Flatten[Append[
     {0.96 Hcor, {{{Round[Qd/(3 Acup), 100 000], Floor[Qd/(8 Acup), 100 000],
          Ceiling[1.5 qchf[π/2], 100 000]}}}, {{{Round[Qd/(3 Acup), 100 000],
          Floor[Qd/(8 Acup), 100 000], Ceiling[1.5 qchf[π/2], 100 000]}}},
      3.2, (2. + κup), {{{5., 10.^-2, 10.}}}},
     Table[pguessetθ[i], {i, 0, nθ}]], 2] * pscaleset;
papproxset = Table[Flatten[
    Prepend[{pguessset[[i]]}, pvarset[[i]]]], {i, 1, 6 (nθ + 2)}];
meqsetall = Table[meqs[i], {i, 1, 8 + 5 (nH - 1)}];
midpool = pguessetθ[Floor[nθ/2]][[2]][[1]];
maxpool = pguessetθ[nθ][[2]][[1]];
For[i = 1, i ≤ nH, i++,
 mvarsetH[i] = {qmsdi[i], Tvomi[i], Tmsdi[i], δvmi[i]};
 mscalesetH[i] = {10^0, 10^2, 10^3, 10^-1};
 mguessetH[i] = {Floor[midpool + i/nH (maxpool - midpool), 100 000],
    4.1, 1.58, {1.5, 10.^-6, 1.5}};];
mvarset = Flatten[Append[{qmup, Tmup},
    Table[mvarsetH[i], {i, 1, nH}]]];
mscaleset = Flatten[Append[{10^0, 10^3},
    Table[mscalesetH[i], {i, 1, nH}]]];
mguessset = Flatten[Append[{{{{Floor[2 Qd/(8 Acup), 100 000],
          10.^-6, Ceiling[3 Qd/(4 Acup), 100 000]}}}, (2. + κup)},
     Table[mguessetH[i], {i, 1, nH}]], 2] * mscaleset;
mapproxset = Table[Flatten[Prepend[{mguessset[[i]]}, mvarset[[i]]]],
  {i, 1, 2 + 4 nH}];


peqsetinit = Delete[peqsetall, Flatten[Append[
     {If[Hm > 0.01, {{4}}, {}]}, Table[{11 + 7 i}, {i, 0, nθ}]], 1]];
meqsetinit = Delete[meqsetall, Flatten[
    Append[{}, Table[{5 + 5 (i - 1)}, {i, 1, nH}]], 1]];
eqsetinit = Join[peqsetinit, meqsetinit];
```

```
varset = Join[pvarset, mvarset];
approxset = Join[papproxset, mapproxset];

solsetinit = (varset /.
    FindRoot[eqsetinit, approxset, MaxIterations → Infinity]);
meltiter = 0;
For[i = 0, i ≤ nθ, i++,
 nmelt[meltiter] = nθ + 1;
 If[solsetinit[[6 i + 9]] ≥ Tves, nmelt[meltiter] = i;
  Break[];];];
For[i = 1, i ≤ nH, i++,
 nmmelt[meltiter] = nH + 1;
 If[solsetinit[[17 + 6 nθ + 4 (i - 1)]] ≥ Tves, nmmelt[meltiter] = i;
  Break[];];];

Label[melting];
peqset = Delete[peqsetall, Flatten[Append[{If[Hm > 0.01, {{4}}, {}]},
     Join[Table[{11 + 7 i}, {i, 0, nmelt[meltiter] - 1}],
      Table[{10 + 7 i}, {i, nmelt[meltiter], nθ}]]], 1]];
meqset = Delete[meqsetall, Flatten[Append[{{}},
     Join[Table[{5 + 5 (i - 1)}, {i, 1, nmmelt[meltiter] - 1}],
      Table[{4 + 5 (i - 1)}, {i, nmmelt[meltiter], nH}]]], 1]];
eqset = Join[peqset, meqset];
solset =
 (varset /. FindRoot[eqset, approxset, MaxIterations → Infinity]);

meltiter++;
For[i = 0, i ≤ nθ, i++,
 nmelt[meltiter] = nθ + 1;
 If[solset[[6 i + 9]] ≥ Tves, nmelt[meltiter] = i;
  Break[];];];
For[i = 1, i ≤ nH, i++,
 nmmelt[meltiter] = nH + 1;
 If[solset[[17 + 6 nθ + 4 (i - 1)]] ≥ Tves, nmmelt[meltiter] = i;
  Break[];];];
If[
 nmelt[meltiter - 1] ≤ nmelt[meltiter] &&
  nmmelt[meltiter - 1] ≤ nmmelt[meltiter],
 meltnum = meltiter;,
 Clear[solset, peqset, meqset, eqset];
```

```
 Goto[melting];]

genout[8] := Grid[{{"C_boil", "Pr_OX", "Ra_OX", "Pr_LM", "Ra_LM,up", "Ra_LM,sd"},
    {Cboil, Prp, Rap /. Hp → solset[[1]], Prm,
     Ramup /. {Tmup → solset[[14 + 6 nθ]], Tmdn → solset[[5]]},
     Ramsd /. {TmsdH → solset[[17 + 6 nθ + 4 (nH - 1)]],
       Tmup → solset[[14 + 6 nθ]], y → (Hm - Hhmi[nHh - 2] + 0.001)}}},
  Alignment → {Left, Bottom}, Frame → {All, False}];
corrList = {"INEEL", "ACOPO", "KE/MA", "minACOPO", "Appen V"};
genout[9] :=
 Grid[{{"Corr", "Ra_OX", "NU_up", "NU_dn"}, {ToString[corrALT] <>
     "-" <> corrList[[corrALT + 1]], Rap, NUpup, NUpsd}},
  Alignment → {Left, Bottom}, Frame → {All, False}, ItemSize → 9];

(*-------------------------------------------------*)
(*Results Prep*)
ptopgrid = Grid[
  MapThread[Prepend, {{{"H_pool", "q''_p,up", "q''_c,up", "T_p^max", "T_c,up", "δ_c,up"},
     Table[Flatten[{pguessset[[i]]}][[1]], {i, 1, 6}],
     solset[[1 ;; 6]]}, {"Var", "Guess", "Actual"}}],
  Frame → {1 → True, All}, Alignment → {Center, Bottom}];
For[i = 0, i ≤ nθ, i++,
 psidegrid[i] =
   Grid[MapThread[Prepend,
     {MapThread[Prepend, {{{"q''_p,sd", "q''_c,sd", "T_c,sd", "T_v^out", "δ_c,sd",
          "δ_v"}, Table[Flatten[{pguessset[[j + 6 i]]}][[1]],
          {j, 7, 12}], solset[[(7 + 6 i) ;; (12 + 6 i)]]},
        {"Var", "Guess", "Actual"}}], {"θ_i", i, Round[θi[i] * 180/π]}}}],
    Frame → {1 → True, All}, Alignment → {Center, Bottom}];];
mtopgrid = Grid[MapThread[Prepend, {{{"H_LM", "q''_m,up", "T_m,up"},
     Prepend[Table[Flatten[{mguessset[[i]]}][[1]], {i, 1, 2}], "--"],
     Prepend[{solset[[13 + 6 nθ]], solset[[14 + 6 nθ]]}, Hm]},
    {"Var", "Guess", "Actual"}}],
  Frame → {1 → True, All}, Alignment → {Center, Bottom}];
For[i = 1, i ≤ nH, i++,
 msidegrid[i] =
   Grid[MapThread[Prepend,
     {MapThread[Prepend, {{{"q''_m,sd", "T_v,m^out", "T_m,sd", "δ_v,m", "h_m,sd^HTC"},
         Flatten[{Table[Flatten[{mguessset[[j + 4 (i - 1)]]}]][[1]],
```

```
                    {j, 3, 6}], "--"}], Flatten[
                  {solset[[(15 + 6 nθ + 4 (i - 1)) ;; (18 + 6 nθ + 4 (i - 1))]],
                   (Mean[Table[hmsd /. {y → (Hm - Hhmi[nHh/nH i - j] + 0.001),
                         TmsdH → solset[[17 + 6 nθ + 4 (nH - 1)]],
                         Tmup → solset[[14 + 6 nθ]]}, {j, 1, nHh/nH - 1}]])}]],
              {"Var", "Guess", "Actual"}}], {"Hi", i, NumberForm[
              Round[Mean[Table[Hhmi[j], {j, nHh/nH (i - 1) + 1, nHh/nH i}]], .001],
              {4, 3}]}}], Frame → {1 → True, All},
          Alignment → {Center, Bottom}];];, {1}];
Grid[approxset];
   (*-------------------------------------------------*)
(*Plot Prep*)
   (*Oxide Pool*)
   ticksetP = Table[θi[i] * 180/π, {i, 0, nθ}];
   qpθplot = ListPlot[{Table[{θi[i] * 180/π, solset[[6 i + 7]]}, {i, 0, nθ}],
      Table[{θi[i] * 180/π, solset[[6 i + 8]]}, {i, 0, nθ}](*,
      Table[{θi[i]*180/π,qchfpθ[i]},{i,0,nθ}]*)}, Joined → {True},
     Ticks → {Round[ticksetP], Automatic}, AxesLabel →
      {"θi [°]", "q''sd [W*m^-2]"}, PlotRange → {{0, θmax * 180/π}, All},
     PlotStyle → {ColorData[97, 2], ColorData[97, 1], ColorData[97, 4]},
     PlotLegends → {"q''p,sd", "q''c,sd", "q''CHF"},
     PlotMarkers → If[fLP == 1, Automatic, "X"]];
   qchfplot = Show[ListPlot[Table[{θi[i] * 180/π, solset[[6 i + 8]]/qchfpθ[i]},
       {i, 0, nθ}], Joined → {True}, Ticks → {Round[ticksetP], Automatic},
      AxesLabel → {"θi [°]", "q''c,sd/q''CHF"}, PlotStyle → ColorData[97, 1],
      PlotRange → {All, {0, 1.2}},
      PlotMarkers → If[fLP == 1, Automatic, "X"]], Plot[1.0,
      {x, 0, θmax * 180/π}, PlotStyle → {Dashed, ColorData[97, 4]}]];
   TpθPlot = ListPlot[{Table[{θi[i] * 180/π, solset[[6 i + 9]]}, {i, 0, nθ}],
      Table[{θi[i] * 180/π, solset[[6 i + 10]]}, {i, 0, nθ}],
```

```
      Table[{θi[i] * 180/π, Tves}, {i, 0, nθ}]}, Joined → {True},
     Ticks → {Round[ticksetP], Automatic}, AxesLabel → {"θi [°]", "T [K]"},
     PlotStyle → {ColorData[97, 2], ColorData[97, 1], Black},
     PlotLegends → {"Tv^in", "Tv^out", "Tves^melt"}, PlotRange → {All, {200, 1800}},
     PlotMarkers → If[fLP == 1, Automatic, {"X", Automatic, Automatic}]];
  δpθplot = ListPlot[{Table[{θi[i] * 180/π, solset[[6 i + 11]]}, {i, 0, nθ}],
      Table[{θi[i] * 180/π, Max[solset[[6 i + 12]], 0]}, {i, 0, nθ}]},
     Joined → {True}, Ticks → {Round[ticksetP], Automatic},
     AxesLabel → {"θi [°]", "δ [m]"},
     PlotStyle → {ColorData[97, 2], ColorData[97, 1]},
     PlotLegends → {"δc,sd", "δv"}, PlotRange → {All, {-0.01, 0.20}},
     AxesOrigin → {0, -0.01}, PlotMarkers → If[fLP == 1, Automatic, "X"]];
  (*LM Layer*)
qmHplot = ListPlot[
     Table[{solset[[(15 + 6 nθ + 4 (i - 1))]], Round[Hhmi[nHh/nH i - 2], .001]},
      {i, 1, nH}], Joined → {True}, Mesh → Full,
     InterpolationOrder → 1, PlotRange → {{0, All}, {-ΔH, Hm + ΔH}},
     AxesOrigin → {0, -ΔH}, AxesLabel → {"q'm,sd", "HLM"},
     PlotMarkers → If[fLP == 1, Automatic, "X"]];
δmHplot = ListPlot[Table[{Max[solset[[(18 + 6 nθ + 4 (i - 1))]], 0],
       Round[Hhmi[nHh/nH i - 2], .001]}, {i, 1, nH}],
     Joined → {True}, Mesh → Full, InterpolationOrder → 1,
     PlotRange → {{-0.05, 0.2}, {-ΔH, Hm + ΔH}},
     AxesOrigin → {-0.05, -ΔH}, AxesLabel → {"δm,sd", "HLM"},
     PlotMarkers → If[fLP == 1, Automatic, "X"]];
  (*Joint Plots*)
rangemax =
    Max[1.2, 1.1 * Table[solset[[(15 + 6 nθ + 4 (i - 1))]]/10^6, {i, 1, nH}]];
  qjointplot = ListPlot[{Table[{θi[i]/θi[nθ], solset[[6 i + 8]]/10^6}, {i, 0, nθ}],
      Table[{1 + (θm[i] - θm[0])/(θm[nH] - θm[0]), solset[[(15 + 6 nθ + 4 (i - 1))]]/10^6},
       {i, 1, nH}]}, Frame → True, PlotRange → {{0, 2.1}, {0, rangemax}},
     FrameTicks → {{{0, 0}, {0.5, "θOX/2"}, {1.0, "θOX"}, {1.5, "HLM/2"},
        {2.0, "HLM"}}, Automatic}, FrameTicksStyle → 14,
```

```
  FrameLabel → {Style["Location", 18], Style["q''sd (MW/m^2)", 18]},
  GridLines → {{0.5, 1.0, 1.5, 2.0}, Automatic},
  GridLinesStyle → Directive[Dashed, Opacity[0.25]],
  PlotMarkers → If[fLP == 1, Automatic, "X"], ImageSize → 72 * 6];
δjointplot = ListPlot[{Table[{θi[i]/θi[nθ], solset[[6 i + 12]]}, {i, 0, nθ}],
   Table[{1 + (θm[i] - θm[0])/(θm[nH] - θm[0]), Max[solset[[(18 + 6 nθ + 4 (i - 1))]], 0]},
    {i, 1, nH}]}, Frame → True, PlotRange → {{0, 2.1}, {-0.01, 0.2}},
  FrameTicks → {{{0, 0}, {0.5, "θOX/2"}, {1.0, "θOX"}, {1.5, "HLM/2"},
     {2.0, "HLM"}}, Automatic}, FrameTicksStyle → 14,
  FrameLabel → {Style["Location", 18], Style["δves (m)", 18]},
  GridLines → {{0.5, 1.0, 1.5, 2.0}, Automatic},
  GridLinesStyle → Directive[Dashed, Opacity[0.25]],
  PlotMarkers → If[fLP == 1, Automatic, "X"], ImageSize → 72 * 6];
chfjointplot = Show[ListPlot[
   {Table[{θi[i]/θi[nθ], solset[[6 i + 8]]/qchf[θi[i]]}, {i, 0, nθ}], Table[
     {1 + (θm[i] - θm[0])/(θm[nH] - θm[0]), solset[[(15 + 6 nθ + 4 (i - 1))]]/qchf[θm[i]]}, {i, 1, nH}]},
   Frame → True, PlotRange → {{0, 2.1}, {0.0, 1.6}},
   FrameTicks → {{{0, 0}, {0.5, "θOX/2"}, {1.0, "θOX"}, {1.5, "HLM/2"},
      {2.0, "HLM"}}, Automatic}, FrameTicksStyle → 14,
   FrameLabel → {Style["Location", 18], Style["q''sd/q''CHF", 18]},
   GridLines → {{0.5, 1.0, 1.5, 2.0}, Automatic},
   GridLinesStyle → Directive[Dashed, Opacity[0.25]],
   PlotMarkers → If[fLP == 1, Automatic, "X"]],
  Plot[1.0, {x, 0, 2.0}, PlotStyle → {Dashed, ColorData[97, 4]}],
  ImageSize → 72 * 6];
(*Esmaili Plots*)
esqpθdata = Table[{θi[i] * 180/π, solset[[6 i + 8]]/1000}, {i, 0, nθ}];
esqchfdata = Table[{θi[i] * 180/π, solset[[6 i + 8]]/qchfpθ[i]}, {i, 0, nθ}];
esδcθdata = Table[{θi[i] * 180/π, 100 * solset[[6 i + 11]]}, {i, 0, nθ}];
esδvθdata =
 Table[{θi[i] * 180/π, Max[100 * solset[[6 i + 12]], 0]}, {i, 0, nθ}];
Clear[ρguess, ρtotal];
ρguess[1] =
```

```
    Abs[pguessset[[7 + 6 * Floor[nθ/2]]][[1]] - solset[[7 + 6 * Floor[nθ/2]]]];
  ρguess[2] = Abs[pguessset[[8 + 6 * Floor[0.9 * nθ]]][[1]] -
      solset[[8 + 6 * Floor[0.9 * nθ]]]];
  ρguess[3] = Abs[mguessset[[3 + 4 (Floor[nH/2] - 1)]] -
      solset[[(15 + 6 nθ + 4 (Floor[nH/2] - 1))]]];
  ρtotal = Sum[ρguess[i], {i, 1, 3}];
  If[ρtotal < 1000, ρpen++; Print["Whoops"]; Goto[start];];
  , {1}];
```

Results Loop

```
labelloop := Do[
  If[fLP == 1, Goto[Hemi], If[fLP > 1, Goto[Elli], Print["Error: fLP < 1"];
    Break[];]];
  Label[Hemi];
  HSchfOP = qchfplot;
  HSTpθOP = Tpθplot;
  HSqJNT = qjointplot;
  HSchfJNT = chfjointplot;
  HSδJNT = δjointplot;
  HSOXθ = Round[θmax * 180/π, 0.01];
  HSLMθ = Round[θmmax * 180/π, 0.01];
  Goto[Stop];
  Label[Elli];
  ELchfOP = qchfplot;
  ELTpθOP = Tpθplot;
  ELqJNT = qjointplot;
  ELchfJNT = chfjointplot;
  ELδJNT = δjointplot;
  ELOXθ = Round[θmax * 180/π, 0.01];
  ELLMθ = Round[θmmax * 180/π, 0.01];
  Goto[Stop];
  Label[Stop];, {1}];
jointloop := Do[
  SetDirectory[$UserDocumentsDirectory];
```

```
    SetDirectory["Cases\\Joint"];
    Print[
     Grid[{{"Qdecay", "OX Mass", "LM Mass", "Ellipse", "HS θ", "EL θ"},
       {Qd, mcor, mLM, fLP, HSOXθ, ELOXθ}, {Qd / Pdecay[Qt, td],
        mcor / 88 783.187, mLM / 79 595.958, fLP, HSLMθ, ELLMθ}},
      Alignment → Left, Frame → All]];
    (*Print[Text@Style[
       "-----------------------------------------------------------------
         --",Bold,Larger]];
    Print[Text@Style["Oxide Pool Results",Bold,Larger]];
    Show[HSchfOP,ELchfOP,ImageSize→Large]//Print;
    Show[HSTpθOP,ELTpθOP,ImageSize→Large]//Print;*)
    Print[Text@Style[
       "-----------------------------------------------------------------
         --", Bold, Larger]];
    Print[Text@Style["Joint Layer Results", Bold, Larger]];
    Show[HSqJNT, ELqJNT, ImageSize → Large] // Print;
    Show[HSchfJNT, ELchfJNT, ImageSize → Large] // Print;
    Show[HSδJNT, ELδJNT, ImageSize → Large] // Print;
    Export[ToString[case] <> "-jqflux" <> ".png",
     Show[HSqJNT, ELqJNT, ImageSize → Large]];
    Export[ToString[case] <> "-jchf" <> ".png",
     Show[HSchfJNT, ELchfJNT, ImageSize → Large]];
    Export[ToString[case] <> "-jdel" <> ".png",
     Show[HSδJNT, ELδJNT, ImageSize → Large]];
    , {1}];
resloop := Do[
    SetDirectory[$UserDocumentsDirectory];
    SetDirectory["Cases\\HS-EL"];
    Print[
     Grid[{{"Correlation", "Qdecay", "OX Mass", "LM Mass", "Ellipse"},
       {ToString[corrALT] <> "-" <> corrList[[corrALT + 1]], Qd,
        mcor, mLM, fLP}, {"--", Qd / Pdecay[Qt, td], mcor / 88 783.187,
        mLM / 79 595.958, fLP}}, Alignment → Left, Frame → All]];
    Print[Text@Style[
       "-----------------------------------------------------------------
         --", Bold, Larger]];
    Print[Text@Style["General Results", Bold, Larger]];
    For[i = 1, i ≤ 8, i++,
     Print[genout[i]];];
```

```
Print[genout[9]];
(*Show[ListPlot[Table[{i/nθ, solset[[6(i)+8]]}, {i,0,nθ}]],
  Plot[(1.6-0.5x).4(Qd FitFunc[x]), {x,0,1}],
  Plot[(0.4+0.3x).35(Qd FitFunc[x]), {x,0,1}], PlotRange→All];*)
(*Print[Text@Style[
   "-----------------------------------------------------------------
     --",Bold,Larger]];
Print[Text@Style["Oxide Pool Results",Bold,Larger]];
*)For[i = 0, i ≤ nθ, i++,
 If[i == 0, Print[ptopgrid]];
 Print[psidegrid[i]];]; (*
Show[δpθplot,ImageSize→Large]//Print;
Show[qpθplot,ImageSize→Large]//Print;
Show[qchfplot,ImageSize→Large]//Print;*)
(*Show[Tpθplot,ImageSize→Medium]//Print;*)
(*Print[Text@Style[
   "-----------------------------------------------------------------
     --",Bold,Larger]];
Print[Text@Style["LM Layer Results",Bold,Larger]];
*)For[i = 1, i ≤ nH, i++,
 If[i == 1, Print[mtopgrid]];
 Print[msidegrid[i]];];
Show[qmHplot, ImageSize → Large] // Print;
Show[δmHplot, ImageSize → Large] // Print;
Print[Text@Style[
   "-----------------------------------------------------------------
     --", Bold, Larger]];
Print[Text@Style["Two Layer Results", Bold, Larger]];
Show[qjointplot, ImageSize → Large] // Print;
Show[chfjointplot, ImageSize → Large] // Print;
Show[δjointplot, ImageSize → Large] // Print;
If[fLP == 1, geo = "HS", geo = "EL"];
Export[ToString[case] <> geo <> "-qflux" <> ".png",
 Show[qjointplot, ImageSize → Large]];
Export[ToString[case] <> geo <> "-chf" <> ".png",
 Show[chfjointplot, ImageSize → Large]];
Export[ToString[case] <> geo <> "-del" <> ".png",
 Show[δjointplot, ImageSize → Large]];
(*Print[Text@Style[
   "-----------------------------------------------------------------
```

```
      --",Bold,Larger]];
Print[Text@Style["Esmaili Layer Results",Bold,Larger]];
Show[esδcθplot,ImageSize→Large]//Print;
Show[esqpθplot,ImageSize→Large]//Print;
Show[esqchfplot,ImageSize→Large]//Print;
Show[esδvθplot,ImageSize→Large]//Print;*)
, {1}];
```